Title
Quantum Measurement with Atomic Cavity Optomechanics

Author
Schreppler, Sydney Frances

Publication Date
2016

Peer reviewed|Thesis/dissertation

Quantum Measurement with Atomic Cavity Optomechanics

By

Sydney Frances Schreppler

A dissertation submitted in partial satisfaction of the

requirements for the degree of

Doctor of Philosophy

in

Physics

in the

Graduate Division

of the

University of California, Berkeley

Committee in charge:

Professor Dan M. Stamper-Kurn, Chair
Professor Irfan Siddiqi
Professor Jeffrey A. Reimer

Spring 2016

Quantum Measurement with Atomic Cavity Optomechanics

Abstract

Quantum Measurement with Atomic Cavity Optomechanics

by

Sydney Frances Schreppler

Doctor of Philosophy in Physics

University of California, Berkeley

Professor Dan M. Stamper-Kurn, Chair

A cloud of ultracold atoms trapped within the confines of a high-finesse optical cavity shakes from the pressure of the light that probes it. This form of measurement backaction, a central component of quantum measurement theory, is the subject of this dissertation. Enlisting the collective motion of ultracold atoms as the mechanical degree of freedom in a cavity optomechanical system, we reach settings cold and quiet enough to allow for the effects of measurement backaction to manifest. We report predictions for and experimental observations of the Standard Quantum Limit for force sensitivity, optical ponderomotive squeezing, and the possibility of complex squeezing through generalized optical correlations.

Contents

List of Figures **iii**

List of Tables **v**

Acknowledgments **vi**

1 Introduction **1**
1.1 Quantum measurement . . . 1
1.2 Cavity quantum electrodynamics . . . 4
1.3 Cavity optomechanics . . . 6
1.4 Combining the elements . . . 9

2 Tools **11**
2.1 Introduction . . . 11
2.2 Atom chip and optical cavity . . . 12
2.3 Fiber switch . . . 16
2.4 Mechanical superlattice . . . 19
2.5 Heterodyne detection . . . 21

3 Force Sensitivity Measurement **27**
3.1 Introduction . . . 27
3.2 The Standard Quantum Limit . . . 28
3.3 DC force measurement . . . 33
3.4 Calibrating applied force . . . 36
3.5 Fitting the data . . . 37
3.5.1 Separating signal from noise . . . 37
3.5.2 Anharmonic trap . . . 40
3.5.3 Discrepancies in C_{om} . . . 43
3.6 Plotting in phase space . . . 45

4 Ponderomotive Squeezing **48**
4.1 Introduction . . . 48
4.2 Predicted spectra . . . 50

4.3 Experimental observation 54
4.4 Squeezing force sensitivity 60

5 Complex Squeezing **64**
5.1 Introduction 64
5.2 Eigenmodes of complex squeezing 65
5.2.1 Generalized covariance matrices 67
5.2.2 Homodyne quantum operators 69
5.2.3 Limits on squeezing 71
5.3 Experimental observations 75
5.3.1 New search for complex squeezing 76
5.3.2 Angles of complex squeezing 79
5.3.3 Requirements for detection 81

Bibliography **83**

Appendix A Digital heterodyne demodulation **89**

List of Figures

1.1 Sensitive quantum measurement . . . 3
1.2 Jaynes-Cummings interaction . . . 5
1.3 Optomechanical interaction . . . 8

2.1 Atom chip and cavity . . . 13
2.2 Tunable optomechanics . . . 15
2.3 Fiber switch wavemeter lock . . . 18
2.4 Superlattice potential . . . 19
2.5 Mechanical spectral control . . . 20
2.6 Lattice force . . . 21
2.7 Phase insensitive heterodyne lock . . . 23
2.8 Heterodyne locking and PM detection . . . 25

3.1 Components of the SQL . . . 29
3.2 Force vs. position sensitivity . . . 33
3.3 Loading site mechanical spectrum . . . 34
3.4 Cavity shift potential steps . . . 35
3.5 Model determined force . . . 36
3.6 Phase space . . . 38
3.7 Complex force response fit . . . 39
3.8 Coherent and incoherent force responses . . . 40
3.9 Anharmonic PSD and level spacing . . . 41
3.10 Differences in C_{om} . . . 44
3.11 Phase space plots . . . 46

4.1 Quadrature squeezing of light . . . 49
4.2 Optomechanical feedback . . . 50
4.3 Ponderomotive squeezing trends . . . 54
4.4 $\chi(\omega)$ . . . 55
4.5 Ponderomotive squeezing with probe detuning . . . 55
4.6 Quantifying LO power variations . . . 58
4.7 Resonant probe squeezing quadrature map and slices . . . 59
4.8 Multioscillator technical squeezing . . . 60

4.9 Mechanical susceptibility and force sensitivity quadrature maps 61
4.10 Optimal sensitivity parameters 62

5.1 Complex $\chi(\omega)$ 65
5.2 Eigenvectors of covariance matrices 66
5.3 Homodyne beamsplitter 69
5.4 Eigenmodes of measured ponderomotive squeezing 75
5.5 Relative quadrature response phases 76
5.6 Eigenvalue spectrum of resonant optomechanical response 77
5.7 Dependence of complex squeezing on detection efficiency 78
5.8 Dependence of complex squeezing on thermal occupation 78
5.9 Eigenvector angles for experimental optomechanical response 80
5.10 Synodyne schematic 81

A.1 Digital heterodyne demodulation 90

List of Tables

2.1 Detection efficiency components 25

3.1 Coupling and cooperativity inconsistencies 45

Acknowledgments

To Dan S-K who was persuasive,
to Nathan who was patient,
to Dan B who was playful,
to Thierry who was loyal,
to Jennie who was meticulous,
to Ed who was observant,
to Ryan who was jocular,
to Nicolas who was steady,
to Jonathan who was amused,
to Lukas who was eloquent,
to Maryrose who was gleeful,
to Claire who was audacious,
to Tom who was mischievous,
to Fang who was sincere,
to Zephy who was cheeky,
to Justin who was eager,
to Shun who was warm,
to Pev who was inspiring,
to Jon who was inviting,
to Jack H who was encouraging,
to Anne T who was compassionate,
to Eleanor who was unflappable,
to Kayte who was bemused,
to Todd who was droll,
to Pat who was tickled,
to Grant who was erudite,
to Jeanne who was open,
to Glenn who was merry,
to Kathleen who was sunny,
to Bob who was trusty,
to Caroline who was strong,
to Gabe who was wry,
to Halleh who was blithe,
to Mom who was constant,
to Dad who was cheering,
to Hayley who was knowing,
to Johnny who was diverting,

I owe you my happiness, my success, and my sanity.

Beginning my studies, the first step pleas'd me so much,
The mere fact, consciousness–these forms–the power of motion,
The least insect or animal–the senses–eyesight;
The first step, I say, aw'd me and pleas'd me so much,
I have never gone, and never wish'd to go, on farther,
But stop and loiter all my life, to sing it in extatic songs.

Walt Whitman, "Beginning my studies", 1900

Chapter 1

Introduction

The glass must stretch
Down his middle,
Or rather down the edge.
But he's in doubt
As to which side's in or out
Of the mirror.
There's little margin for error,
But there's no proof, either.
And if half his head's reflected,
Thought, he thinks, might be affected.

Elizabeth Bishop, "The Gentleman of Shalott", 1936

1.1 Quantum measurement

This dissertation grapples with quantum measurement as a means, and an obstacle, to probing the interactions between light and motion. The theory of quantum mechanics introduces fundamental limits to the characterization of an object where the classical world has none. The existence of these limits has long been an underlying tenet of the theory, though experimental validation has only been recent. As we explore the boundaries, new methods to surpass them by harnessing quantum mechanical interactions proliferate, ensuring that the field of quantum measurement is as dynamic and relevant as ever.

Almost as soon as the process of codifying a quantum theory began, concern about the measurement problem arose. How could the classical and the quantum be teased apart experimentally? Though certain delightfully spooky features of quantum mechanics quickly cemented the theory's appeal in popular culture (Heisenberg's uncertainty principle and Schrödinger's cat being favorites), the development of a theory for quantum measurement did not match that of the general quantum mechanics theory in pace. In particular, the collapse of an object's wave function was considered by the founders of quantum mechanics,

but was not relevant for the probability amplitude measurements of the mid-20th century. Rather, attention waned as many of the experiments testing quantum theory were either destructive by design (the Stern-Gerlach measurement [1], for example), strongly and irreversibly projecting the quantum objects into an eigenstate of the measurement, or they were ensemble measurements of, for example, many nuclei interacting with strong magnetic fields (as in nuclear magnetic resonance [2]).

Nonetheless, in the early days of the quantum mechanics revolution, Dirac [3] and soon after von Neumann [4] realized that in order to test the predictions of quantum mechanics, the results must somehow be linked to us – classical beings who interact with classical detectors. Therein lies the importance of rigorous treatment of the quantum measurement theory. Any tests of quantum mechanics we perform must necessarily include such a quantum-classical leap, and we must account for it when matching laboratory data to theory. How does quantum measurement theory differ from classical measurement theory? Wiseman and Milburn [5] put it well:

> *As we have discussed, with a classical system an ideal measurement can determine with certainty the values of all of the system variables. In this situation of complete knowledge, all subsequent ideal measurement results are determined with certainty. In consequence, measurement and probability do not play a significant role in the foundation of classical mechanics (although they do play a very significant role in practical applications of classical mechanics, where noise is inevitable.)*

Quantum mechanics, by contrast, does not allow for complete knowledge of the values of all system variables. Instead, we are given uncertainty relations among variables, telling us that any additional knowledge of one always comes at the expense of increased uncertainty in another.

Consider, for example, the bosonic creation and annihilation operators, $\hat{a}$ and $\hat{a}^\dagger$, which are applicable both for describing the motion of a mechanical oscillator and the fluctuations of electromagnetic field modes. The commutation relations for modes k and k' are given by, $[\hat{a}_k, \hat{a}_{k'}] = [\hat{a}_k^\dagger, \hat{a}_{k'}^\dagger] = 0$ and $[\hat{a}_k, \hat{a}_{k'}^\dagger] = \delta_{kk'}$[1]. These operators are not Hermitian, and since we deal in the realm of real observables in our laboratory, we are more inclined to consider the canonical quadrature operators $\hat{X}_{\mathrm{AM}} = \left(\hat{a}^\dagger + \hat{a}\right)/\sqrt{2}$ and $\hat{X}_{\mathrm{PM}} = i\left(\hat{a}^\dagger - \hat{a}\right)/\sqrt{2}$. We easily find that the quadrature operators obey the commutation relation $\left[\hat{X}_{\mathrm{AM}}, \hat{X}_{\mathrm{PM}}\right] = i$. This leads to an inequality in the product of their variances: $\Delta X_{\mathrm{AM}}^2 \Delta X_{\mathrm{PM}}^2 \geq 1/4$.

This is the famous Heisenberg uncertainty principle, which I will recall and derive in greater detail later in this dissertation. It can be considered both from the perspective of the intrinsic uncertainty in the object's state and from the perspective of the uncertainty in the measurement record of the object's state. Ultimately, these uncertainties come from the

[1] I regret inconsistencies in my use of the Schrödinger picture ($\hat{a}\,|\psi(t)\rangle$) and the Heisenberg picture ($a(t)\,|\psi\rangle$) of quantum mechanics throughout this dissertation, though I hope that my inclusion of the dependence of certain terms on t or ω will suggest which representation I am employing in a given case.

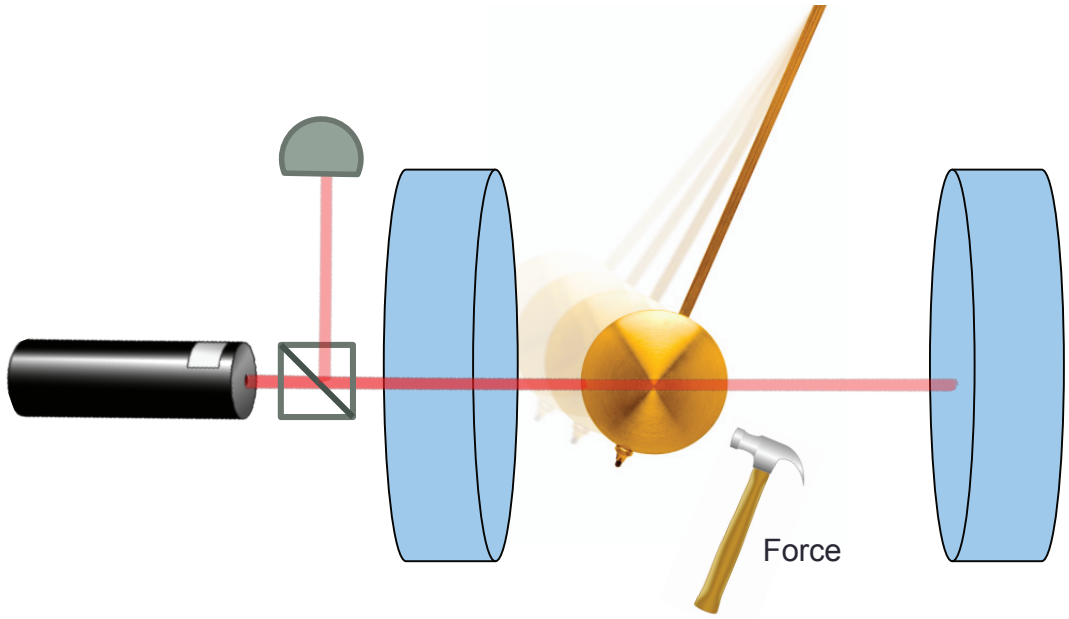

Figure 1.1: Laser light provides a sensitive meter for the displacement of a forced pendulum. To further enhance sensitivity, one can enclose the pendulum within an optical cavity that increases the likelihood that it will interact with the light.

same physical origin, though the latter also relies on the uncertainty in the measurement device itself. On this subtlety, Braginsky et al. [6] offer philosophical discussion:

> *The impossibility of describing the quantum measurement process within the framework of the standard evolutionary apparatus of quantum mechanics can be traced to the fact that the receiver of the measurement's information is a macroscopic observer... One thing, however, is evident: The observer cannot even in principle write down a wave function for himself.*

The solution to the problem of classical observers is that of indirect measurement, using a quantum probe as an intermediary. In this case, the ultimate perturbation of the probed system is due to the internal uncertainty of the quantum probe, which can be well understood. An obvious and extensively studied quantum probe is a well-behaved electromagnetic field mode, the sort that experimentalists can harness thanks to the revolutionary introduction of the laser to laboratories worldwide.

Imagine that we desire to measure the position of a pendulum (shown schematically in Fig. 1.1) after it has been subjected to some unknown force. Because of its precise and minute wavelength, laser light is a desirable meter for such a measurement. We could reflect light off of the pendulum and then mix the reflected light with reference light to produce

an interference pattern detectable on a photodiode. Any change in the position of the pendulum will shift the interference fringes in such a way as to give a sensitive displacement measurement with precision at a fraction of the wavelength of the light. Now suppose that the interaction of the light with the pendulum is slight – that only some of it reflects while the rest passes through the space between the atoms that compose the pendulum, unaffected by their presence. To enhance the likelihood of establishing a detectable signal, we could place a high-reflectivity mirror on either side of the pendulum, such that light injected into the region between the mirrors would bounce back and forth many times, increasing its probability of encountering the pendulum before finally leaking back out of the input mirror, now carrying information about the displacement record. Finally, consider the impact of quantum measurement theory on such a scheme. Not only does the pendulum have some fundamental uncertainty in its position at any given time, but also the light we use to probe it has its own uncertainty. Both contribute to the precision of the measurement. However, this is not the end of our troubles. Because light carries momentum in the form of radiation pressure, any light that interacts with the pendulum pushes on it slightly, altering its trajectory. These disruptive kicks, known in quantum measurement parlance as "backaction", will further affect the result of the measurement.

Despite the absurdity of the scales[2] presented in Fig. 1.1, the schematic nonetheless demonstrates important aspects of the two testbeds of quantum measurement theory I will describe in the remainder of this chapter: cavity quantum electrodynamics (CQED) and cavity optomechanics. Both rely on the technological advances of the latter half of the 20th century to perform quantum measurements via indirect probing, and both make use of an electromagnetic resonator, or cavity, which isolates an electromagnetic field mode to assist in measurement.

1.2 Cavity quantum electrodynamics

Quantum measurement theory is most important at the single-particle level, where backaction perturbations are strongly felt and cannot be averaged away in a statistical ensemble. Additionally, weak measurements (those that do not strongly project an object into a certain state, but rather perturb it minimally) are more reliant on the theory, since they permit the system to continue its evolution after it has been measured. Braginsky et al. [6] identify the historical turning point for application of quantum measurement theory:

> *Although the main principles of the field were elaborated in the 1930s by Bohr, Schroedinger, Heisenberg, von Neumann and Mandelstam, it was not until the 1980s that technology became sufficiently advanced to allow its application in real experiments.*

[2]Dirac made the distinction between "big" and "small" objects in his treatment of the measurement problem, assigning the former to the classical realm, where measurement disturbances could be neglected, and the latter to the quantum realm, where they could not [3].

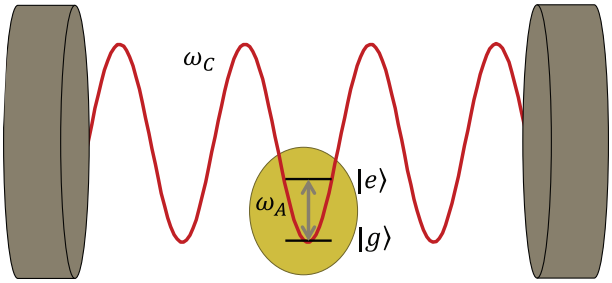

Figure 1.2: Overlapping a single electromagnetic field mode isolated by an optical cavity with the electric dipole moment of a two-level atom realizes the Jaynes-Cummings Hamiltonian. Red curve indicates electric field and circles are atom's ground and excited electronic states.

The 1970's and 80's brought the production of monophotonic light states [7, 8] and the ability to trap single atoms and ions [9, 10]. These single light and matter particles could then be subjected to repeated measurements, with the evolution between measurements governed by quantum measurement theory.

Among the simplest quantum measurement interactions one can consider is that between a two-level system and a harmonic oscillator[3]. This basic interaction is exactly the interplay realized in CQED (Fig. 1.2), where the ground and excited states of an atom play the role of the two-level system which couples to a resonant mode of an electromagnetic cavity. Such coupling was first isolated and measured in the 1980's (Serge Haroche summarizes the early days of CQED in his Nobel acceptance speech [12]). Tremendous experimental effort resulted in the realization the Jaynes-Cummings Hamiltonian [13], which was originally constructed in order to compare the fully quantum and semiclassical treatments of spontaneous emission in masers, and then reappropriated as a simple and accurate description of CQED dynamics[4].

The Hamiltonian itself can be divided into three terms.

$$\begin{aligned} H_{\mathrm{JC}} &= H_a + H_c + H_{ca} \\ &= \frac{1}{2}\hbar\omega_a\hat{\sigma}_z + \hbar\omega_c\hat{a}^\dagger\hat{a} + \hbar g_0\left[\hat{\sigma}_+\hat{a} + \hat{a}^\dagger\hat{\sigma}_-\right] \end{aligned} \tag{1.1}$$

The first term gives the energy of the two-level atom, assuming that a magnetic field oriented along $\hat{z}$ has produced the energy splitting between ground and excited states $\hbar\omega_a$, and with $\hat{\sigma}_z$ the Pauli operator. The second term is the well-known harmonic oscillator Hamiltonian (with vacuum energy set to zero), here representing the energy of the electromagnetic field, with $\hbar\omega_c$ the spacing between optical energy levels and $\hat{a}$ the annihilation operator. Finally, the third term, H_{ca}, is the CQED interaction term, allowing for the exchange of excitations

[3]This introduction to CQED borrows from the work of Haroche and Raimond [11].

[4]It took some 20 years from its publication for the Jaynes-Cummings Hamiltonian to find its proper audience. Frederick Cummings said of the delay, "The silence and zero feedback...for so many years following 1965 was a bit deafening, so I thought it would be best that I go mostly onto other topics... One day in about 1989, I got a tap on the shoulder from a colleague at UCR: 'I saw your name on the title of a paper'."[14]

between the field and the atom at a rate g_0. This interaction results in a hybridization of the states of the two elements, creating an avoided crossing in their energy spectrum given by $\Delta E_{\mathrm{JC}} = \hbar\sqrt{\Delta_{ca}^2 + 4g_0^2}$. Here, $\Delta_{ca} = \omega_c - \omega_a$ is the relative detuning of the light from the atomic transition. The coupling rate g_0, also called the vacuum Rabi splitting, is found to be the product of the dipole matrix element of the atomic transition, d, with the cavity mode electric field strength E_0 (which depends on the cavity mode volume and optical frequency), modified by the overlap of the field with the atomic dipole: $g_0 = dE_0\boldsymbol{\epsilon_a}^* \cdot \boldsymbol{\epsilon_c}/\hbar$. $\boldsymbol{\epsilon_a}$ and $\boldsymbol{\epsilon_c}$ are polarization unit vectors for the atomic transition and the cavity electric field, respectively. In the Heisenberg picture, H_{ca} actually contains terms that oscillate both at $\omega_c - \omega_a$ and at $\omega_c + \omega_a$, with the latter being eliminated under the rotating wave approximation.

The relative contributions of g_0 and Δ_{ca} to ΔE_{JC} set the two limits of CQED coupling. When $\Delta_{ca} \ll g_0$, the atom can easily absorb a photon and change its state. This limit is thus appropriately called the absorptive regime. By contrast, when $\Delta_{ca} \gg g_0$, the light does not excite an atomic transition, but rather shifts the atomic energy levels slightly. In complementary fashion, the energy levels of the optical field are shifted by the presence of the atom, effectively altering the optical path within the cavity and thus changing its resonance frequency. This is the dispersive regime of CQED, and choosing such a detuning Δ_{ca} allows for weak probing of either the light by the atom or the atom by the light.

CQED coupling is now realized using many cavity geometries with different kinds of two-level systems (among them Rydberg atoms [12] and ions [15, 16]), requiring varying electromagnetic energy scales. Its close cousin, circuit QED [17], couples artificial atoms to microwave circuits such that the Jaynes-Cummings Hamiltonian is again realized. When the two-level system is harmonically confined within the cavity, as is the case for some neutral atom and ion experiments, the particle's motion can alter the CQED coupling. Though at first this additional degree of freedom may seem like a hindrance to quantum measurement pursuits, the remainder of this thesis will explore the kinds of measurements such motionally inflected coupling permits.

1.3 Cavity optomechanics

When motion intrudes on a CQED measurement, as is the case for a harmonically suspended atom coupled to a cavity mode, the interaction now depends on an additional oscillator mode, this time mechanical rather than electromagnetic. This comes about because the CQED coupling rate g_0 acquires a dependence on the position of the atom. In the dispersive regime, and assuming that the phonon/photon excitation number is conserved (consistent with the rotating wave approximation), the Jaynes-Cummings interaction term becomes $H_{ca} = \hbar g_0(z)\hat{a}^\dagger\hat{a}\hat{\sigma}_z$. We can describe the atom's position, z, in terms of bosonic field operators like those used for the quadratures $\hat{X}_{\mathrm{AM}}$ and $\hat{X}_{\mathrm{PM}}$ that we built at the beginning of this chapter, with

$$\hat{z} = z_{\mathrm{HO}}\left(\hat{b}^\dagger + \hat{b}\right) \tag{1.2}$$

describing the position fluctuations atop some classical displacement[5]. The characteristic harmonic oscillator length is $z_{\mathrm{HO}} = \sqrt{\frac{\hbar}{2m\omega_m}}$ for an oscillator of mass m and resonance frequency ω_m. If we assume that the system consists of a ground state atom and n photons in the cavity on average, such that the eigenstates of the coupled system can be written as $|g(e), n\rangle$ for the ground (excited) state, then $\langle \hat{a}^\dagger \hat{a} \hat{\sigma}_z \rangle = \langle e, n \left| \hat{a}^\dagger \hat{a} \hat{\sigma}_z \right| g, n-1 \rangle = -n/2 = -\langle \hat{a}^\dagger \hat{a} \rangle /2$. Finally the interaction term, $H_{ca} = -\hbar g_0(\hat{z}) \hat{a}^\dagger \hat{a}/2$, begins to look like one useful for a new kind of measurement, more similar to that depicted in the cartoon in Fig. 1.1. By pushing far to the dispersive regime, where atomic excitation is unlikely, we have isolated motion as the driver of the dynamics of the light field.

Such interplay between cavity light and mechanical motion is called "cavity optomechanics". I have just described a special case of its realization through the motional degree of freedom for a two-level system in CQED. However, in practice, the cavity optomechanical interaction can be realized any time there is dispersive coupling between a mechanical degree of freedom and a cavity field (See Fig. 1.3), such that the cavity mode frequency can be expanded in terms of its dependence on the position of the mechanical element: $\omega_c(z) = \omega_c(z=0) + z\partial\omega_c/\partial z + z^2\partial^2\omega_c/\partial z^2 + \ldots$. In this dissertation, I will focus on terms only up to first order in z in this expansion, assuming therefore that the optomechanical coupling, $g_{\mathrm{om}} = z_{\mathrm{HO}}\partial\omega_c/\partial\hat{z}$, is constant and describes the frequency shift per unit displacement of the mechanical oscillator about some static displacement.

Assuming the linear expansion of ω_c and substituting Eq. 1.2, we recover a cavity optomechanics Hamiltonian of the form:

$$\begin{aligned} H_{\mathrm{om}} &= H_m + H_c + H_{cm} \\ &= \hbar\omega_m \hat{b}^\dagger \hat{b} + \hbar\omega_c \hat{a}^\dagger \hat{a} - \hbar g_{\mathrm{om}} \hat{a}^\dagger \hat{a} \left(\hat{b} + \hat{b}^\dagger \right). \end{aligned} \tag{1.3}$$

As was the case with the CQED interaction, this optomechanical interaction should work both ways. As the oscillator position alters the cavity resonance frequency, so too should the cavity light alter the position of the oscillator.

But is this second effect realistic? When we consider two canonical optomechanical geometries, those shown in Fig. 1.3, it seems unlikely. The left schematic is of an optical cavity with one mirror free to move in such a way that the cavity length will change. Such a scenario is a simplification of the enormous interferometers built to detect gravitational waves [18]. Isolated as they are from seismic vibrations, the giant mirrors in these observatories are free to move, even as they are subjected to large amounts of circulating light. Questions about the possible backaction of the light on the mirrors motivated early investigations of cavity optomechanics, leading to a variety of tabletop experiments (Kippenberg and Vahala [19] and Aspelmeyer et al. [20] provide good reviews) to investigate optomechanics predictions.

One major advance in the field was the realization that the movable object need not be one of the mirrors. Thompson et al. [21] demonstrated that a partially reflective object

[5] I am not using a factor of $\sqrt{2}$ in my definition of $\hat{z}$ so as to be consistent with later chapters of this dissertation and with some of our publications. Without this factor, the commutator between $\hat{z}$ and the momentum operator $\hat{p} = i\left(\hat{b}^\dagger - \hat{b}\right)$ is $[\hat{z}, \hat{p}] = 2i$.

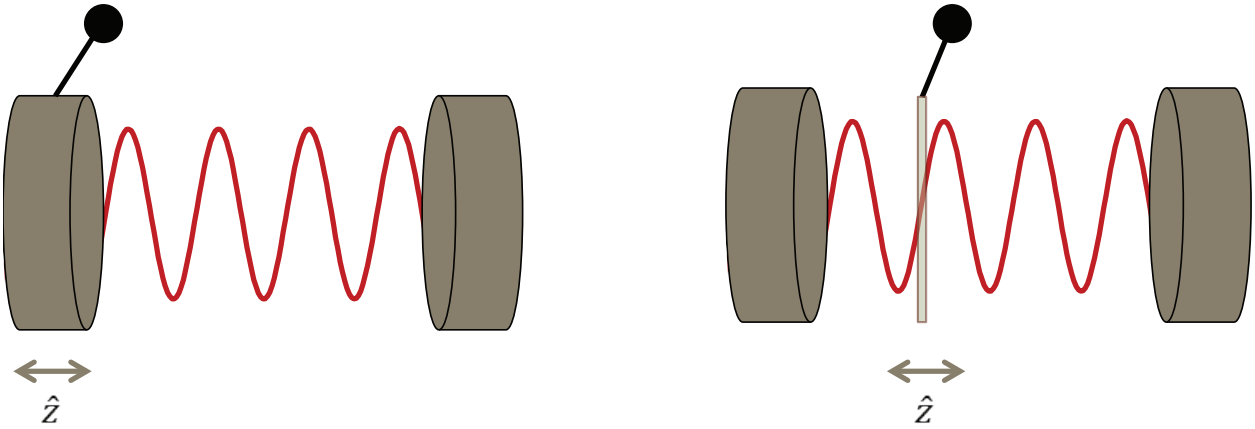

Figure 1.3: The canonical cavity optomechanical system (left) couples the position of a movable end mirror to a field resonant within the cavity. An alternative geometry, called "membrane-in-the-middle" (right), realizes the same optomechanical interaction using fixed mirrors and a partially-reflective element within the cavity that is free to move.

within the cavity, if positioned appropriately and allowed to move (as shown on the right side of Fig. 1.3), could realize the same optomechanical Hamiltonian. This is known as a "membrane-in-the-middle" geometry. By releasing experimentalists from the requirement of creating mirrors that are both high quality reflectors of light and also high quality mechanical oscillators, in favor of inserting more accommodating elements like silicon nitride membranes, this alternative option has contributed to numerous experimental advances.

Another important consideration for realizing the optomechanical interaction is temperature. Radiation presure-driven motion is always a small effect, and it can be easily swamped by thermal motion of the oscillator. Experiments in cavity optomechanics, then, often become exercises in the cooling and quieting of mechanical motion. In this sense, an approach that recalls CQED by employing atoms as mechanical elements has an advantage. The field of ultracold atomic physics has a long and well-trodden history of cooling atoms [22] and ions [23] to their electronic and motional ground states. The experimental apparatus upon which this dissertation is built does just that, placing ground-state atoms inside a cavity and observing the interaction between their motional modes and the cavity field. I will discuss our cavity optomechanics platform in greater detail in Ch. 2.

Cavity optomechanics has blossomed from an offshoot of gravitational wave observatories to its own branch of quantum optics experiments (see Aspelmeyer et al. [20] for a recent review). As in CQED, there now exist numerous cavity-oscillator geometries that can test the mechanics of quantum measurement (or the measurement of quantum mechanics). To date, experiments have demonstrated such effects as cavity cooling of mechanics [24] even to the motional ground state [25], the squeezing of light [26–28] and of mechanical motion [29], and entanglement between mechanical motion and an electromagnetic field [30]. Still there are outstanding goals yet to be achieved, though ever-improving experimental control

suggests that tests of quantum gravity [31] or classical decoherence [32], for example, are not far off.

1.4 Combining the elements

I joined the effort for performing quantum measurement using atomic cavity optomechanics in the fall of 2010, the same year that ground-state cooling of a macroscopic object [33] was voted by AAAS as the "Breakthrough of the Year", galvanizing the optomechanics community in its quest to observe quantum effects. It was a time of excitement, too, for the cavity optomechanics experiment embedded in Dan Stamper-Kurn's Ultracold Atomic Physics group at UC Berkeley. The apparatus that graduate students Tom Purdy and Dan Brooks had designed and built (called "E3" within the group) to combine the effects of CQED and cavity optomechanics was functioning and had produced results confirming its ability to isolate and measure optomechanical interactions [34] between the center-of-mass motion of a cloud of rubidium atoms and a laser field within a high-finesse cavity. Now Dan, graduate student Thierry Botter, and postdoc Nathan Brahms, were excited to take advantage of the very cold mechanical oscillator to measure an effect long predicted but never demonstrated: ponderomotive squeezing, the mechanically-mediated reduction of optical fluctuations below the vacuum limit.

My introduction to cold atomic physics in general and to E3 in particular came during the pursuit of this measurement [26]. It took many hands to maintain the stability of the apparatus through the long session of data taking. One of my contributions was a wavemeter feedback scheme for long-term laser frequency stabilization that I will describe in Ch. 2. In the years since, we have revisited the theory of ponderomotive squeezing and have taken some exploratory data to understand how it changes with experimental parameters, as I will describe in Ch. 4. I enjoyed two years of collaboration with Dan, Thierry, and Nathan, taking advantage of their wealth of experience and their patient teaching as we explored optomechanical calorimetry [35] and measurements in an optical superlattice [36], a new experimental tool I will discuss in Ch. 2. Soon after their departure, a new postdoc, Nicolas Spethmann, joined me just as we began measurements of force sensitivity [37], an experiment that benefited from the contributions of undergraduate Maryrose Barrios. For this experiment, we had to develop the technique of calibrated force application using a superlattice and new analysis techniques, described in Ch. 3. Accompanied by a new graduate student, Jonathan Kohler, we next set out to explore multi-oscillator optomechanics [38]. Lukas Buchmann, a theory postdoc, helped us to understand the cavity-mediated coupling between the oscillators and guided us through our theoretical investigation of a new form of optical squeezing: complex squeezing [39]. I include a theoretical description of the effect in Ch. 5 that differs from that in Buchmann et al. [39] and some early experimental efforts to observe complex squeezing. Throughout my time, I have benefited from the guidance and encouragement of Dan Stamper-Kurn and the assistance and wisdom of my colleagues from the other experiments within the Ultracold group as well. Now, as Nicolas and I prepare to

leave E3, Jonathan has already tuned the apparatus to couple atomic spin dynamics to cavity light, a novel interaction that has been termed "spin optodynamics" [40] and will allow for analogous measurements that can surpass the limitations of atomic mechanical oscillators.

This dissertation will describe three of the quantum measurement experiments performed (or in one case, proposed) during my tenure in the Ultracold group. I have chosen to focus on experiments that emphasize the nature of measurement backaction: how it can be detected, tuned, and perhaps, through careful accounting, avoided. This follows a trend of recent work in quantum optics measurement (both theoretical [6, 41, 42] and experimental [43]) investigating whether and where we can move backaction to improve upon limits.

Chapter 2 will describe the apparatus in greater detail and step through some of the technologies we have introduced that allow access to new limits of quantum measurement. Of particular importance are tools that permit us to assemble statistical ensembles by exerting stabilizing influences over the days and sometimes weeks when we must acquire data in an unchanging environment. Chapter 3 will describe a specific quantum measurement these tools allow us to perform – measuring forces near the Standard Quantum Limit. This lower bound on force sensitivity is the result of a careful balance of measurement imprecision from probe fluctuations and the additional uncertainty introduced by the same probe through measurement backaction. Chapter 4 introduces the concept of ponderomotive squeezing, including our experimental realization of the effect. Chapter 5 builds and generalizes upon the concepts in Ch. 4 to develop the concept of complex squeezing, and offers prospects for its application to quantum measurement.

Chapter 2

Tools

Here come real stars to fill the upper skies,
And here on earth come emulating flies,
That though they never equal stars in size,
(And they were never really stars at heart)
Achieve at times a very star-like start.
Only, of course, they can't sustain the part.

Robert Frost, "Fireflies in the Garden", 1928

2.1 Introduction

Performing an experiment that exhibits the characteristics of quantum measurement requires fine control of the environment. In Ch. 1, I described methods of separating quantum systems from classical observers so as to be sensitive to the effects of quantum limits. This chapter will review some of the tools used in our atomic cavity optomechanics experiment, particularly highlighting those relevant for experimental realizations of quantum-limited force sensing, ponderomotive squeezing, and complex squeezing, as these efforts will be discussed in later chapters. First, I will describe the atom chip and optical cavity that generate our optomechanical interaction. Then, I will detail the installation and use of an optical fiber-switch and wavemeter-based lock for optical frequency stability necessary for multi-day data acquisition. Next, I will give an overview of the superlattice potential we use to separate spectrally mechanical oscillators and how it can be additionally employed to apply well-calibrated forces to the oscillators. Finally, I will introduce our experimental optical heterodyne detection scheme and phase-insensitive heterodyne lock for data acquisition.

2.2 Atom chip and optical cavity

In Ch. 1 I introduced the concepts of cavity QED and cavity optomechanics, describing how a two-level atom coupled to a cavity could, through its mechanical degree of freedom, realize both CQED and cavity optomechanical couplings. I took the time to describe both CQED and cavity optomechanics interactions because the experimental system employed throughout this dissertation is a combination of the two.

The apparatus we use for investigating quantum measurement with atomic cavity optomechanics was expertly designed and built by Tom Purdy and Dan Brooks, as documented in Tom's dissertation [44]. That the apparatus has continued to run beautifully for so many years is a testament to their good planning and technical prowess. Then and now, each experiment begins with the a spray of rubidium-87 atoms into an ultrahigh-vacuum chamber. The spray comes from an alkali metal dispenser[1] containing a stable salt that releases rubidium gas when the dispenser is heated by an applied dc current. The first step of a multistage cooling and trapping procedure (shown in Fig. 2.1) is to capture some of these atoms in a magneto-optical trap (MOT). Use of a MOT is the first indication of our experimental requirement for ultrahigh vacuum. Within the MOT, the atoms are cooled from 300 K down more than 6 orders of magnitude in temperature, enough so that they cannot escape the confines of their trapping potentials. However, a particle not subjected to the same cooling could easily collide with a trapped Rb atom and impart enough energy to free it from its trap. Thus, if we want to be able to collect a large sample of atoms in the MOT over many seconds, we must limit the number of disruptive particles present.

The steel vacuum chamber that encloses the atom chip-cavity setup has ports for electrical feedthroughs (important for the signals that produce chip-based magnetic fields and lock the cavity), vacuum pumps, and optical access to the experimental procedure. Optical access allows us to characterize the temperature of the atoms at each stage of their preparation, extrapolating via time-of-flight measurements[2] to determine the size and temperature of the cloud in each kind of trap.

After the MOT stage, the atoms are transferred (via a second MOT stage during which they are compressed, cooled through forced RF evaporation, and optically pumped into the $|F = 2, m_F = -2\rangle$ state) to a magnetic trap generated by wires on an atom chip. The atom chip is crucial to the measurements I will describe in this dissertation because it allows for the application of very strong magnetic field gradients that can compress the atomic cloud to dimensions smaller than an optical wavelength. When combined with an external bias field, a single current-carrying wire can produce a magnetic field gradient $\nabla B \propto I/r^2$, where r is the distance from and I is the current through the wire. Proximity to the wire is therefore essential for strong gradients. The atom chip in E3 is placed very close to the atoms and still supports substantial currents through its wires, with magnetic traps approximately 100

[1] SAES Getters rubidium dispensers

[2] A time-of-flight measurement gives the temperature of an atomic cloud by comparing the size of the cloud as a function of time since it was released from a trap to a temperature-dependent expansion model. Hot clouds expand faster than cold clouds.

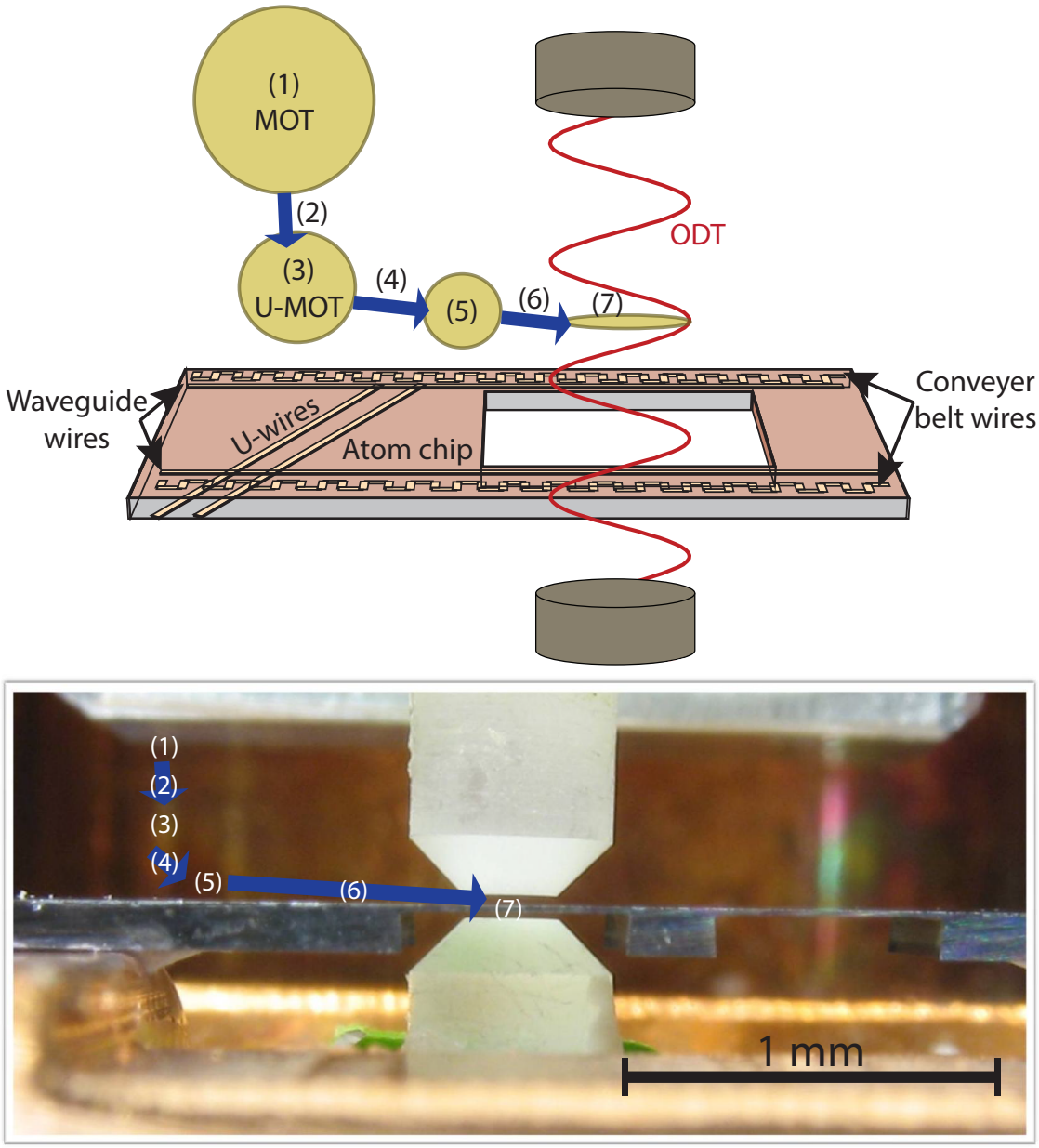

Figure 2.1: Schematic (top, not to scale) and photograph (bottom) of the atom chip and cavity. The procedure of creating an atomic optomechanical sample is: 1) Load MOT from background vapor. 2) Transfer to U-MOT with magnetic fields produced by U-wires on chip. 3) Compress, cool with evaporation and polarization gradient cooling, and optically pump atoms to magnetically trappable state. 4) Transfer to magnetic trap produced by waveguide and conveyer-belt wires. 5) Translate magnetic trap toward optical cavity by modulating currents in chip wires. 6) Use chip-based and bias fields to position atoms at desired location along cavity axis, perform compression and evaporative cooling before turning off magnetic traps as optical traps are ramped on. 7) Perform optical evaporative cooling by temporarily reducing lattice depth. Photograph by Tom Purdy.

microns from the chip surface and currents of a few Amperes. The first in the sequence of magnetic traps generated by the chip, however, is large and shallow, so that it overlaps well with the large and shallow MOT, optimizing the handoff of the atoms by reducing heating and losses. Once the atoms are fully in the chip's control, the currents through the chip wires are modulated so as to translate the magnetic field minimum, and therefore the atomic cloud, to a region between the mirrors of the optical cavity, as depicted in Fig. 2.1.

In the final part of this translation, we additionally use magnetic bias fields produced by large magnetic coils outside of the vacuum chamber to help the chip direct the atoms carefully to overlap with a region of interest along the cavity. Our goal is to isolate atoms to a particular single site of a one-dimensional optical lattice produced by a standing-wave of light within the optical cavity, an important factor in tuning optomechanical coupling, as I will soon explain. To this end, the atom chip's final contribution is to compress further the cloud before we apply another forced RF evaporation. This second stage of cooling also ensures that the all of the atoms are in the ground state of the optical lattice potential within the cavity once the chip-based trap is turned off. Occupying the ground state of mechanical motion is the first step for each of the quantum measurements discussed in this dissertation, as warm oscillators can obscure quantum effects. We will see, for example, that even slight excursions from the ground state increase the mechanical linewidth due to the anharmonic nature of the optical potential.

The cavity itself is a high-finesse near-planar Fabry-Pérot resonator with the output mirror eight times more transmissive than the input mirror. Both mirrors have a radius of curvature of 5 cm and are separated by 250 μm. Each mirror has a multilayer dielectric coating that makes it maximally reflective for light near 780 nm, the D2 transition wavelength of ^{87}Rb, where the cavity has a measured half-linewidth of $\kappa = 2\pi \times 1.82$ MHz. An important parameter of the cavity for its use in CQED and cavity optomechanics experiments is the mode waist, since for a near-planar cavity the CQED coupling rate g_0 is inversely proportional to this value. With a mode waist of 25 μm, our cavity allows us to reach the strong-coupling regime of CQED, where the CQED cooperativity $C = g_0^2/2\kappa\gamma > 1$, with γ the full-linewidth of the atomic transition.

The one-dimensional optical lattice potential within the cavity is generated by one or two standing-waves of laser light resonant with separate TEM_{00} modes of the cavity. All of the lasers that enter the cavity have been previously frequency-referenced to each other by a transfer cavity locking chain, which I will discuss later in this chapter. The trapping lasers have wavelengths of approximately 850 nm, very far detuned from the atomic transition so as to produce an optical dipole trapping (ODT) potential. Once the atoms are in the all-optical trap, we perform an additional stage of evaporative cooling to bring them to their final temperature. We have found that this final evaporation is necessary to limit the number of atoms heated out of the motional ground state, especially in cases where we introduce a second trap laser which seems to contribute some additional heating, as quantified by time-of-flight measurements and sideband asymmetry thermometry [35]. This heating manifests as a broadening of the mechanical linewidth. In Ch. 3, we will see that in some cases we have sufficient resolution of this broadening to count the atoms that have been heated out of the

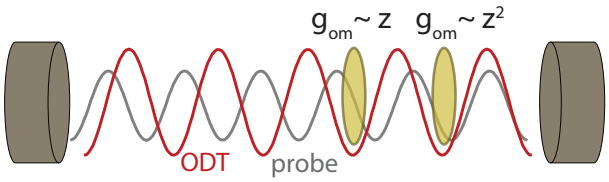

Figure 2.2: Because of incommensurate wavelengths of trap light (850 nm) and probe light (780 nm), the potential minima (intensity maxima) of the trap sometimes align with a local probe field that changes linearly and sometimes with one that changes quadratically.

ground state. Optical evaporative cooling also serves to eliminate most of the residual atoms in wells neighboring our lattice site of interest. Since those neighboring sites have slightly different optomechanical coupling rates, we are therefore able to evaporate to a more pure linear optomechanical interaction.

The cooling, trapping, transport, and placement stages complete, the atoms finally are allowed to interact with a weak probe we introduce as yet another standing wave within the cavity (see Fig. 2.2). Since the trap and probe fields are of incommensurate wavelength, some anti-nodes of the trap light (which attract the atoms and define the potential wells) overlap with regions of the probe field that change linearly with position along the cavity axis, z, others with a quadratically changing probe field, and others with some combination of the two.

The probe frequency is close to the atoms' $|F = 2, m_F = -2\rangle \rightarrow |F = 3, m_F = -3\rangle$ transition, yet still detuned sufficiently to be well within the dispersive limit of CQED. In Ch. 1 I described CQED coupling for a single atom in the dispersive limit, and showed how an optomechanical interaction could come about. At this point in our experimental procedure, we have a few thousand atoms trapped in one to two sites of the optical lattice. The Tavis-Cummings Hamiltonian [45] is the expansion of the Jaynes-Cummings Hamiltonian to the many-atom case, such that $g_0 \rightarrow \sum_{i=1}^{N} g_0^2(z_i)$. Even assuming that the atoms are non-interacting, it is not obvious whether the system should behave as it does in the single-atom case, since each atom may move in any direction relative to the others. Kater Murch's thesis [46] provides a careful derivation of how optomechanical coupling to the center-of-mass motion of the atoms within the cavity comes about from the Tavis-Cummings CQED interaction. Though there are as many motional modes along the cavity axis as there are atoms, the degeneracy of these modes is lifted by the presence of a static optical spring shift proportional to the number of atoms, and the collective center-of-mass mode is selected as the fundamental eigenmode of the system. We refer to this motional mode as our atomic "mechanical oscillator", and observe that it behaves according to the same equations of motion as apply to solid-state mechanical oscillators [34].

Though the dynamics we observe suggest that this picture is mostly true, we find that in some circumstances we must reexamine the assumptions made in concluding that all of the atoms contribute to the collective ground-state center-of-mass mode. In particular, we typically assume that excursions of the atoms are small compared to both the trap

and the probe wavelengths, justified for ground-state atoms with $z_{\mathrm{HO}} \ll k$ where k is the optical wavenumber. This allows us to simplify the spatial-dependence of the coupling as $g_0^2 \sin^2(k_p z) \to g_0^2 k_p z$. In practice, however, we observe that in certain settings a substantial fraction of the atoms explore greater and greater extents of the trap, no longer settled in their ground states. This requires us to consider higher orders in the expansion of g_{om}. Recall that in transitioning from the CQED to the cavity optomechanics Hamiltonian in Ch. 1, we assumed that $|g(e), n\rangle$ were the only system eigenstates available. This is no longer the case when additional mechanical excitations can occur. These excitations contribute to a broadening of the mechanical linewidth that we can capture by expanding to higher order the approximations made in deriving the linear optomechanical Hamiltonian for our system. I will discuss the effects of this in greater detail in Ch. 3.

As in the case of, for example, a silicon nitride membrane [21], the initial position of our atoms along the cavity axis is of great importance for determining their coupling to the probe field. The linear optomechanical coupling described in Ch. 1 is most nearly achieved at the location of linear probe intensity gradient, such that as the atoms make small excursions from the minimum of their potential well they encounter probe power that is proportional to their displacement. Again, in practice, we are imperfect. We have a limited number of lattice sites from which to choose, none of which will overlap precisely with the node of the probe's electric field (we are especially sensitive to this when we try to match the coupling of two mechanical oscillators in Spethmann et al. [38]). Nonetheless, the atom chip's dexterity in placing the atoms allows us to optimize for the linear case. We can calibrate the coupling observed in various lattice sites by placing the atoms at a variety of locations along the cavity axis and measuring the resulting cavity frequency shift, a technique I will expand upon in Ch. 3.

Finally, I will point out the ease with which we can adjust the optomechanical cooperativity $C_{\mathrm{om}} = 4\bar{n} g_{\mathrm{om}}^2/\kappa\Gamma$ (where Γ is the mechanical linewidth and $g_{\mathrm{om}} = N_a g_0^2 k_p z_{\mathrm{HO}}/\Delta_{ca}$ is the optomechanical coupling rate, with N_a the atom number, k_p the probe wavenumber, and z_{HO} the harmonic oscillator length) in our system by changing either the average probe photon number $\bar{n}$ or its detuning from atomic resonance Δ_{ca}. This tunability is important for investigating the effects of measurement backaction, as will be seen especially in Ch. 3.

2.3 Fiber switch

Two aspects of the quantum measurements we perform with our apparatus necessitate long-term stability of experimental conditions. Because many of the signals we measure are small when compared to the various noise sources that surround them, the experimental averaging time must surpass the signal coherence time by at least the noise-to-signal ratio. Additionally, we construct measurements of the quantum mechanical state through ensemble averages, requiring many realizations of the same experiment to fill a region in phase space. However, because of limited trapping times and steady heating of our oscillator due to its coupling to other motional modes, each experimental realization is limited to measurement

records of only about 10 ms, after which the atomic oscillator must be discarded and the preparation and measurement process begun anew. The experimental duty cycle is usually 30-40 seconds. Thus, though the signals we measure are usually at frequencies of 100 kHz with decay rates of a few kHz (meaning their coherence typically lasts less than a millisecond), we require the stability of optical frequencies, for example, over weeks at a time.

A common way to stabilize an optical frequency, particularly of a laser which will be employed in the probing of atoms, is to reference the frequency to an atomic transition [47]. We use such stabilization for the cooling lasers that prepare our atomic sample. This light needs to be detuned at most by a few hundred MHz from the atomic transition, an offset which can be achieved using standard acousto-optic modulators. The lasers that we inject into the cavity to trap and probe the atoms, however, are farther detuned from resonances of interest (10's of THz and 10's of GHz offset, respectively). Furthermore, the sensitivity of the trapping and measurement to small frequency differences is not acute. Nonetheless, it is important for our experiment that we stabilize the cavity lasers relative to each other and to the cavity, and that the probe light frequency not drift on the order of GHz over the period of data taking.

The relative stabilization of probing and trapping lasers is achieved by referencing them to a common "transfer cavity"[3] using a Pound-Drever-Hall lock. The length of the "science cavity" used for optomechanical measurement is subsequently locked to one of the trapping lasers, completing the chain of frequency referencing. Thus the lasers and the science cavity itself all follow any drifts in the length of the transfer cavity. During measurements of ponderomotive squeezing (presented in Ch. 4), we noticed that the long-term changes in the length of the transfer cavity occasionally allowed the probe light frequency to drift up to several GHz from week to week, as measured on a high precision wavemeter[4]. Not only were these frequency changes enough to affect the cooperativity of our measurements, but also they would frequently drag the laser frequency to the edge of the range of the Pound-Drever-Hall lock, such that the referencing would be lost and the lock chain would have to be reestablished.

To remedy this, we introduced an additional slow feedback system (see Fig. 2.3) to stabilize the long-term drifts of probe frequency. In addition to selecting a small portion of probe light to use for the transfer cavity lock, we send some light to a 12 channel serial-controlled optical fiber switch [5] that directs the input channels to the wavemeter. We introduce a digital proportional-integral-derivative (PID) controller that compares the wavemeter monitor to a frequency setpoint and produces an error signal with proportional and integral gain that can be tuned in-loop. We then feed the error signal back to a thermoelectric cooling (TEC) element attached to the the transfer cavity. The TEC can control the temperature, and therefore the length, of the cavity, so as to restrict one of its modes (the one resonant with the probe) to maintain the probe's frequency setpoint.

[3]Toptica FPI 100 Confocal Fabry-Pérot Interferometer, inside an evacuated chamber, set atop Sorbothane for vibrational isolation

[4]Toptica WS-7 HighFinesse Wavelength Meter

[5]DiCon Fiberoptics MEMS 1×12 optical switch, customized for near IR wavelength range

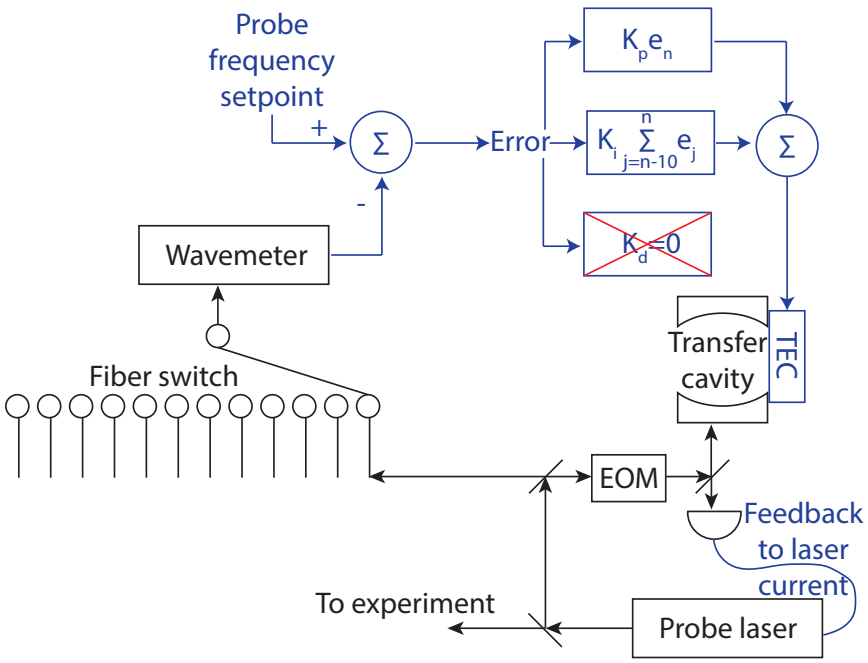

Figure 2.3: Wavemeter lock schematic. The fiber switch receives light from the probe laser that has been referenced to the transfer cavity. The switch then directs the light to the high precision wavemeter. Wavelength measurements made on the fiber switch channel of interest are directed to a digital PI control (no derivative gain) which feeds back to the TEC that adjusts the transfer cavity length. In this diagram, blue components signify electrical connections, and black components are optical. An additional digital system controls the switch position, typically allowing it to cycle constantly through the open channels.

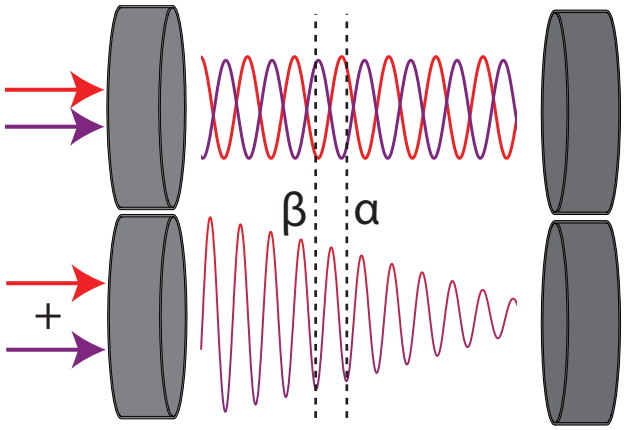

Figure 2.4: Two trapping tones (red and purple, top) are superimposed within the cavity to create an overall superlattice potential (red-purple gradient, bottom) which provides varied trap frequencies at its trapping sites. We can choose a set of neighboring loading sites that maximize spectral separation between α and β so that we can easily resolve their responses and address the oscillators individually.

The fiber-switch allows us to share the functionality of the high precision wavemeter among the several rooms that house our research group. It is usually set to cycle constantly through its input channels in such a way that light piped in from nearby rooms is sampled at rates high enough to allow for slow feedback to be implemented in multiple laboratories. The fiber switch, wavemeter readout, and transfer cavity feedback are all controlled through LabView codes interfacing with the three components through RS-232, USB, and analog output channels, respectively. The feedback protocol is a digital PID controller with gain parameters that can be adjusted in-loop.

2.4 Mechanical superlattice

The task of stabilizing and referencing the cavity lasers is made more difficult by our use of two separate lasers to produce optical lattice potentials, which together combine to form a one-dimensional superlattice. The added ability to create multiple spectrally separate oscillators and apply forces to them individually, though, makes the increased complexity of the experimental apparatus well worth the trouble.

We inject two lasers with wavelengths of approximately 840 nm and 860 nm (red and purple lines in Fig. 2.4) into the cavity. The cavity length is adjusted using feedback to a piezoelectric device upon which one of the cavity mirrors is mounted so that one of the lasers is always resonant with one of the cavity's TEM_{00} modes. Because the lasers have already been referenced to each other on the transfer cavity, both are subsequently resonant with separate TEM_{00} modes of the science cavity. The atoms experience the sum of their intensities, an optical superlattice, with total potential $U(z) = |U_A| \sin^2(k_A z + \phi_A) + |U_B| \sin^2(k_B z + \phi_B)$

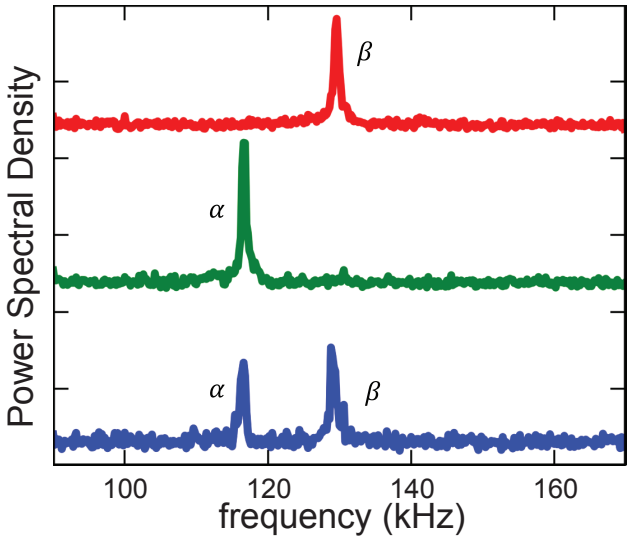

Figure 2.5: Spectra of mechanical response for different loading parameters of the superlattice potential, offset for clarity. By tuning the chip-based magnetic fields when loading atoms into the superlattice and changing the levels of evaporation to vary overall atom number, we can select to load either site α or β or both. We see a clear spectral separation between the sites. Since the mechanical response spectrum also follows the susceptibility to applied force, the distinct peaks mean that we can individually address the oscillators with forces as well.

(where I am neglecting the small contribution of the probe to the optical dipole potential). We can find the minima of the potential, the locations of the trap sites, by solving $\partial U/\partial z = 0$. The minima occur at locations z for which this equality holds:

$$\frac{\partial U_A}{\partial z} = -\frac{\partial U_B}{\partial z}. \tag{2.1}$$

Noting that these derivatives give the force of the optical traps, we recover the (admittedly unsurprising) result that the minima of the superlattice potential are locations for which the forces from the optical fields are equal and opposite, such that $F_A(z) = -F_B(z)$. A careful accounting of the components of force within the superlattice will be necessary in Ch. 3, when we calibrate forces we apply by modulating one of the optical traps.

With incommensurate wavelengths, the two trap lasers produce a superlattice with a trap frequency (assuming harmonic confinement), $\omega_m(z) = \sqrt{-\frac{1}{m}\frac{\partial^2 U}{\partial z}}$, that varies along the cavity axis. In practice, we are able to separate trap frequencies in adjacent sites by as much as 15 kHz, enough to distinguish well the spectra of neighboring oscillators with few kHz linewidths [36].

Figure 2.5 shows power spectral densities for noise-driven oscillators in our superlattice potential. These curves also demonstrate the spectral susceptibility of each oscillator to applied forces. Because the peaks do not overlap, we can modulate the superlattice at the resonance frequency of one oscillator, forcing it strongly, without disrupting the other [36, 38].

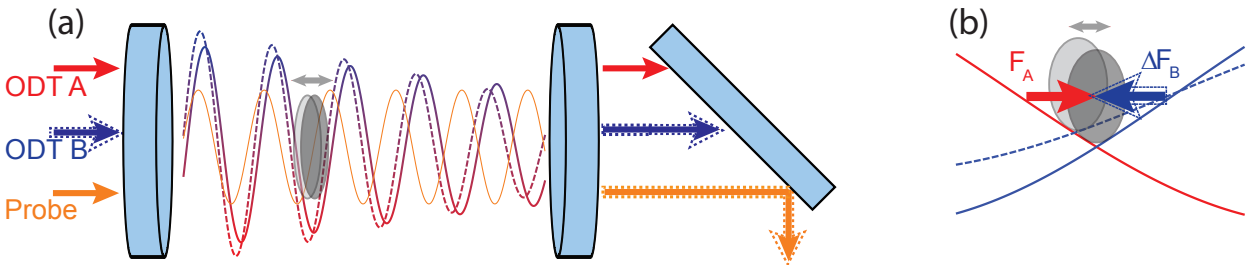

Figure 2.6: Scheme of lattice modulation for applying forces. **(a)** By modulating the amplitude of one trapping laser, we cause the mechanical oscillator to follow the potential minimum as it shifts along the cavity axis. This shift is then imprinted onto the probe. **(b)** A close-up of the trap potential near the atoms yields the components of the force. The two trap lasers provide equal and opposite force against the atoms, and this force changes as the potential minimum shifts.

The superlattice potential therefore provides us with both the spectral separation of and the means to address individually multiple oscillators. Though we can alternatively apply forces to the atoms using the probe light or magnetic fields, we find that forces applied with the superlattice afford us the best control without introducing additional noise or confounding our measurements[6].

I will go into greater quantitative detail about the calibration of the forces applied by modulation of one component of the superlattice in Ch. 3. Here, I offer a schematic representation of force application using an optical lattice in Fig. 2.6. By modulating the power of one lattice component, U_B, we shift the minimum of the entire superlattice along a path that has some non-zero projection along the cavity axis. This is possible because, although the atoms are trapped at an intensity maximum of the total superlattice potential, they actually encounter a linear intensity gradient of each individual trap laser, where $\partial U_A/\partial z = -\partial U_B/\partial z \neq 0$. These intensity gradients produce equal and opposite forces from the two trap lasers, which are modified by the shaking of one of the traps. The resulting motion of the atoms imprints onto the probe light in the usual optomechanical interaction.

2.5 Heterodyne detection

Once the probe light has been allowed to interact with the mechanical oscillator and carry information about its motion out of the cavity, we wish to collect that information from the light. The first measurements made with our apparatus used a detector that counted single photons, gleaning spectral information from the photon arrival times. For a measurement like ponderomotive squeezing, it is advantageous to have phase-sensitive detection, since the signal of interest can appear in the phase of the light. A photon counting detector

[6]When we modulate the probe light in order to apply a force, a record of that modulation will appear in the heterodyne measurement, though this can be taken into account through network analysis, as was performed in Ref. [26].

is completely insensitive to the light's phase. A homodyne receiver, by providing a phase reference in the form of a local oscillator (LO), offers the ability to tune the detection phase[7]. In homodyne detection, the signal of interest (usually modulations on top of some classical carrier wave) is beat with LO light with the same carrier frequency as the signal, realizing an effective Mach-Zehnder interferometer. The relative phase of the LO light determines whether the beat note measured by a photodetector carries information about the phase modulation (PM) or amplitude modulation (AM) of the signal light.

Because the LO and the signal have the same carrier frequency, spectral analysis of the homodyne beat note shows the information of interest at frequencies near dc, with spectral density (assuming the measurement of amplitude fluctuations in the AM quadrature)

$$S_{\mathrm{Hom}}(\omega) = S_{\mathrm{sn}} + 2P_{\mathrm{LO}}P_s\delta(\omega) + P_{\mathrm{mod}}\left[\delta(\omega+\omega_{\mathrm{mod}}) + \delta(\omega-\omega_{\mathrm{mod}})\right], \tag{2.2}$$

where S_{sn} is the shot-noise spectral density, P_{LO} is the power of the LO, P_s the power of the signal, and P_{mod} the power of the modulation of interest at frequency ω_{mod}. This is problematic experimentally, since some unavoidable sources of laboratory noise (LO intensity fluctuations, electrical noise in detectors) occur at low frequencies. Instead, we opt for heterodyne detection by detuning the LO by 10 MHz from the signal. Frequencies around 10 MHz are ideal for our particular experiment because they are well above most noise sources and also above frequencies of experimental interest like the mechanical resonance frequency of the atoms, while remaining low enough that the beat spectrum can be captured by standard photodetectors and oscilloscopes. A heterodyne power spectral density has the form

$$\begin{aligned} S_{\mathrm{Het}}(\omega) =& S_{\mathrm{sn}} + P_{\mathrm{LO}}P_s\left[\delta(\omega-\omega_{\mathrm{Het}}) + \delta(\omega+\omega_{\mathrm{Het}})\right] \\ &+ \frac{P_{\mathrm{mod}}}{2}\Big[\delta(\omega-\omega_{\mathrm{Het}}+\omega_{\mathrm{mod}}) + \delta(\omega-\omega_{\mathrm{Het}}-\omega_{\mathrm{mod}}) \\ &+ \delta(\omega+\omega_{\mathrm{Het}}-\omega_{\mathrm{mod}}) + \delta(\omega+\omega_{\mathrm{Het}}+\omega_{\mathrm{mod}})\Big], \end{aligned} \tag{2.3}$$

The beat note is a large signal at ω_{Het} with the modulations of interest now displaced in frequency to $\omega_{\mathrm{Het}} \pm \omega_{\mathrm{mod}}$. The LO cycles through its phase relative to the signal at a rate set by ω_{Het}. It therefore gathers information about PM half the time and AM half the time. These two sets of information can be disentangled through demodulation of the measurement record.

Because heterodyne detection is designed for sensitivity to small phase differences between the signal and the local oscillator, drifts in path length difference due to thermal fluctuations of optics could spoil the signal of interest. In our case, the signals we are trying to measure occur at frequencies at and above 100 kHz. Environmentally-induced fluctuations in path length should be restricted to much lower frequency bands. In the past, we actively stabilized the path length difference through a phase-lock feedback scheme by inserting a piezo-driven mirror into the LO path (see Fig. 2.7). The additional complexity of this solution made

[7] Thierry Botter's thesis [48] provides a detailed and accessible review of the quantum optics of balanced homodyne detection.

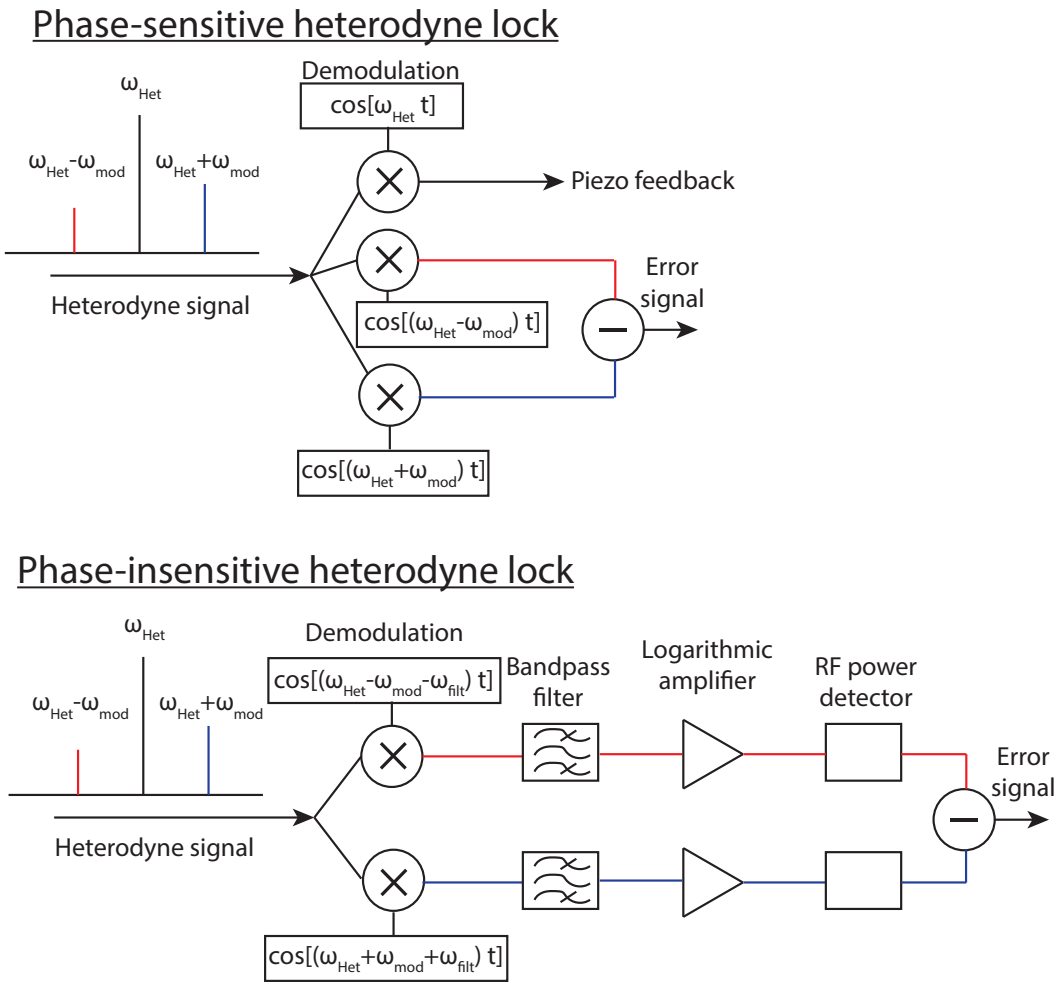

Figure 2.7: Top: old heterodyne lock for referencing probe frequency to cavity frequency. The heterodyne signal is demodulated in parallel three times, once at the heterodyne frequency ω_{Het} to establish an error signal for feedback to a piezo-electrically driven mirror that maintains the relative LO phase, and once each at the modulation sideband frequencies $\omega_{\mathrm{Het}} \pm \omega_{\mathrm{mod}}$ to recover (demodulation-phase-sensitive) power in each sideband. We can then compare the power in each sideband to determine the detuning of the probe. Though all demodulation frequencies are referenced to the same clock, the demodulation phase required for the lock sidebands must be optimized based on detuning. Bottom: new locking scheme that eliminates demodulation phase dependence and piezo-electric driven mirror. Heterodyne signal is now demodulated at an intermediate frequency which falls in the narrow bandpass of an RF filter (Murata ceramic filter, 455 kHz center frequency, 10 kHz stopband) before a logarithmic amplifier and RF power detector select the power in each sideband to compare as before.

the locking chain for experimental operation cumbersome, since the phase of the signal fed into the phase lock had to be adjusted depending on detuning of the probe light. Instead, we moved to correct environmental phase drifts digitally, without bothering to perform any phase-locking of the signal and LO paths. Appendix A describes the process and shows an example of the code we use for demodulation. The choice of digital filters for such a process is important, since errors in quadrature correction could affect the signal we hope to measure.

The heterodyne signal also contains the information we use to stabilize the frequency of the probe laser relative to the cavity resonance. Before the probe is injected into the cavity, we phase-modulate it using an electro-optic modulator (EOM). The resulting sidebands appear in our heterodyne measurement record, where the ratio of the power of the sidebands reveals the location of the probe tone along the spectral slope of the cavity. For example, in Fig. 2.7, the blue sideband is slightly taller than the red sideband, suggesting $\Delta_{pc} = \omega_p - \omega_c < 0$ for probe frequency ω_p. To feed back to the probe frequency, thus maintaining its detuning from cavity resonance during measurements, we direct a copy of the heterodyne signal first through an slightly offset demodulation stage and then to a set of narrow analog filters that isolate the locking sidebands, as shown in Fig. 2.7.

We then use matched pairs of RF logarithmic amplifiers and power detectors to measure the power in each sideband. The difference in the powers is the error signal for our feedback loop. In addition to feeding back to the difference, we also digitally record the derived detuning,

$$\Delta_{pc} = \frac{-\omega_{\mathrm{mod}} + \sqrt{\omega_{\mathrm{mod}}^2 - r^2(\omega_{\mathrm{mod}}^2 + \kappa^2)}}{r}, \tag{2.4}$$

where $r = (S_b - S_r)/(S_b + S_r)$ is the normalized difference between the power in the blue sideband S_b and that in the red sideband S_r, for each experimental realization. This probe frequency locking method is an improvement over a previous version that required analog demodulation of the heterodyne signal. Though we phase-referenced the demodulation signals to the modulating tones used on the EOM, the quadrature rotation imprinted by the cavity at different detunings required us to adjust the demodulation phase regularly. By contrast, a phase-insensitive scheme that only picks out power in a narrow bandwidth around the locking tones is more robust. Regardless of how we generate the error signal, we feed back to an acousto-optic modulator (AOM) that is shared between the signal and LO paths. This is important because in feeding back to the frequency of the probe we do not want to change the relative heterodyne frequency as well.

Figure 2.8 reveals the importance of phase sensitive detection. Optomechanically mediated modulations in the cavity resonance frequency shift the cavity transmission maximum relative to the static probe tone. When the probe light is resonant with the cavity, this has little impact on the amplitude of the light transmitted, but greatly alters the phase. Thus optomechanical signals appear in the PM detection quadrature. Halfway down the slope, at a detuning of the cavity half-linewidth κ, these roles are mostly reversed, and the optomechanical signals appear in the AM. Therefore, for maximal sensitivity to the optomechanical signal, we would choose to detect in the correct output quadrature.

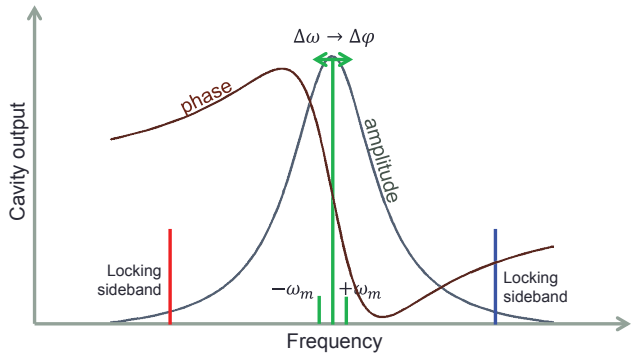

Figure 2.8: The probe light is referenced to the cavity resonance by comparing the power in two locking sidebands. When the probe is resonant with the cavity (equal power sideband condition), the optomechanical signal appears in sidebands at frequencies $\pm\omega_m$ in the PM quadrature. Detuning the probe from cavity resonance allows the optomechanical response to appear in the AM quadrature.

Optical path component	Signal transduction efficiency
Cavity	0.3
Detection path optics	0.9
LO/signal mode matching	0.9
Photodetector quantum efficiency	0.8
Heterodyne penalty	0.5
Total ε	0.1

Table 2.1: Components of overall heterodyne detection efficiency in our optical path, with typical values for their transduction efficiency.

As a final consideration for heterodyne detection, I note the importance of identifying and quantifying all of the loss mechanisms that lead to reduced detection efficiency in our system. Because of its importance for experimental calibration and for generating theory calculations to match our data, we measure (and make improvements to) our detection efficiency daily. Its measured value includes losses due to absorption and scattering out of the cavity, due to absorption by additional optical elements and polarization imperfections along the detection path, due to mode-mismatch between the LO and signal beams when they are combined, and due to the quantum efficiency of the photodiodes used for detection. Finally, because a heterodyne detector, by cycling through AM and PM, measures the wrong quadrature half the time, the overall detection efficiency is reduced by half compared to homodyne. Typical loss values are tabulated in Tab. 2.1. We measured the losses from the cavity once, and do not expect them to change as we have not observed any of the other cavity parameters (linewidth, finesse, etc.) to drift in that time. We check the value for efficiency through the post-cavity optical path every day, and occasionally must adjust beam pointing through, for example, an optical isolator. The mode-matching between the LO and the signal light is the most fickle, requiring frequent optimization by adjusting pointing of one or both beams.

To do so, we observe the steady heterodyne signal on a spectrum analyzer and attempt to maximize the height of the 10 MHz beat note. We have found that the photodetector quantum efficiency has not changed.

Because of the importance of detection efficiency for so many measurements, we have considered ways to improve it. One idea is to build a cavity that is constructed out of optical fibers [49], such that the output coupling efficiency should be excellent. Additionally, we could consider pushing for photodetectors with better quantum efficiency, as detection of infrared photons with total system efficiency of greater than 93% has been reported [50].

Chapter 3

Force Sensitivity Measurement

For such evasive dust
Can make so little clear:
Much less is known than not,
More far than near.

Philip Larkin, "Far Out", 1959

3.1 Introduction

Two properties of our atomic cavity optomechanical system encouraged us of its ability to perform the most precise force and displacement measurements. First, our mechanical oscillator, the center-of-mass mode of the atoms' motion, is cold from its creation. Given the extensive knowledge of cooling and trapping techniques for alkali atoms, creating a ground-state mechanical mode is a relatively easy feat. By the time the atoms are trapped within the confines of our optical cavity, they are already at a temperature of only a few microkelvin, sharing only about one phonon of thermal excitation among thousands of atoms in a 40 μK deep trap. Compare this, for example, to more macroscopic mechanical oscillators that must be placed in dilution refrigerators [33] or addressed with cavity cooling techniques [25] in order to reach the ground state. The advantage of a cold mechanical oscillator is its ability to measure small perturbations that would otherwise be masked by the Brownian motion that comes with coupling to a thermal bath. This is particularly important for force measurements, since the oscillator's motional response to broadband thermal noise is peaked at the same frequencies where it is most susceptible to force noise.

The second advantage of our system is that the oscillator position is well referenced to the probe light. Our atoms are trapped in an optical lattice, such that the relative position of the lattice sites is pinned to our probe by the boundary conditions of an optical cavity (that is, unless we deliberately modulate the lattice, as will be discussed). Should the trap which holds the atoms – and thus the atoms themselves – move due to trembling of the cavity mirrors, the probe light moves along with it, preserving the calibration of the measurement.

This is not to say that the movement of the mirrors does not exert forces on the atoms – it does. However, these forces occur at much lower frequencies than those we care to measure. More important for our measurements is the coupling of the probe light to the atoms at their trapped location, which we must calibrate carefully in order to extract a value of force from the optical record. The optical cavity boundary conditions assure us that this coupling does not change over the duration of the measurement.

The optical lattice also provides isolation from the room temperature environment, since the mechanical support structure, the light, is effectively very cold, despite its prior propagation through a 300 K room. By contrast, experiments with macroscopic oscillators must carefully ensure that the physical tether holding the oscillator in place does not couple in additional mechanical noise or heat. Although optical trapping has been shown to improve oscillator quality factor in solid-state systems [51], ours remains a rather humble $Q = \omega_m/\Gamma \approx 100$. A higher Q, as will be seen when we derive sensitivity equations, would result in improved force sensitivity. We concede this improvement in favor of the ease of low temperature preparation made possible using an atomic center-of-mass mode.

In this chapter I will describe the calibrations and analysis that characterize the force sensing capabilities of our optomechanical system, culminating in measurements near the standard quantum limit (SQL) of force detection. I will first summarize the theoretical underpinnings of the SQL and derive a formula for its value. I will draw a contrast between displacement and force sensitivity. Next I'll detail the experimental calibrations necessary for force application and detection. (Because we had already quantified the optical shot-noise in our experiment in several previous works [26, 35, 36], calibrating the applied force, and assuring ourselves that the calibration remained true throughout, was the main challenge of the experiment.) I will then show how we extract phase-sensitive results from our apparatus. Finally, I will advocate for efforts to overcome the SQL.

3.2 The Standard Quantum Limit

How well can a measuring device resolve a small force? This question has more than just philosophical merit, as many existing technologies rely on the detection of very small forces. Atomic force microscopy, for example, exploits force detection to map surfaces beyond the diffraction limits of optical microscopy [52]. State-of-the-art intertial sensing technologies employ nanofabricated oscillators [53, 54] and even cold atoms [55] to discern minute orientation-dependent accelerations. And before these technologies had ever approached fundamental limits, the designers of the gravitational wave observatories had begun to question the ultimate limits to achievable sensitivities [41].

In Ch. 1 I gave some motivation for the use of CQED and cavity optomechanics for quantum measurement. With these platforms in mind, I will first tell a qualitative story of how the standard quantum limits (SQLs) of force and displacement measurement come about. I will follow this with more detailed derivations.

As just described, one obstacle to sensitive force measurement is a warm detector. Tech-

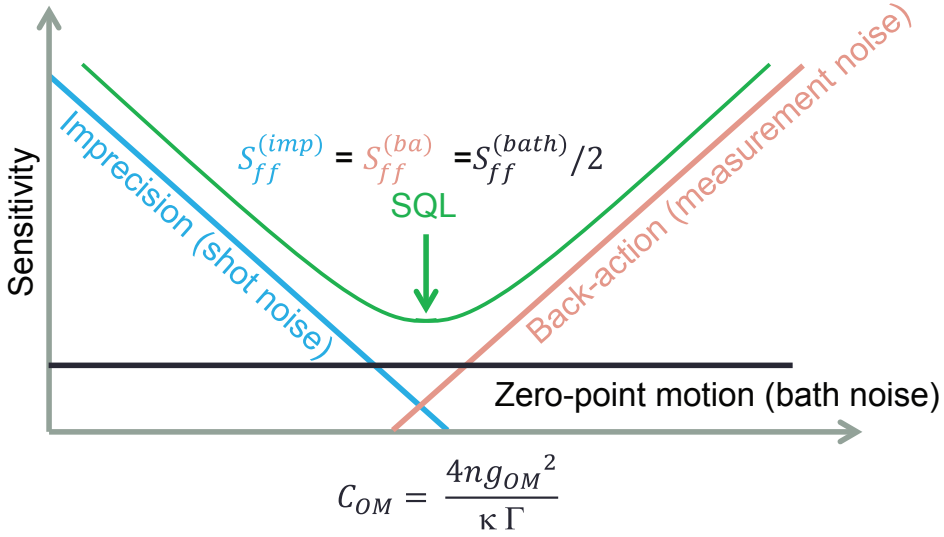

Figure 3.1: The sensitivity (or total measurement imprecision) of an optomechanical measurement of position or force, as a function of measurement strength $C_{\rm om}$ (green curve). Note that lower values of sensitivity are preferred for finer measurement. The three noise sources that contribute to $S_{FF,\rm tot}$ are each plotted separately. The optimal measurement condition occurs where shot-noise imprecision is equal to backaction noise, and defines the SQL.

nical noise affecting either the mechanical oscillator or the probing light can obscure the signal of interest. However, even if every experimental precaution is taken, one is left with fundamental vacuum fluctuations, often referred to as "zero-point motion" for mechanical modes and "shot-noise" for electromagnetic ones. An experimentalist's first instinct might be that a fundamental limit to measurement precision would then be the vacuum noise power. She would be partially right. Consider the black line in Fig. 3.1. It shows a flat lower bound on the sensitivity of an optomechanical measurement for all values of optomechanical cooperativity $C_{\rm om}$ (recall that $C_{\rm om}$ quantifies the measurement strength), and is due to half a phonon's worth of mechanical wiggle that is unavoidable for a ground-level coherent mechanical state. The blue line, on the other hand, represents the shot-noise of the optical probe, which contributes measurement imprecision that now falls off[1] with increasing $C_{\rm om}$. The intuition for this comes from the Poisson statistics of a coherent light beam. If the probe has n photons on average, it also has $\sqrt{n}$ photons of shot-noise. Since $C_{\rm om} \propto n$, as $C_{\rm om}$ increases, the relative contribution of shot-noise (equal to $\sqrt{n}/n$) falls.

Now the experimentalist might imagine that as long as she measures her system strongly enough, shot-noise imprecision will be negligible and she will again be limited only by the zero-point-motion of the mechanics. However, this would be ignoring the Heisenberg-

[1]Sensitivity is quantified by the sum of all sources of measurement imprecision, and is usually described as the measurement variance over the measurement bandwidth. As such, when a contribution of measurement imprecision decreases, the sensitivity decreases as well. This is a favorable effect, since lower sensitivity is finer sensitivity, which is preferable.

mandated backaction of her measurement. Along with the n photons she uses for her measurement come $\sqrt{n}$ shot-noise photons that can randomly kick her oscillator, spoiling the measurement. Clearly, this effect rises with increasing $C_{\rm om}$, as shown by the pink line in Fig. 3.1. Without deviating from coherent mechanical and optical states (an option I will explore further in Chapters 4 and 5), the experimentalist finds that her best recourse is a compromise between shot-noise imprecision and measurement backaction: the SQL. This occurs when each of these effects contributes an additional quarter-phonon of imprecision, meaning that the SQL has the equivalent of twice the zero-point imprecision.

This qualitative description of the SQL holds for both displacement and force detection. While at first it might seem that optimal conditions for these two measurements should be the same, as force measurement relies on detecting the displacement of an oscillator after it has been forced, a more careful derivation will illuminate the differences. In deriving the sensitivity of an optomechanical system to applied forces, we can consider two approaches that eventually yield the same result. The first, more intuitive, approach is to sum up the various noise sources, optical and mechanical, that limit the force sensitivity. The second, more experimentally motivated, approach is to write down the equation for the transduction of an applied force by the optomechanical system – the signal – and that for the noise power spectral density of the same system – the noise. The ratio of these gives the force sensitivity. I will briefly describe each, and note that a longer derivation is available in Schreppler et al. [37].

First we will derive the sensitivity by adding up force noise contributions. This approach follows the reasoning of Clerk et al. [42]. We begin with the sensitivity of the system to displacements of the mechanical oscillator. The spectrum of optomechanical position noise has three contributions.

$$S_{zz,\rm tot}(\omega) = S_{zz}^{\rm th}(\omega) + S_{zz}^{\rm imp}(\omega) + S_{zz}^{\rm BA}(\omega) \tag{3.1}$$

The first term is due to the intrinsic motion of the mechanical oscillator, and has contributions both from native zero-point motion and from any additional thermal phonon occupation. The symmetrized spectrum of oscillator motion is

$$S_{zz}^{\rm th}(\omega) = z_{\rm HO}^2(2\nu_{\rm th}+1)\frac{\Gamma}{(\omega-\omega_m)^2+(\Gamma/2)^2}, \tag{3.2}$$

where $z_{\rm HO} = \sqrt{\hbar/2m\omega_m}$ is the characteristic harmonic oscillator length for an oscillator of mass m and resonance frequency ω_m, with Γ the mechanical decay rate of the oscillator, and $\nu_{\rm th}$ the thermal phonon occupation in addition to the "+1" term that already accounts for the vacuum energy. The second term in Eq. 3.1 is the imprecision of any measurement of oscillator position due to the shot-noise of the measurement tone. Optical shot-noise is white (constant at frequencies away from its large coherent tone), but, as discussed earlier, its imprecision is inversely proportional to $C_{\rm om}$.

$$S_{zz}^{\rm imp}(\omega) = z_{\rm HO}^2\frac{1}{2\Gamma\varepsilon C_{\rm om}} \tag{3.3}$$

We have included here the heterodyne detection efficiency, ε. Remember that the heterodyne efficiency is exactly half the homodyne efficiency, $\varepsilon = \varepsilon_{\rm hom}/2$. Finally, we have the contribution from measurement backaction. The oscillator is susceptible to backaction over the same spectrum for which it exhibits thermal motion. The backaction noise is proportional to the measurement strength, $C_{\rm om}$.

$$S_{zz}^{\rm BA}(\omega) = z_{\rm HO}^2 C_{\rm om} \frac{\Gamma}{(\omega-\omega_m)^2 + (\Gamma/2)^2} \tag{3.4}$$

Thus we have three terms contributing to position sensitivity, one of which decreases with $C_{\rm om}$, one that is constant, and one that rises. They roughly follow the trends of Fig. 3.1.

The force sensitivity is just the total position sensitivity divided by the susceptibility to applied force, $\chi(\omega) = \{m\left[(\omega_m^2 - |\omega|^2) - i\Gamma\omega\right]\}^{-1}$, squared. In the limit of a high Q oscillator (that is, if $\omega_m/\Gamma \gg 1$), this can be simplified to $\chi(\omega) = \{2m\omega_m\left[-(|\omega| - \omega_m) - i\Gamma/2\right]\}^{-1}$, and gives us for force sensitivity:

$$\begin{aligned} S_{FF,\rm tot}(\omega) &= S_{zz,\rm tot}(\omega)/|\chi(\omega)|^2 \\ &= 2\Gamma p_{\rm HO}^2 \left[(2\nu_{\rm th}+1) + \frac{1}{4\varepsilon C_{\rm om}} \frac{(\omega-\omega_m)^2 + (\Gamma/2)^2}{(\Gamma/2)^2} + C_{\rm om}\right]. \end{aligned} \tag{3.5}$$

Now the terms for the force sensitivity are again, in order from first to last, due to thermal and zero-point noise, shot-noise imprecision, and measurement backaction. We can see from Eq. 3.5 and Fig. 3.1 that when $\omega = \omega_m$ the sensitivity has a minimum, occurring at $C_{\rm om} = 1/2\sqrt{\varepsilon}$ in the case of S_{FF}. The sensitivity at this point is the force sensing SQL for the system, $S_{FF}^{SQL} = 4\Gamma p_{\rm HO}^2 \left(1/\sqrt{\varepsilon} + 1\right)$, where $p_{\rm HO}$ is the characteristic harmonic oscillator momentum.

The second line of reasoning that allows us to derive the force measurement sensitivity of our system is that sensitivity is the ratio of noise to signal in a measurement. In the case of forces acting on an optomechanical oscillator, it is then the ratio of the noise spectral density (as measured in the phase quadrature of heterodyne detection) of the measured light,

$$S_{\rm het}^{PM}(\omega) = \frac{\varepsilon C_{\rm om}\Gamma}{z_{\rm HO}^2} \frac{S_{\rm SN}}{2} S_{zz,\rm tot}(\omega), \tag{3.6}$$

to the transduced force. Here, $S_{\rm SN} = P_{\rm LO}\hbar\omega_{\rm LO}$ is the heterodyne shot-noise power, usually dominated by a strong coherent local oscillator tone. In order to calculate the spectral power of the transduced force, we consider the application of an external force $F_{\rm ext} = F_0 \cos\omega_d t$, at driving frequency ω_d, to our oscillator. In the frequency domain, the force has the form $\tilde{F}_{\rm ext}(\omega) = \frac{F_0}{2}\left(\delta_{\omega,\omega_d} + \delta_{\omega,-\omega_d}\right)$. It affects the position of the mechanical oscillator according to the mechanical susceptibility:

$$\hat{z}(\omega) = \chi(\omega)\tilde{F}_{\rm ext}(\omega) \tag{3.7}$$

Now we consider the subsequent transduction of these position fluctuations onto the light that exits the cavity. We use the linear amplifier model for optomechanics of Botter et al. [56] for this treatment. In the case of linear optomechanical coupling and probe light resonant

with the cavity, we expect the entire optical response to be contained within the phase fluctuations of the light,

$$\begin{aligned}\hat{X}^{\mathrm{PM}}(\omega) &= -i(\hat{a}(\omega) - \hat{a}^{\dagger}(\omega)) \\ &= \frac{g_c}{\kappa}\frac{\hat{z}(\omega)}{z_{\mathrm{HO}}},\end{aligned} \tag{3.8}$$

where $g_c = 2g_{\mathrm{om}}\sqrt{\bar{n}} = \sqrt{C_{\mathrm{om}}\kappa\Gamma}$ is the collective optomechanical coupling. Using the boundary conditions of the cavity, $\hat{X}_{\mathrm{out}} = \hat{X}_{\mathrm{in}} + \sqrt{2\kappa}\hat{X}$, we describe the PM quadrature light exiting the cavity,

$$\hat{X}^{\mathrm{PM}}_{\mathrm{out}}(\omega) = \sqrt{2\kappa}\hat{X}^{\mathrm{PM}}(\omega) \tag{3.9}$$

The power in this quadrature as measured by the heterodyne detector (after beating with a local oscillator) is

$$\hat{P}_{\mathrm{PM}} = -i\sqrt{\frac{S_{\mathrm{SN}}\omega^2_{\mathrm{BW}}}{2}}\sqrt{\varepsilon}\langle\hat{a}_{out}(\omega) - \hat{a}^{\dagger}_{out}(-\omega)\rangle, \tag{3.10}$$

where ω_{BW} is the detection bandwidth, and I have omitted additional terms that occur frequencies with only incoherent shot-noise, as these will average out in the next step.. We average the power over a discrete Fourier window, measuring

$$\begin{aligned}\langle\hat{P}^{\mathrm{PM}}\rangle &= \sqrt{\frac{\varepsilon S_{\mathrm{SN}}\omega^2_{\mathrm{BW}}}{2}}\sqrt{\langle\hat{a}_{\mathrm{out}}(\omega)\hat{a}^{\dagger}_{\mathrm{out}}(\omega)\rangle} \\ &= \sqrt{\frac{\varepsilon S_{\mathrm{SN}}}{2}}\langle\hat{X}^{\mathrm{PM}}\rangle \\ &= \sqrt{\frac{\varepsilon S_{\mathrm{SN}} C_{\mathrm{om}}\Gamma F_0^2}{4z^2_{\mathrm{HO}}}}\chi(\omega).\end{aligned} \tag{3.11}$$

Now we normalize the signal we measure by our calibrated force (the method of calibration will be described in the next section), noting that the calibration is an rms force so we need an extra factor of $\sqrt{2}$. This gives us a measured force transduction (with units of W/N):

$$\begin{aligned}T_{\mathrm{sig}} &= \frac{\sqrt{2}\langle\hat{P}^{\mathrm{PM}}\rangle}{F_0} \\ &= \sqrt{\frac{\varepsilon S_{\mathrm{SN}} C_{\mathrm{om}}\Gamma}{2z^2_{\mathrm{HO}}}}\chi(\omega)\end{aligned} \tag{3.12}$$

Finally, we can take the ratio of $S^{\mathrm{PM}}_{\mathrm{het}}(\omega)/|T_{\mathrm{sig}}(\omega)|^2$ and recover Eq. 3.5.

This second derivation is useful to include as it gives intuition for how we extract force sensitivity from our acquired data. I will return to this later in the chapter.

Now that we have derived forms for the position (Eq. 3.1) and force (Eq. 3.5) sensitivity, we can compare their spectra and limits. The SQL is defined for each by the minimum

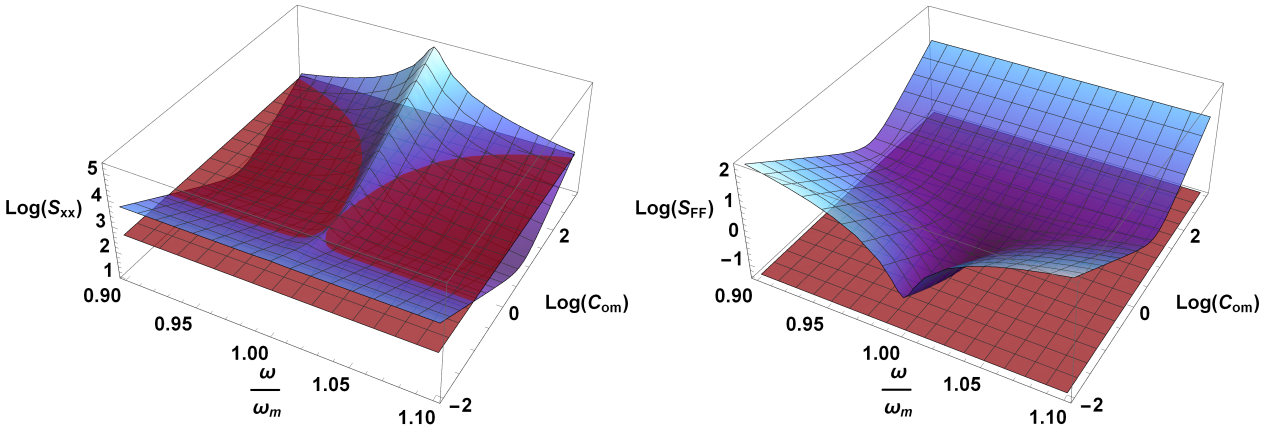

Figure 3.2: Displacement (left) and force (right) sensitivity as a function of frequency and $C_{\rm om}$. The red plane is the SQL for each case, defined as the minimum sensitivity for measurements at $\omega = \omega_m$. Sensitivities are in harmonic oscillator units and the oscillator $Q = 100$.

sensitivity when $\nu_{\rm th} = 0$, $\varepsilon = 1$, and $\omega = \omega_m$, occurring at $C_{\rm om} = 1/2\sqrt{2\varepsilon}$ for position measurements and $C_{\rm om} = 1/2\sqrt{\varepsilon}$ for force measurements. We can additionally see from Eq. 3.5 that the force sensitivity is in fact always minimized whenever $\omega = \omega_m$. This is shown on the right plot in Fig. 3.2, where the sensitivity only touches the SQL-valued plane at a single point in the ω vs $C_{\rm om}$ spectrum. By contrast, Eq. 3.1 (specifically the terms $S_{zz}^{\rm th}$ and $S_{zz}^{\rm ba}$) suggests that sensitivity to displacement can always be improved by measuring at frequencies ω increasingly far from resonance. This is evident on the left plot of Fig. 3.2, where sensitivities can easily beat the SQL over a range of $C_{\rm om}$ for frequencies above and below ω_m. Physically, this can all be understood by the factor of $|\chi(\omega)|^2$ that separates force from position sensitivity. Because the noise in position measurements has a Lorentzian spectral lineshape, meaning that most of it occurs near the resonance frequency, one can always improve one's precision by choosing to measure at frequencies where the noise isn't, namely outside of a region that is approximately $\omega_m \pm \Gamma$. For measuring forces, on the other hand, we have seen that it is not enough to escape the noise, as one must still choose a frequency at which the oscillator can be used to detect a force. As such, the sensitivity has an inverse Lorentzian spectral lineshape, which can only be optimized on resonance. Again, these conditions are true so long as we restrict ourselves to coherent optical and mechanical states. A far more colorful and interesting set of circumstances arises if we relax this restriction, and we will return to this idea in later chapters.

3.3 DC force measurement

With the derivation of force sensitivity behind us, I will now begin to describe the details of our actual experimental force measurement. The first step in characterizing force sensitivity is to calibrate the forces to be applied. As described in Ch. 2, we use an optical

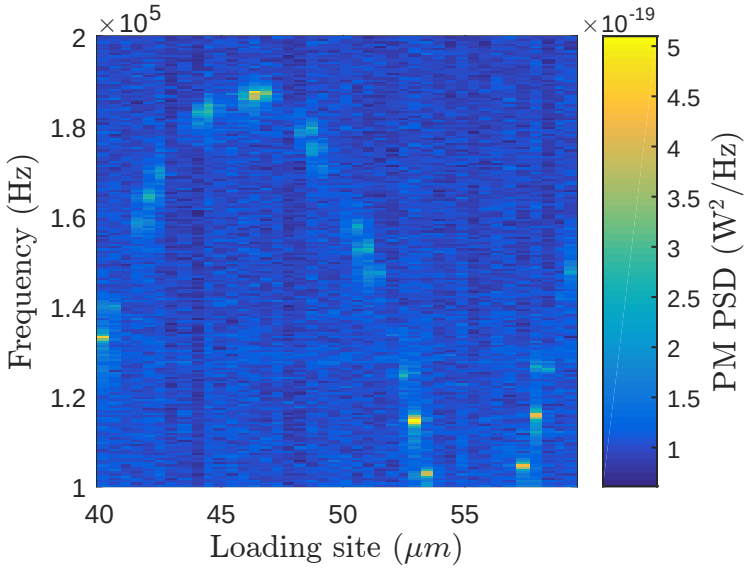

Figure 3.3: Power spectral density of multiple loading sites in an optical superlattice. Both the mechanical frequency change and the optomechanical coupling change (response power, as shown by color) with loading position are apparent.

superlattice to trap our atoms and to apply forces. Since we expect our system to be most sensitive to forces at frequencies near ω_m, we choose to apply a force to our atomic oscillator by modulating the power of one of the components of the superlattice at that frequency. The force applied is therefore given by the dc force of that component of the trap potential modified by some the modulation index at the frequency of interest. We thus needed both pieces of information to go about determining our system's sensitivity.

The superlattice potential that the atoms experience can be easily modeled as the sum of three sinusoidal potentials $U_i = |U_i| \sin^2(k_i z + \phi_i)$. The magnitude $|U_i|$ of each component can be deduced from the observed motional frequency associated with atoms trapped in the minima of either ODT (for $i = \{A, B\}$) or from a measurement of $\bar{n}$, the average number of probe photons in the cavity (for $i = p$), together with knowledge of the CQED coupling rate. For the former, we assume that the trapping potential is approximately harmonic near its minimum, such that $\omega_m = \left(-\frac{1}{m}\frac{\partial^2 U}{\partial z^2}\right)^{1/2}$. This approximation is valid so long as the oscillator is in its ground state, but breaks down with excitation of the oscillator, as will be seen later in this chapter. Knowledge of the strength of each superlattice component in turn allows us to deduce their relative phases ϕ_i by following the work of Botter et al. [36] and spectrally mapping the trap frequency of a range of loading sites along the superlattice, as shown in Fig. 3.3.

To further confirm this model, we use our magnetic trap to load our atoms first into a particular starting location within our superlattice, measuring the static cavity shift that results from their presence. After time, we decrease the power in one of the ODTs, noting that

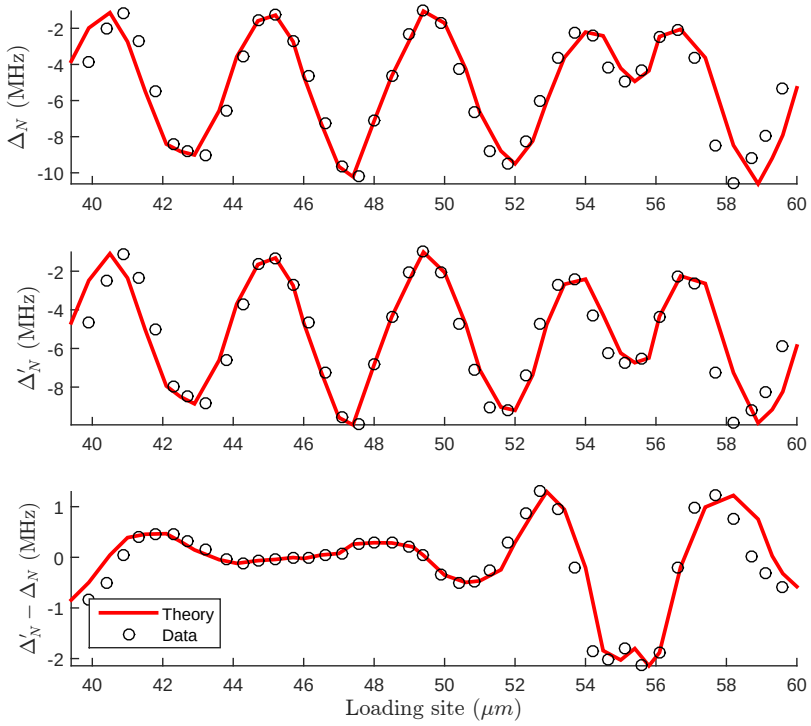

Figure 3.4: Cavity shift (relative to empty cavity resonance) as a function of atomic loading position for initial ODT power (top) and final ODT power (middle) after we forcibly moved the potential minima. The difference in shift (bottom) matches the superlattice potential theory well and confirms our model's accuracy in measuring the static force of the ODTs.

this will produce a different superlattice potential with shifted minima. We again measure the cavity shift due to the atoms, and note that any frequency change is the consequence of the altered potential landscape that the atoms experience. The change in the cavity shift due to the displacement of the atoms (from Δ_N to Δ'_N, is shown in Fig. 3.4). We then repeat this measurement for the same range of loading positions along the cavity axis as in Fig. 3.3. The cavity shift is a direct measurement of the displacement of our atomic oscillator, since the optomechanical coupling relates them by the equation $\Delta_N = N_a g_0^2 \sin^2(k_p z)/\Delta_{ca}$.

Having confirmed our understanding of the potentials, we can then calculate from our model the precise location of the superlattice minima along the cavity axis and find the location of our oscillator of interest. This finally allows us to determine the static force applied by each component of the trapping potential at these minima, $F_i = \frac{\partial U_i}{\partial z}|_{z=z_{\min}}$, as plotted in Fig. 3.5. Here we see why a superlattice potential allows for application of forces by modulating one ODT. When the atoms sit undriven at the trap minimum, the ODT's in the two-color lattice apply equal and opposite forces $F_A = -F_B$ (neglecting the force of gravity and the very small F_p). If ODT-A were removed, returning the atoms to a single-color

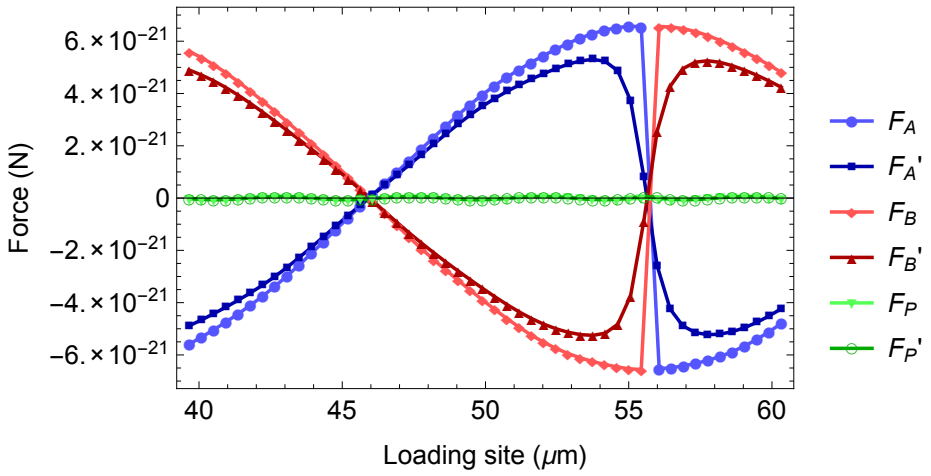

Figure 3.5: Model-derived force from each component of the optical potential (A is ODT-A, B is ODT-B, and p is the probe) for the loading positions considered. Model input parameters are experimentally-calibrated U_i and ϕ_i, $i = \{A, B, p\}$. The components of the force should sum to zero for the trapping condition to hold. Lighter colors indicate forces for conditions before the ODT was stepped and darker colors indicate conditions after the step.

lattice, its force contribution F_A would vanish and the atoms would fall into the minimum of ODT-B, where $F_B = -F_A = 0$. In this case, modulating either ODT would not result in a net force. A two-color lattice is therefore required to achieve $F_A = -F_B \neq 0$. In this case, modulating one ODT does change the net center-of-mass force on the atoms.

3.4 Calibrating applied force

Having determined the dc force, our next step is to measure how it is modified by modulating the intensity of one of the trapping lasers. We observe the transduction of this modulation onto the laser light by recording its fluctuations on a photodiode. In this case, then, a rigorous optical treatment is best for deducing the modulation index. The ODT has some dc power, already determined, to which we apply a very small ac modulation ($m = P_{\mathrm{mod}}/P_L \ll 1$). We represent this as a traveling field with weak sidebands applied.

$$\langle \hat{X}_L(\omega) \rangle = \sqrt{2\pi P_L} \left\{ \delta(\omega - \omega_L) + \sqrt{m/2} \left[\delta(\omega - \omega_L - \omega_{\mathrm{mod}}) + \delta(\omega - \omega_L - \omega_{\mathrm{mod}}) \right] \right\} \quad (3.13)$$

The photodetector measures the mean optical power modulations.

$$\langle \hat{I}(t) \rangle = \sqrt{\epsilon} G \langle \hat{X}_L^\dagger(t) \rangle \langle \hat{X}_L(t) \rangle \quad (3.14)$$

G is the gain of the detector and ϵ is its quantum efficiency. We observe the power spectral density of the photocurrent.

$$\begin{aligned}\frac{S_{II}(\omega)}{\epsilon G^2} =& P_L^2\delta(\omega) + 2P_L\sqrt{2P_L P_{\text{mod}}}(\delta_{\omega,\omega_{\text{mod}}} + \delta_{\omega,-\omega_{\text{mod}}}) \\ &+ 2P_L P_{\text{mod}}(\delta_{\omega,2\omega_{\text{mod}}} + \delta_{\omega,-2\omega_{\text{mod}}}) + \frac{P_L\hbar\omega_L}{2\pi}\end{aligned} \tag{3.15}$$

We analyze only the negative frequency components of the power spectral density (though they are equal to those at positive frequencies since S_{II} is a real signal). Taking the ratio of the squared power of the positive frequency sideband to the squared power of the ODT at dc gives

$$\frac{S_{II}(\omega_{\text{mod}})}{\epsilon G^2} = 2\sqrt{2P_{\text{mod}}/P_L}. \tag{3.16}$$

From this we have our modulation index of interest (squared), which we then multiply by the squared static force applied by the ODT and by the squared number of atoms to give us our overall calibrated applied force.

$$F_0^2 = \frac{1}{2}\frac{S_{II}(\omega_{\text{mod}})}{S_{II}(0)}N_a^2(\text{force per atom})^2 \tag{3.17}$$

This is the force we normalize our coherent response by to get our measured $|T_{sig}|^2$.

3.5 Fitting the data

Having calibrated our applied force, our experimental sequence proceeds as follows. We load atoms into our superlattice potential, then apply a constant modulation to that potential at a single frequency. While this modulated force persists, we introduce probe light at a given C_{om} and resonant with the optical cavity. After its interaction with the atoms, we measure its beating with a local oscillator using our heterodyne receiver. We collect between 1 and 5 ms of data, depending on the strength of the probe light. We repeat this procedure many times to create a statistical ensemble of measurements for each of several values of modulation frequency at and near ω_m and for values of C_{om} that span two orders of magnitude, thus assuring that we will be observe regions of sensitivity that are both shot-noise and backaction dominated. The heterodyne time signal, together with additional calibrations, gives us the phase-sensitive information we need to separate the coherent force signal from the incoherent noise of the measurement. In this section, I will detail the process of determining S_{FF} from our acquired signal.

3.5.1 Separating signal from noise

As described in Ch. 2, heterodyne detection is phase sensitive detection that rotates between in-phase and out-of-phase quadratures at the heterodyne frequency. It is an important

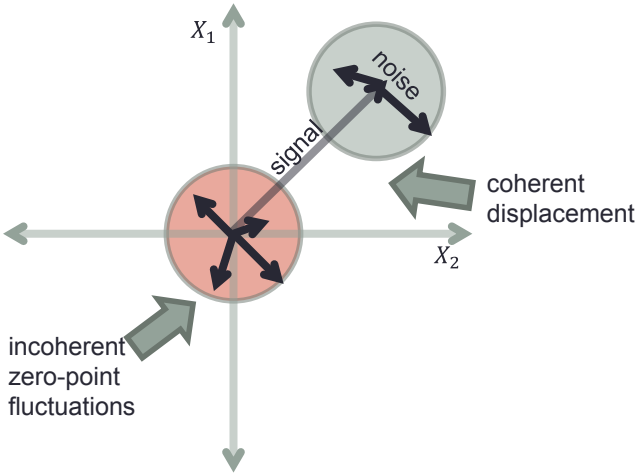

Figure 3.6: Phase space schematic of a vacuum state (red) and a displaced coherent state (blue). The vacuum state is composed of incoherent fluctuations, while the displaced coherent state has large average displacement of constant phase with additional incoherent noise around its mean.

tool, therefore, for separating phase-coherent signals from incoherent ones. To understand the importance of the coherence distinction, it is useful to imagine the signal in phase space, as in Fig. 3.6. The Fourier spectrum of a time series is in general complex, such that every frequency point in the spectrum has a magnitude and phase. The vacuum state has zero magnitude when averaged over a statistical ensemble. However, any single measurement can yield a non-zero magnitude and an associated phase. The black arrows emanating from the origin in Fig. 3.6 are examples of individual measurements of a vacuum state. They could be recovered, for example, by plotting the magnitude and phase of a frequency point in the heterodyne Fourier spectrum that contains only photon shot-noise. If we were to average over very many such measurements, we would find that the vectors we plot fill in a disk in phase space centered at the origin, suggesting that the average vector does in fact have zero magnitude. However, the non-zero radius of the disk represents a non-zero standard-deviation: the incoherent noise power. A displacement of the circle in phase space, like the gray "signal" vector, corresponds to a coherent drive. For example, if we look at the heterodyne beat frequency in the spectrum, we expect to see a large magnitude response with a definite phase. Vacuum fluctuations are still present, but they do not cancel out the average coherent displacement. In this section, I will describe how we separate such coherent signals from incoherent noise in practice. We will return to the phase-space picture later in this chapter when we plot the state of our forced mechanical oscillator.

In the case of our force measurements, so long as the applied force has a constant phase over the ensemble of measurements, the transduced force response, derived in Eq. 3.12, is phase-coherent, with a frequency-dependent phase relative to the drive given by $\chi(\omega)$. Because we have carefully avoided any coherent technical noise in our setup, the measurement noise, on the other hand, should consist only of vacuum-driven fluctuations and some residual

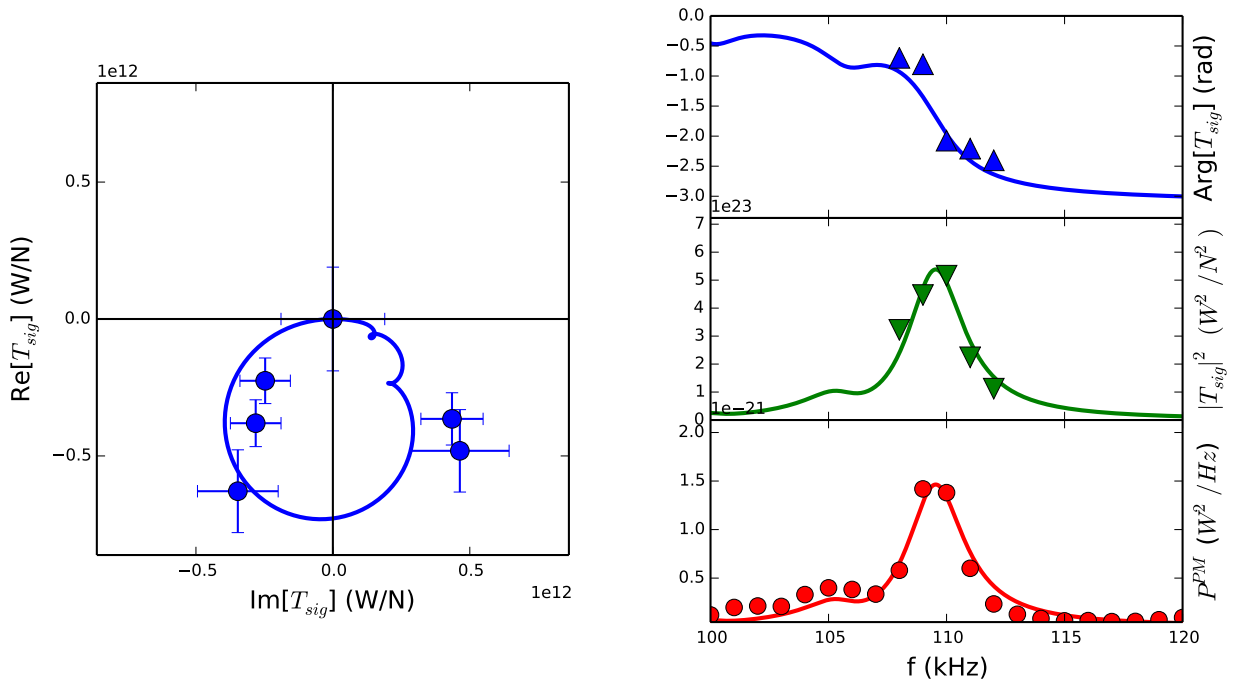

Figure 3.7: Force sensitivity data for $C_{\rm om} = 4$. Left: The complex coherent response to applied force at at 108, 109, 110, 111, and 112 kHz driving frequency, together with a complex fit. Right: Blue and green traces are the phase and amplitude, respectively, of the complex response at left. Red is the incoherent noise spectral density for the same conditions, together with its fit.

thermal noise, all incoherent. Therefore, by averaging together the complex heterodyne signal for many experimental realizations, the incoherent noise should average to zero while the coherent signal should remain.

We can divide this transduced force signal by the power spectral density (which gives the absolute value of the heterodyne signal, and is thus not sensitive to phase angle) of the unforced oscillator to determine force sensitivity. Data for several values of force driving frequency ω_d and fixed $C_{\rm om} = 4$ are shown in Fig. 3.7. The complex coherent response is shown in the blue and green data points, while the incoherent noise response is in red. We simultaneously fit both the complex coherent response and the real incoherent response in order to take advantage of increased statistics for shared parameters. The fits yield the sensitivity at mechanical resonance, as well as $C_{\rm om}$, allowing us to compare the data to theoretical predictions for the SQL.

Incidentally, though this experiment strove to measure the force sensitivity of our system, any time we measured the undriven oscillator to record the noise power, we were also performing a test of displacement sensitivity. As shown in Fig. 3.2, at high enough $C_{\rm om}$ we expect frequencies away from mechanical resonance to give displacement sensitivity beyond the SQL. Figure 3.8 shows the magnitude of the averaged coherent spectral response (red)

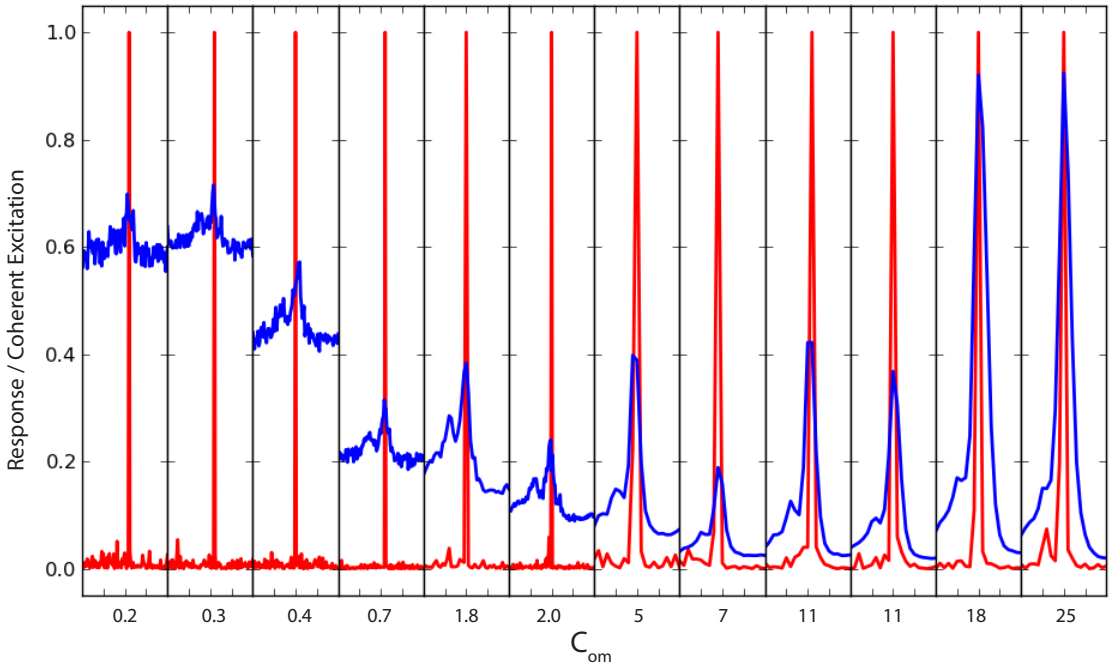

Figure 3.8: Averaged coherent response to resonant force drive (red) and incoherent noise response (blue) for a range of C_{om}. For each C_{om}, both traces are normalized to the peak coherent response. Qualitatively, the peak of the blue curve shows the force sensitivity, while its value away from the peak is proportional to the displacement sensitivity.

plotted with the incoherent noise spectrum across the measured range of C_{om}. For each value of C_{om}, both data sets are normalized to the peak coherent value (red trace maximum). The peaks of the blue data traces therefore are proportional to the force sensitivity, though they lack some corrections for varying experimental parameters for different values of C_{om}. Interestingly, if we look at the noise levels in the blue traces away from their peaks, we see that the values continue to drop as C_{om} increases, even after the peaks begin their backaction-driven upswing. This is exactly due to the continued improvement in displacement sensitivity for increasing measurement strength, as long as we consider frequencies away from ω_m.

3.5.2 Anharmonic trap

In our first attempts at force sensitivity measurements, we had difficulty probing our driven atomic oscillator with high C_{om}. As we increased the probe power, the mechanical response seemed to saturate and broaden. Its broadening was asymmetric, and upon closer inspection showed second and even third peaks arising at frequencies below the resonant response, as observed in Fig. 3.9. These spectral bumps were in fact vibrations in higher bands of the anharmonic oscillator potential. Recall that the standing wave ODT potential is defined by the intensity landscape of the light, and therefore actually has the form of

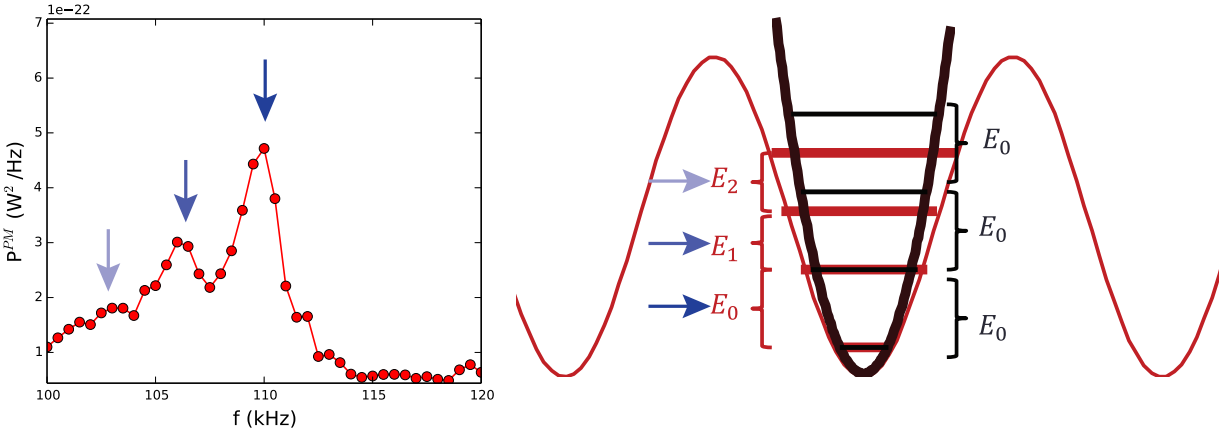

Figure 3.9: Left: Power spectral density of undriven oscillator at $C_{\text{om}} \approx 2$. A second peak is clearly visible at lower frequency and a third peak is somewhat suppressed. Right: Energy level spacing of sinusoidal vs quadratic potential. The quadratic potential shows evenly spaced levels corresponding to harmonic oscillator eigenvalues. The squared sine potential is more relaxed at higher energy, leading to decreasing level spacing as excitation rises.

$\sin^2(z)$ rather than its approximation z^2. In order to calibrate the mechanical oscillator parameters and also to achieve good fits to the data, we needed to predict both the higher band frequencies and the coupling of these bands to the probe light. This would allow us to deduce the population of atoms in each band, since only those in the lowest band contributed to the coherent response to a force applied at that band's frequency.

First, we calculate the frequency spacing of the levels of a one-dimensional optical lattice potential, $V(z) = V_0 \sin^2(k_T z)$, where k_T is the trap wavenumber. Assuming that our atoms are very cold, we expand around small displacements z from the potential minimum:

$$V(z) \approx V_0 \left(k_T^2 z^2 - \frac{1}{3} k_t^4 z^4 \right). \tag{3.18}$$

The first (quadratic) term is just the harmonic oscillator potential, which justifies our usual approximation of atomic motion as harmonic. The frequency of motion in the quadratic potential is then given by $\omega_m = \frac{2}{\hbar}\sqrt{V_0 E_R}$, where $E_R = \hbar^2 k_T^2 / 2m$ is the single photon recoil frequency for the trapping light. In such a harmonic potential, spacing between energy levels is constant and proportional to ω_m, as shown by the black lines in the schematic in Fig. 3.9. Since a sinusoidal potential is more relaxed away from the minimum compared to a quadratic potential, we expect that higher energy levels have increasingly smaller spacing. We will therefore treat the second (quartic) term in the potential expansion as a perturbation on the harmonic oscillator solution states $|n\rangle$. We express the perturbation in terms of the quantum operator $\hat{z}$, where $z = z_{\text{HO}}\hat{z} = z_{\text{HO}}\left(\hat{b} + \hat{b}^\dagger\right)$, z_{HO} is the harmonic oscillator length

associated with state $|n\rangle$, and $\hat{b}$ is the lowering operator for that state.

$$\begin{aligned} E_n^{(1)} &= -\frac{V_0}{3}(k_T z_{\mathrm{HO}})^4 \langle n|\hat{z}^4|n\rangle \\ &= -\frac{V_0}{3}(k_T z_{\mathrm{HO}})^4 \langle n| \left(\hat{b}+\hat{b}^\dagger\right)^2 \left(\hat{b}+\hat{b}^\dagger\right)^2 |n\rangle \\ &= -\frac{E_R}{4}(2n^2+2n+1) \end{aligned} \tag{3.19}$$

We are interested in the energy difference between the nth and $(n-1)$th state of the anharmonic oscillator, to this quartic order in $\hat{z}$.

$$\begin{aligned} E_n - E_{n-1} &= E_n^{(0)} + E_n^{(1)} - E_{n-1}^{(1)} - E_{n-1}^{(1)} \\ &= \hbar\omega_m - nE_R \end{aligned} \tag{3.20}$$

We find that each energy level splitting decreases by an additional recoil frequency. For the harmonic oscillator shown in fig. 3.9, this amounts to a difference of a couple of kilohertz for each level, enough to resolve spectrally the different peaks.

Now let's return to the optomechanical Hamiltonian for the entire atomic oscillator:

$$H_{\mathrm{OM}} = \hbar \sum_{i=1}^{N_a} \left(\frac{g_0^2 \sin^2(k_p z_i)}{\Delta_{ca}} \right) (\hat{a}^\dagger \hat{a}). \tag{3.21}$$

Let's consider the Hamiltonian for just one atom of this oscillator, at the point of linear coupling to the probe light.

$$\begin{aligned} H_{\mathrm{OM},i} &= \frac{\hbar g_0^2}{\Delta_{ca}} (\hat{a}^\dagger \hat{a}) \sin^2(k_p z_i) \\ &\approx \frac{\hbar g_0^2}{\Delta_{ca}} (\hat{a}^\dagger \hat{a}) k_p z_i \end{aligned} \tag{3.22}$$

We are interested in the coupling between harmonic oscillator states $|n\rangle$ and $|n'\rangle$ for a single atom by this optomechanical Hamiltonian. Note that even though we just showed that the oscillator is anharmonic, we will approximate the wave functions as harmonic oscillator solutions.

$$\begin{aligned} \langle n'|H_{\mathrm{om},i}|n\rangle &= \frac{\hbar g_0^2 k_p}{\Delta_{ca}} (\hat{a}^\dagger \hat{a}) \langle n'|z_i|n\rangle \\ &= \frac{\hbar g_0^2 k_p}{\Delta_{ca}} (\hat{a}^\dagger \hat{a}) z_{HO} \langle n'|\hat{b}+\hat{b}^\dagger|n\rangle \end{aligned} \tag{3.23}$$

We see that the matrix element of interest gives us the scaling of the coupling with harmonic oscillator level.

$$\langle n'|\hat{b}+\hat{b}^\dagger|n\rangle = \sqrt{n}\delta_{n',n-1} + \sqrt{n+1}\delta_{n',n+1} \tag{3.24}$$

Therefore, at the point of linear coupling of the probe to the atom's position, we expect that displacement of an atom on the nth excited transition couples $\sqrt{n+1}$ times more strongly than displacement of an atoms in the next lower transition.

3.5.3 Discrepancies in C_{om}

The final piece necessary for comparing our sensitivity measurements to theory is an accurate accounting of optomechanical cooperativity. In the past [35], we inferred C_{om} from a combination of calibration values and fit parameters:

$$C_{\mathrm{om}} = \frac{g_c^2}{\kappa\Gamma} = \frac{4\bar{n}g_{\mathrm{om}}^2}{\kappa\Gamma}. \tag{3.25}$$

The value for $\bar{n}$ comes from a ratio of the heterodyne carrier height to the shot-noise floor, taking into account the measured detection efficiency. Over the years, we have measured κ and found that it has not changed. Γ, the full width at half maximum of the mechanical response, is measured from the data fits. Finally,

$$g_{\mathrm{om}} = \frac{g_0^2}{\Delta_{ca}} k_p \sqrt{\frac{\hbar N_a}{2m_{\mathrm{Rb}}\omega_m}} \tag{3.26}$$

gives the optomechanical coupling, where $g_0 = \sqrt{\frac{d^2\omega_a}{2\hbar\epsilon_0 V_m}}$, with V_m the mode volume of the cavity and ω_a the atomic transition frequency. The value for k_p comes from our high precision wavemeter, Δ_{ca} and ω_a from knowledge of rubidium D2 lines, V_m from calculations and measurements when the cavity was installed, and ω_m from our fits. N_a is measured using the cavity shift Δ_N, with corrections for anharmonicity as described in the last section. d is the dipole moment assuming we have perfect σ_+ polarized light within our cavity. Because the value for d comes into the calculation of N_a by way of g_0, in the end C_{om} is quadratically dependent on g_0 and therefore quadratically on d as well.

In the reporting of our sensitivity measurements, we instead measured C_{om} using the height of the undriven incoherent response to probe shot-noise. As described earlier, the incoherent response peak (that is, on resonance) is expected to take the form:

$$S_{\mathrm{het}}^{\mathrm{PM}} = \frac{S_{\mathrm{SN}}}{2}[1 + 4\epsilon C_{\mathrm{om}}(2\nu_{\mathrm{th}} + C_{\mathrm{om}} + 1)]. \tag{3.27}$$

Solving this equation for C_{om} allows us to determine its value based on the peak height of the incoherent response normalized by shot-noise:

$$C_{\mathrm{om}} = -(\nu_{\mathrm{th}} + 1/2) + \sqrt{(\nu_{\mathrm{th}} + 1/2)^2 - \frac{2S_{\mathrm{het}}^{\mathrm{PM}}/S_{\mathrm{SN}} - 1}{4\epsilon}}. \tag{3.28}$$

The value of ν_{th} was determined using time-of-flight measurements for a particular experimental cycle, while the value of S_{SN} is the noise floor as measured on the un-demodulated heterodyne spectrum in a spectral window without mechanical response. Why the alternative determination of C_{om}? In comparing the results of the two methods, we found that the cooperativity as predicted by the photon number was consistently above that shown by the optomechanical interaction, as plotted in Fig. 3.10.

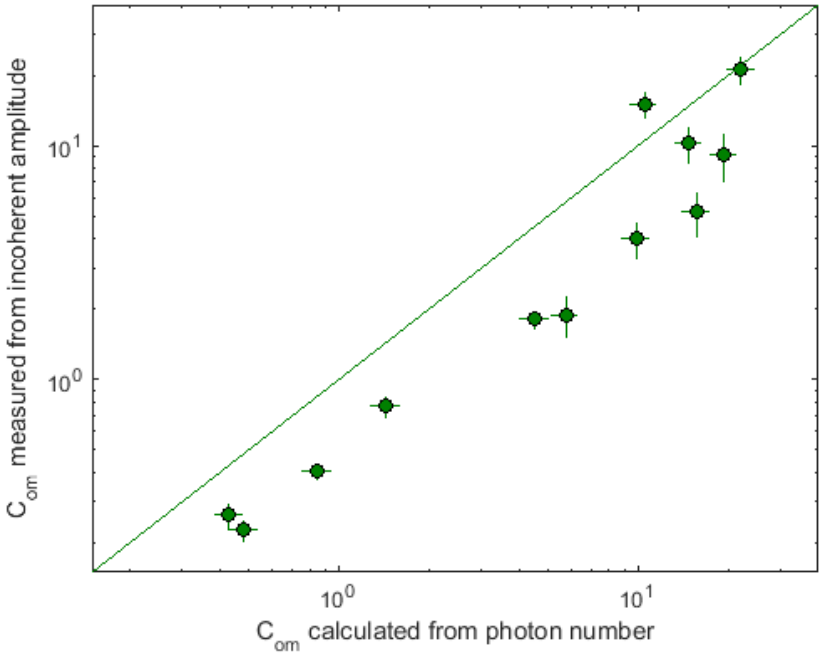

Figure 3.10: Comparison of C_{om} value as measured by strength of optomechanical interaction (ordinate) and C_{om} value as determined from measured photon number (abscissa). An overall offset suggests a calibration error in g_{om}.

$\bar{n}$ **calculation**	$S_{\mathbf{het}}^{\mathbf{PM}}$ **calculation**	**10% correction to** σ_+
g_0	0.88 g_0 (inferred)	0.92 g_0
C_{om}	0.6 C_{om} (observed)	0.72 C_{om}

Table 3.1: Discrepancies in observed coupling g_0 and cooperativity C_{om} as calculated using $\bar{n}$ and $S_{\mathrm{het}}^{\mathrm{PM}}$, compared to the predicted correction needed for a 10% correction to probe polarization purity.

We ultimately decided that since the optomechanical response would provide our sensitivity measurement, it was more consistent to rely on the C_{om} value obtained from the same data. We may speculate here, though, as to what could have lead to this discrepancy.

One possible contributing factor could be the polarization of the probe light. In Ch. 1, we saw that the CQED coupling rate g_0 actually depended on the dot product between the atomic dipole operator and the electric field of the cavity mode. Thus, we expect the coupling to change with the polarization of the light. Since we have seen that C_{om} is actually quartic in g_0, a 15% reduction in g_0 could lead to 50% difference in C_{om}. In more recent experiments, when we have deliberately changed the polarization of the probe light in order to address atoms polarized in different directions, we had cause to examine the purity of σ_+ polarization we had been applying. We found that a quarter wave plate (QWP) at the input to the cavity was 16° off from ideally transmitting σ_+ light, and that the subsequent output QWP was 14° off. For the input QWP, at least, this resulted in approximately 10% of the incident power actually polarized σ_-. This alone might not explain the difference in C_{om}, since the σ_- light would be detuned far from the σ_+ light due to coupled cavity-atomic birefringence. However, since the measurement of detection efficiency was performed using an empty cavity, if the output QWP was incorrectly adjusted along with the input QWP in such a way as to direct some σ_- light onto the detector, we would incorrectly assume more photons were interacting with our atoms during experimental measurements than was accurate. To put this another way, since g_0 is proportional to the dot product of the atomic electric dipole moment and the local electric field of the cavity mode (that is, the dipole matrix element), light that is only 90% σ_+ and 10% σ_- could result in a reduction of g_0 by 8%, compared to perfect σ_+ polarization, as calculated using the respective dipole matrix elements for the rubidium electric dipole transition. The potential contribution of the polarization impurity is compared with the observed discrepancy in Table 3.1. Such a miscalibration could explain some of the difference observed in Fig. 3.10, and bolster our claim (*a posteriori*) that measuring C_{om} using the optomechanical response is the more appropriate method.

3.6 Plotting in phase space

Let's return to the phase-space picture discussed earlier in the chapter. I described the plotting of incoherent and coherent excitations of light. These are exactly what we measure using our heterodyne signal. We also know that the optomechanical coupling means that at

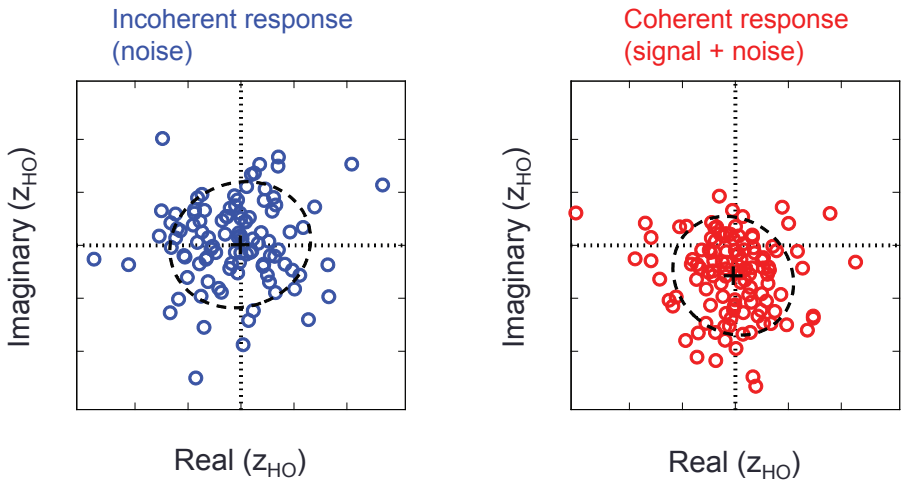

Figure 3.11: Phase space plot of mechanical response as derived from optical heterodyne signal. Left: undriven oscillator shows incoherent scatter around zero-mean displacement, consistent with a near-ground state harmonic oscillator. Right: driven oscillator shows average displacement from the origin at angle $\phi = -\pi/2$, consistent with a resonant driving condition.

certain frequencies, the outgoing state of the light is related to the state of the mechanical oscillator. We can use our knowledge of the optomechanical coupling parameters, therefore, to plot the mechanical oscillator excitations in phase-space. An example of such a plot is shown in Fig. 3.11. Phase-space plotting gives added intuition for what the SQL means in practice, as is discussed in Schreppler et al. [37].

Because of its usefulness, I will derive here the mapping of a complex optical heterodyne signal to the mechanical oscillator state. As described in Ch. 2, our typical analysis takes time-series of voltages from the heterodyne receiver and converts them into Watts, given understanding of detection gains, efficiencies, and bandwidths. It then demodulates at the 10 MHz heterodyne frequency, leaving two quadratures – AM and PM – of data, in Watts. Next it takes a discrete Fourier transform of these quadratures, giving a complex spectrum for each. Depending on the experiment, we would like to investigate and plot points on this complex spectrum, at, near, and far from the mechanical resonance frequency.

We expect the relation between the heterodyne power in the PM quadrature and the normalized displacement of the oscillator to be given by the equation:

$$P_{\mathrm{PM}}(f) = \frac{hf_0}{2} \frac{4\pi\kappa g_C^2(\kappa^2 + f^2)}{(\kappa^2 + \Delta^2 - f^2)^2 + 4\kappa^2 f^2} f_{\mathrm{BW}}^2 \left\langle \left| \frac{z f_{\mathrm{BW}}}{z_{\mathrm{HO}}} \right|^2 \right\rangle . \tag{3.29}$$

On mechanical resonance, and with the limits of our system (unresolved sideband, for example) as simplifying assumptions, Eq. 3.29 reduces to:

$$P_{\mathrm{PM}}(f_m) = \frac{hf_0}{2} \frac{4\pi g_C^2}{\kappa} \left\langle \left| \frac{z}{z_{\mathrm{HO}}} \right|^2 \right\rangle . \tag{3.30}$$

Now for heterodyne detection, given imperfect detection efficiency, we expect to measure:

$$P_{\mathrm{PM}}^{\mathrm{het}}(f_m) = \sqrt{\varepsilon P_{\mathrm{LO}} P_{\mathrm{PM}}(f_m)} = \sqrt{\varepsilon P_{\mathrm{LO}} \frac{h f_0}{2} \frac{4\pi g_C^2}{\kappa} \left\langle \left| \frac{z}{z_{\mathrm{HO}}} \right|^2 \right\rangle}. \tag{3.31}$$

So we can convert measured power in Watts to measured displacement in meters by inverting this equation and taking note of the relations $S_{SN} = P_{\mathrm{LO}} h f_0/2$ and $g_C^2 = 4\bar{n} g_{\mathrm{om}}^2$:

$$P_{\mathrm{PM}}^{\mathrm{het}}(f_m) \sqrt{\frac{\kappa}{\varepsilon S_{\mathrm{SN}} 16\pi \bar{n} g_{\mathrm{om}}^2}} \approx \frac{z}{z_{\mathrm{HO}}}. \tag{3.32}$$

Now we would like to find the statistical variance in the distribution of measurement points. In order to do so, we calculate the 2×2 covariance matrix between the real and imaginary components (the two axes of the phase-plots in Fig. 3.11) of the data. We plot the associated error ellipse with 68.3 % confidence interval. The eigenvalues of this matrix are the minor and major axis lengths, and they give us a measure of the incoherent noise.

For quadrature operators of a harmonic oscillator X_1 and X_2, where $z(t) = X_1(t)\cos(\omega_m t) + X_2(t)\sin(\omega_m t)$, the commutation relation is $[X_1, X_2] = 2i z_{\mathrm{HO}}^2$. According to Clerk et al. [42], this commutation relation shows that a weak measurement of two quadratures will have a total uncertainty that is twice the zero-point motion of the oscillator. The commutation relation is derived using the fact that X_1 and X_2 are quadrature operators of the harmonic oscillator with Hamiltonian $H = \hbar\Omega(b^\dagger b + 1/2)$, such that $X_1 = b + b^\dagger$ and $X_2 = i(b - b^\dagger)$ and $[b, b^\dagger] = 1$. Using the commutator, we can calculate an uncertainty relation of $\Delta X_1 \Delta X_2 \geq |\frac{1}{2i}\langle [X_1, X_2]\rangle| = 1$. This uncertainty relation includes uncertainty from the oscillator zero-point motion itself (1/2) and uncertainty from the measurement (1/2).

Clerk et al. [42] point out that this inequality is minimized when the measurement is performed over the course of one mechanical damping time and with perfect detection efficiency – the SQL. After each mechanical damping period, the imprecision in phase space area decreases. We can infer that imperfect detection efficiency would serve to increase the expected phase space area (and equivalently the expected uncertainty relation product), since for every photon that is counted at our detector there are $\epsilon^{-1} - 1$ photons that have introduced measurement uncertainty but have not been counted. Therefore, we might expect the measured phase space area (that is, the product of the semi-major and semi-minor axes of the error ellipse) to be of size $1/\epsilon\tau\Gamma$ where τ is the time over which we measure the oscillator.

We will revisit the phase-space representation, particularly in Ch. 5, when we consider how quantum squeezing manifests in phase-space.

Chapter 4

Ponderomotive Squeezing

To see thus
Is to ignore the revenge of light on shadow,
To confound both in a brittle and false union.

Charles Tomlinson, "Through Binoculars", 1955

4.1 Introduction

As described in Ch. 1, optomechanical coupling is an interaction between light and mechanical motion. The results of our force sensitivity measurements showed how this interaction could lead to a tradeoff between the sensitive measurement of mechanical fluctuations, thanks to their coupling to the probe light, and the disturbance of those same fluctuations by the backaction of the light itself. In this chapter, I will discuss another phenomenon that results from this delicate interplay: ponderomotive squeezing.

From the start, investigations of light squeezing were motivated by the sensitivity of interferometric measurements. In particular, Caves [57], Braginsky et al. [6], and later members of the LIGO collaboration [58] proposed using squeezed light to improve the sensitivity of the minute displacement measurements performed in gravitational wave detectors. The proposals identify quadrature squeezed light[1] as a means of reducing the measurement imprecision associated with optical noise. While a coherent light state, shown in blue in Fig. 4.1, has equal uncertainty in both its amplitude and phase, a quadrature-squeezed state has reduced uncertainty in one of its quadratures. This "squeezing" of optical noise necessarily comes at the expense of "anti-squeezing" in the conjugate quadrature. Light that is amplitude-squeezed will have more uncertainty in its phase and vice versa. Quadrature squeezing is not limited to amplitude or phase, but can be created (through judicious experimental setup) at any angle ϕ, with $\phi = 0$ defining AM and $\phi = \pi/2$ PM, as discussed in Ch. 2. This could be

[1] Though the focus in this chapter is limited to quadrature squeezing, Ch. 5 will mention some other kinds of squeezing on the way to a more generalized form of ponderomotive squeezing.

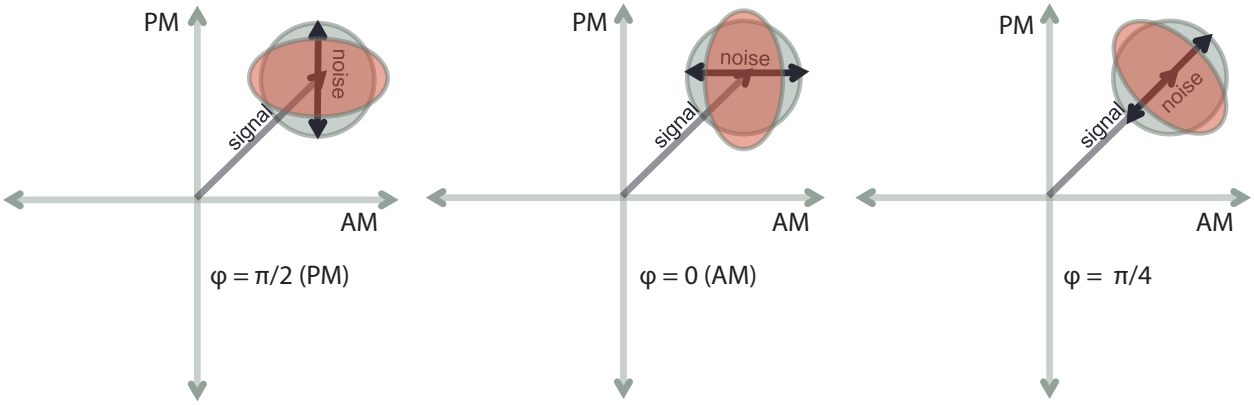

Figure 4.1: Quadrature squeezed states (red ovals) have reduced uncertainty in one quadrature at the expense of increased uncertainty in the conjugate quadrature, compared to equal-uncertainty coherent states (blue circles). From left to right are phase-squeezed, amplitude-squeezed, and $\pi/4$-squeezed states. The right plot shows a state with squeezing chosen to improve sensitivity to the coherent displacement of the light along the $\pi/4$ axis.

convenient, as shown in Fig. 4.1, if that ϕ corresponds with the angle of interest for a sensitive measurement. Reduced incoherent fluctuations along the coherent displacement axis would result in improved sensitivity. Quadrature squeezing of light was first observed experimentally using the method of four-wave-mixing through the interaction between coherent light and sodium atoms [59].

Simultaneously with investigations of squeezed light, came a theoretical push to understand the implications of radiation pressure in optical interferometric measurements. The damping effect of radiation pressure in an optomechanical system was proposed by Braginsky and Manukin [60], when the term "ponderomotive" was introduced to describe the "friction of light" encountered by the mirrors of a Fabry-Pérot resonator. Debate on the matter of whether or not this radiation-pressure-driven damping could impact the interference measurement was ultimately put to rest by Caves [61] with an abstract reading simply:

> *The interferometers now being developed to detect gravitational waves work by measuring small changes in the positions of free masses. There has been a controversy whether quantum-mechanical radiation-pressure fluctuations disturb this measurement. This Letter resolves the controversy: They do.*

Further investigation of the effects of radiation pressure led to a surprising result: the additional measurement noise it introduces is correlated with the measured optical shot-noise through the optomechanical interaction [60, 62]. This correlation can lead to frequency-dependent gain or attenuation of the optical noise in certain quadratures. This is to say that optomechanics can actually produce its own squeezed light [63, 64], through the phenomenon of ponderomotive squeezing.

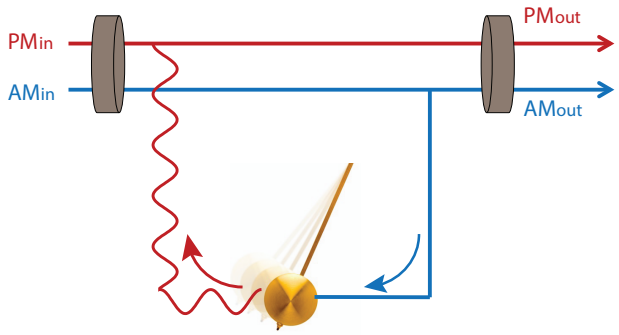

Figure 4.2: Amplifier-style schematic of the optomechanical interaction. When Δ_{pc}=0 (i.e. the cavity is driven at its resonant frequency, as shown here), input AM fluctuations drive the oscillator motion, which then imprints onto intra-cavity PM fluctuations. Upon exiting the cavity, the output AM and PM fluctuations are now correlated. If $\Delta_{pc} \neq 0$, variation in cavity frequency ω_c induced by oscillator motion adds modulation onto both AM and PM output fluctuations.

Nearly two decades after its prediction, this effect was observed in three distinct optomechanical systems [26–28]. In this chapter I will not detail the full extent of our experimental efforts in Brooks et al. [26], but rather strive to give intuition for the origins of ponderomotive squeezing. I will show some unpublished squeezing spectra that additionally confirm our model of squeezing under varied conditions, and will additionally endeavor to address the lingering question of whether, after all, this squeezing can be used to improve upon interferometric displacement and force measurements.

4.2 Predicted spectra

First, I will expand upon the intuition for the origin of ponderomotive squeezing. I will follow this with a quantitative derivation of the predicted squeezing spectrum in certain limits, noting that a full and rigorous treatment of the quantum optics of ponderomotive squeezing is given in Refs. [56] and [26], as well as in Thierry Botter's thesis.

In an optomechanical system, the radiation pressure fluctuations of the probe light drive mechanical motion of the oscillator. These random momentum kicks come from the amplitude fluctuations of the light (present even in the vacuum). If we were to measure the light with a homodyne or heterodyne detector, we would observe these amplitude fluctuations, by definition, in the AM quadrature. For a coherent state of light, they are completely uncorrelated from the phase fluctuations observed in the PM quadrature (recall the round shape of the coherent states shown in Fig. 4.1, showing no correlation trend). However, when the probe light is resonant with the cavity, the mechanical motion of the oscillator imprints onto the phase fluctuations of the light, as shown in Fig. 4.2. (For simplicity, in this chapter I will focus on the case where the detuning of the probe light from cavity resonance is $\Delta_{pc} = 0$, though I will qualitatively describe the effects of probe detuning later.) Thus the phase

fluctuations of the exiting light carry with them information about the mechanical oscillator motion, some of which is governed by the amplitude fluctuations of the light. While the noise level of the outgoing AM quadrature is not affected by the optomechanical interaction, one can imagine that by choosing the homodyne phase, one could measure a quadrature angle ϕ that combines AM and PM (say $\phi = \pi/4$). In this case, the correlated noise between AM and PM could interfere, either constructively or destructively. If the destructive interference is sufficient to bring the noise in that quadrature below its vacuum value, the light is quadrature squeezed.

A more careful derivation of the expected outgoing optical spectra at different quadratures will help to suggest the parameters under which ponderomotive squeezing might be observed experimentally. Our predictions for the spectra of ponderomotive squeezing (and additionally for the force sensitivity derived in Ch. 3) come from the linear amplifier model of optomechanics we detail in Botter et al. [56]. In that work, we connected the input fields of our optomechanical system, both optical and mechanical, to optical outputs, via linear transduction matrices. In doing so, we treated the optomechanical system as a quadrature-sensitive linear amplifier for optical fluctuations. This is a particularly useful scheme for illuminating the origins of ponderomotive squeezing, since these input and output fields can easily be divided into separate quadratures which have different physical interaction with the mechanical oscillator, as illustrated in Fig. 4.2. The resulting correlations between outgoing AM and PM quadratures are responsible for the predicted ponderomotive squeezing.

We will generalize the PM quadrature optomechanical spectrum of Ch. 3 to a spectrum at quadrature angle ϕ. This angle can be chosen, in homodyne detection, by a constant phase-offset of the LO light relative to the signal. In heterodyne detection, as described in Ch. 2, ϕ rotates at the relative heterodyne frequency, such that all quadrature angles are available and can be selected by the appropriate demodulation process. Since we must allow for cross-terms in the power spectral density, we begin our derivation with the Fourier transform for one quadrature of the light that exits the cavity. It is a linear combination of AM and PM quadratures at the output.

$$\hat{X}\left(\phi,\omega\right) = \hat{X}_{\mathrm{AM}}(\omega)\cos(\phi) + \hat{X}_{\mathrm{PM}}(\omega)\sin(\phi) \tag{4.1}$$

Utilizing the Wiener-Khintchine theorem (see Mandel and Wolf [65] for an expansive treatment of the subject), the power spectral density is then the autocorrelation function of the above equation, here shown in frequency space.

$$\begin{aligned} S(\phi,\omega) &= \langle X\left(\phi,\omega\right) X\left(\phi,-\omega\right)\rangle \\ &= \cos^2(\phi)\langle X_{\mathrm{AM}}(\omega)X_{\mathrm{AM}}(-\omega)\rangle + \sin^2(\phi)\langle X_{\mathrm{PM}}(\omega)X_{\mathrm{PM}}(-\omega)\rangle \\ &+ \cos(\phi)\sin(\phi)\langle X_{\mathrm{AM}}(\omega)X_{\mathrm{PM}}(-\omega) + X_{\mathrm{PM}}(\omega)X_{\mathrm{AM}}(-\omega)\rangle \end{aligned} \tag{4.2}$$

Next we must take an accounting of the sources of power in each optical quadrature. Here we will mirror the steps of Ch. 3, when we tallied up the noise contributions for measuring the position of the mechanical oscillator. The outgoing PM quadrature has noise contributions from the thermal fluctuations of the oscillator, from shot-noise imprecision,

and from the backaction driven motion of the oscillator. The first of these is related to the input mechanical field, which we treat as a thermal bath for the mechanical oscillator with input $\hat{X}^{\rm in}_{\rm mech}$[2]. The second is simply due to the phase-fluctuations of the input light, $\hat{X}^{\rm in}_{\rm PM}$. Finally, the third is due to the amplitude-fluctuations of the input light $\hat{X}^{\rm in}_{\rm AM}$, and shows up in the PM quadrature as transduced by the mechanics.

$$\begin{aligned} X_{\rm PM}(\omega) &= X^{\rm th}_{\rm PM}(\omega) + X^{\rm imp}_{\rm PM}(\omega) + X^{\rm BA}_{\rm PM}(\omega) \\ &= \frac{1}{2}\sqrt{S_{\rm SN}}\Bigg[\left(2m\omega_m\Gamma\chi(\omega)\sqrt{(\nu_{\rm th}+1)\varepsilon C_{\rm om}}\right)\hat{X}^{\rm in}_{\rm mech}(\omega) \\ &+ \hat{X}^{\rm in}_{\rm PM}(\omega) \\ &+ \left(2m\omega_m\Gamma\chi(\omega)\sqrt{\varepsilon C^2_{\rm om}}\right)\hat{X}^{\rm in}_{\rm AM}(\omega)\Bigg] \end{aligned} \tag{4.3}$$

All three terms carry with them a factor of $\sqrt{S_{\rm SN}}$, with $S_{\rm SN}$ the shot-noise power density, dominated by the LO power used in detection of $X_{\rm PM}$. Two assumptions made in Eq. 4.3 are that the mechanical oscillator has a high quality factor ($Q = \omega_m/\Gamma \gg 1$) and that the system is in the unresolved sideband regime ($\omega_m/\kappa \ll 1$). Operation in the unresolved sideband regime is an important requirement for the observation of ponderomotive squeezing. The PM fluctuations produced by mechanical motion are delayed by one oscillator cycle from the AM fluctuations that kicked the oscillator to begin the process. Therefore, the correlations have an inherent time delay set by the mechanical frequency. A cavity that equilibrates faster than mechanical motion (that is, one for which $\kappa \gg \omega_m$) has bandwidth large enough to allow the correlations to develop. An interesting finding of Ref. [56] was that in the resolved sideband regime, these same correlations can lead to the phenomenon of optomechanically induced transparency (OMIT).

Though the input AM fluctuations drive the mechanical oscillator, the output AM quadrature should carry only a record of the input fluctuations.

$$\begin{aligned} X_{\rm AM}(\omega) &= X^{\rm imp}_{\rm AM}(\omega) \\ &= \frac{1}{2}\sqrt{S_{\rm SN}}\hat{X}^{\rm in}_{\rm AM}(\omega) \end{aligned} \tag{4.4}$$

Already we can see that both $X_{\rm AM}$ and $X_{\rm PM}$ carry information about $\hat{X}^{\rm in}_{\rm AM}$. Returning to

[2]Note that this contribution contains a $(\nu+1)$ term which is only correct for negative ω. Due to the quantum nature of the mechanical oscillator, for positive ω the extra +1 disappears, leading to an asymmetry in the predicted spectrum between positive and negative frequencies (observable in our system, as shown in Brahms et al. [35]). We will symmetrize the PSDs in this chapter (that is, arithmetically average positive and negative spectral densities) to account for this asymmetry.

the PSD, we find:

$$S(\phi,\omega) \approx \frac{S_{\mathrm{SN}}}{2}\Bigg\{\cos^2(\phi)\frac{1}{2} + \sin^2(\phi)\left[\frac{m^2\omega_m^2\Gamma^2}{2}\left|\chi(\omega)\right|^2\left(\nu_{\mathrm{th}}+\frac{1}{2}\right)\varepsilon C_{\mathrm{om}} + \frac{1}{2} + \frac{m^2\omega_m^2\Gamma^2}{2}\left|\chi(\omega)\right|^2\varepsilon C_{\mathrm{om}}^2\right] + \cos(\phi)\sin(\phi)2m\omega_m\Gamma\ \mathrm{Real}\left[\chi(\omega)\right]\sqrt{\varepsilon C_{\mathrm{om}}^2}\Bigg\} \tag{4.5}$$

Here we have assumed that all inputs, $\hat{X}^{\mathrm{in}}_{\mathrm{mech}}$, $\hat{X}^{\mathrm{in}}_{\mathrm{AM}}$, and $\hat{X}^{\mathrm{in}}_{\mathrm{PM}}$, corresponding to optical vacuum quadratures and the mechanical thermal bath, are uncorrelated at different times and with each other, such that each obeys $\langle X_i^{\mathrm{in}}(\omega)X_j^{\mathrm{in}}(\omega')\rangle = \delta(\omega-\omega')\delta_{i,j}$ with $\{i,j\} = \{\mathrm{mech},\mathrm{AM},\mathrm{PM}\}$.

We see that $S(\phi,\omega)$ reduces to the PM power spectral density discussed in Ch. 3 when $\phi = \pi/2$. The important term for ponderomotive squeezing is the final term that links X_{AM} and X_{PM} and disappears whenever measuring exactly the PM or AM quadrature. At certain quadrature angles and frequencies it can turn negative. However, its contribution to the overall noise power is only non-negligible near mechanical resonance, since $\chi(\omega)$ falls off quickly. If the thermal mechanical motion is not too large, then a negative correlation term can in turn lead to an overall reduction in the PSD below its shot-noise level. It is clear that this negative correlation grows with increasing C_{om} and also depends on detection efficiency. Additionally, from the prefactor $\cos(\phi)\sin(\phi)$, it is obvious that the correlation appears neither in the AM nor in the PM quadrature.

Figure 4.3 shows four calculations of predicted ponderomotive squeezing as a function of frequency and quadrature angle for typical experimental conditions, assuming the probe is resonant with the cavity[3]. The white contours outline the regions of the plot where the noise falls below the vacuum level. At higher C_{om}, the depth of the squeezing increases, but the region over which this squeezing occurs narrows. This is because the increased backaction at higher C_{om} contributes additional noise which is present to some extent at every quadrature angle save identically $\phi = 0$. Another aspect of the squeezing to notice is that for a given frequency, the quadrature opposite the squeezing shows increased noise. Even a squeezed state must obey the Heisenberg uncertainty principle, such that a squeezed quadrature necessitates an opposing anti-squeezed quadrature. Finally, one can see that no squeezing occurs in any quadrature at frequency ω_m. This is because Real $[\chi(\omega)]$ (plotted in

[3]The formal derivation of the measurement of ponderomotive squeezing on cavity resonance deserves a note. When considering the linear optomechanical amplifier theory of Ref. [56], one must be careful in taking the limit as Δ_{pc} goes to 0. While the value of the optomechanical gain G does go to zero in this limit, the ratio G/Δ_{pc}, which appears in some matrix elements, does not necessarily become zero. In fact, we find in this limit that on cavity resonance, there is no optical transduction of PM fluctuations to AM. However, AM optical inputs are transduced into AM optical outputs and, by way of the oscillator coupling, PM optical outputs. Mechanical inputs are transduced only onto the PM optical quadrature with on-resonant probing. Generally, this is why we choose to measure external forces applied to our oscillator via the output PM quadrature of our light.

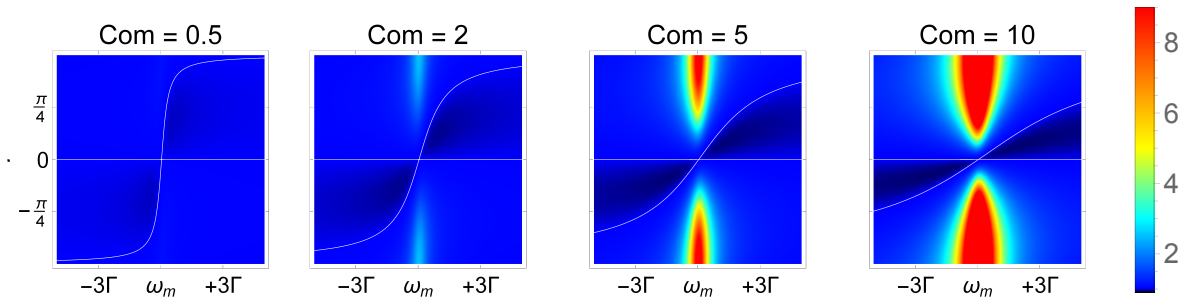

Figure 4.3: Predicted optomechanical response for different values of C_{om}, with $\Delta_{pc} = 0$, shown as a function of quadrature angle ϕ (ordinate) frequency ω (abcissa), for typical experimental parameters: $\kappa = 2\pi\times$ 1.82 MHz, $\omega_m = 2\pi\times$ 110 kHz, $\Gamma = 2\pi\times$ 3 kHz, $\varepsilon = 6\%$. The regions of squeezing, where the response in units of optical shot-noise, drops below 1, are outlined by white contours.

Fig. 4.4) crosses zero at $\omega = \omega_m$. In fact, $\chi(\omega_m)$ is completely imaginary. Recall from the force sensitivity measurement that this is the frequency where the system is most susceptible to forces. This suggests that ponderomotive squeezing may not be useful for improving upon the detection of applied forces. I will return to this point in greater detail later in this chapter.

So far we have assumed that the probe is resonant with the cavity. Detuning of the probe leads to some qualitatively different behavior for the optomechanical interaction that produces squeezing. To first order, the detuning of the probe causes a rotation of the quadratures of the light as they transit the cavity. This can be seen in Fig. 4.5, where the quadrature of maximum optomechanical response shifts from approximately $\pi/4$ for the red-detuned case to $-\pi/4$ for the blue-detuned case. Additionally, it is apparent that the detuning shifts the mechanical response frequency. This effect is known as the optomechanical spring shift, an effect well detailed in Ref. [34, 38]. The final consequence of detuning is the opening and closing of a region of squeezing at the shifted mechanical response frequency, due to optomechanically-induced amplification and damping of the mechanical response. That squeezing is predicted at the shifted mechanical resonance for red-detuned probe light could show promise for force detection. However, the theory predicts (and Ref. [26] shows experimentally) that even the smallest amount of thermal occupation of the oscillator is enough to swamp the squeezing closest to resonance, leaving only the troughs at farther frequencies observable.

4.3 Experimental observation

Ponderomotive squeezing has now been reported in three different optomechanical systems: our ultracold atomic oscillator [26], a vibrating photonic crystal cavity [27], and a silicon nitride membrane [28]. In each of these realizations, its observation required careful control of experimental noise sources. As in our force sensitivity measurement, we benefited from having prepared a ground-state oscillator well isolated from mechanical perturbations.

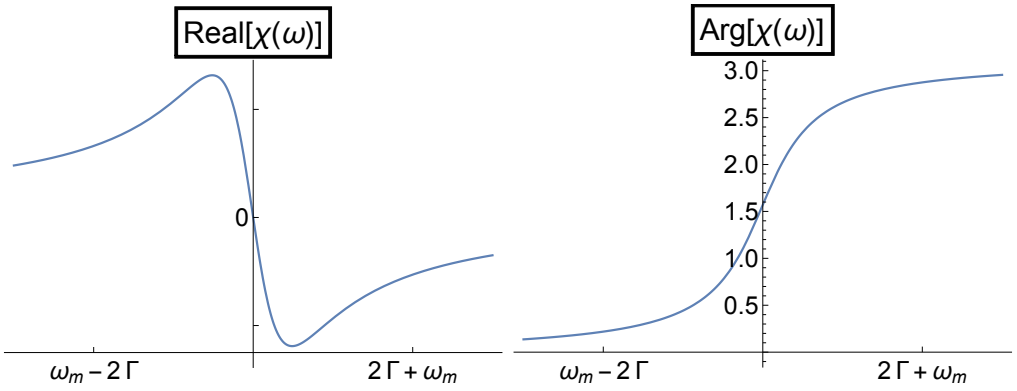

Figure 4.4: Spectrum of the real part of mechanical susceptibility $\chi(\omega)$ (left). The ponderomotive interaction is proportional to Real $[\chi(\omega)]$, and thus crosses zero at $\omega = \omega_m$. This zero crossing occurs because the argument of $\chi(\omega)$ (right), is $\pi/2$ at $\omega = \omega_m$. The amplitude of $\chi(\omega)$ is nonetheless maximized at this frequency, a fact which may be exploited to achieve better sensitivity, as I will discuss in Ch. 5.

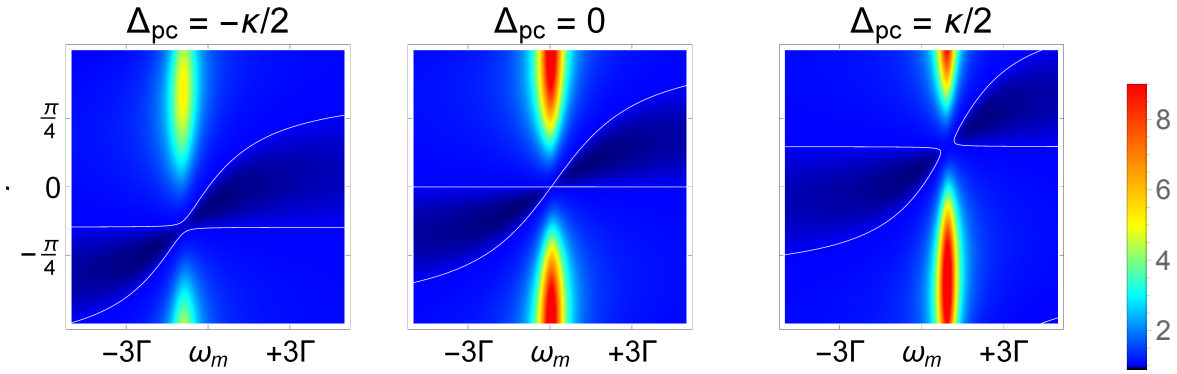

Figure 4.5: Predicted optomechanical response for different values of Δ_{pc}, with $C_{\rm om} = 5$, shown as a function of quadrature angle ϕ (ordinate) frequency ω (abcissa), for the same experimental parameters as in Fig. 4.3. Though it seems that now there is some squeezing near the (shifted) mechanical resonance in the red-detuned case, this squeezing is predicted (and observed [26]) to disappear almost as soon as any additional thermal phonons are introduced.

Other important experimental tools that were key to the result were the introduction of heterodyne detection (previous measurements had all been made by photon counting) and improvements to the experimental stability that allowed for consistent experimental parameters over many-day data taking sessions. The former allowed us to tune carefully the detection quadrature and thereby map the squeezing in quadrature maps, as shown in this chapter. The latter consisted of the introduction of the wavemeter lock described in Ch. 2 as well as an analog heterodyne phase lock that was the precursor to the digital heterodyne phase rotation also described in Ch. 2. Both were necessary since the slight depth of ponderomotive squeezing together with our limited detection efficiency and atomic oscillator lifetime required the averaging of many realizations of the squeezing interaction over the course of a week of nearly non-stop data acquisition.

Each experimental realization consists of the following succession of events. First, an atomic oscillator is prepared as described in Ch. 2 and positioned within the optical cavity such that it has linear coupling to the probe field. The probe light frequency is then swept quickly from very far below cavity resonance to a final frequency of approximately $\Delta_{pc} = -1.1$ MHz (so chosen as to encourage maximal squeezing in the AM quadrature). At this point, the oscillator is permitted to interact with the probe field for 10's of milliseconds, during which time the probe light exiting the cavity is recorded on a heterodyne receiver. Ultimately, we only use 5 ms of each data stream, due to observed heating of the oscillator that makes it unusable beyond this period. A small percentage of the exiting probe light is redirected onto a single photon counting module (SPCM) where its power, combined with the knowledge of the probe power that was incident on the cavity, determines Δ_{pc} and can be fed back to the frequency control of the probe[4]. After the data acquisition period, the atoms are driven out of the cavity by briefly extinguishing the trap light and turning on very bright imaging light resonant with the atomic transition, the pressure of which expels the atoms from the cavity region. Next the same measurement of probe light exiting the cavity is performed, although now it carries the record of an empty cavity. Finally, and importantly for the determination of optical shot-noise, the probe light is extinguished and the heterodyne receiver records the beating of the LO with only the vacuum. This sequence is repeated, in the case of Ref. [26] approximately 2000 times, ultimately providing 10 seconds of data over which to average the optomechanical record. The recorded data are analyzed as described in Ch. 2 in order to acquire the quadrature-dependent spectral response, which can be compared to the responses without atoms and additionally without probe light. We are thus able to plot spectra in units of heterodyne shot-noise power by performing the following normalization:

$$S_{\text{het}} = \frac{S_{\text{atoms}} - S_{\text{empty}}}{S_{\text{LO}}} + 1, \tag{4.6}$$

with S_{atoms}, S_{empty}, and S_{LO} the PSDs for the measurements with atoms, without atoms, and without probe, respectively. The additional "+1" exists so that plotted records have a

[4]In all experiments since this one, we have used a different kind of frequency stabilization employing phase-modulated sidebands applied to the probe and detected only with the heterodyne receiver, acting more like a Pound-Drever-Hall lock in transmission. Thierry Botter's thesis [48] details this locking method.

baseline of one unit of shot-noise.

Because the ultimate effect of ponderomotive squeezing was small, we underwent careful error analysis to identify any and all systematic errors that could contribute to our measurement. The results of this analysis are detailed in the supplementary information of Ref. [26]. I will highlight the characterization of the contribution of LO power variations here, since it is relevant to the discussion of new data presented in this chapter. In order to determine whether an optical state is squeezed, the vacuum noise level must be carefully determined. For this reason, we record the heterodyne spectrum of the empty cavity and of just the LO in quick succession after the spectrum with atoms is recorded, repeating these three measurements each experimental cycle. Since the shot-noise power, $S_{\mathrm{SN}} = P_{\mathrm{LO}}\hbar\omega_p$ (where ω_p is the probe frequency), can vary with the LO power P_{LO}, the hope is that any variations in P_{LO} will happen on a time scale slower than the few seconds between these recordings. Any drifts between experimental repetitions, which happen every 40 seconds, will be common to the three measurements and therefore be eliminated in the normalization step of Eq. 4.6. If, despite our best attempts, P_{LO} is always slightly lower for measurements performed with atoms as compared to those performed without probe light, this could give the appearance of a reduction of optical noise that would mimic squeezing. By performing careful statistical analysis of the spectra at frequencies far from those where optomechanical transduction is expected, we found a small systematic reduction in S_{SN} for measurements with atoms, shown in Fig. 4.6, and were able to estimate the uncertainty this reduction contributed to our measurement. We ultimately determined that the slight correction to our measured squeezing depth was at a level of 10^{-4} times shot-noise, and we included this information in our reported squeezing level.

All of this error analysis was performed in the AM quadrature, where the squeezing was quantified and reported. There was even more technical probe noise in the PM quadrature. We were careful to verify that our light was shot-nose limited in the AM quadrature, such that all amplitude fluctuations were no greater than those expected for vacuum[5]. Because the mechanical oscillator is only driven by amplitude fluctuations of the light, additional phase noise does not alter the fact that the optomechanical response we typically measure is driven by radiation pressure shot-noise. Additionally, since the squeezing measured in Ref. [26] was reported for the AM quadrature, we were sure that measured suppression of noise meant observation of squeezing since that quadrature was already limited to the vacuum level. However, when we try to observe squeezing in any other quadrature, we run up against the obscuring effect of technical phase fluctuations of the probe light, as shown in Fig. 4.7. In these data, we inject light resonant with the cavity, such that squeezing occurs primarily in quadratures that are a mix of AM and PM. The reduction of noise shown is therefore a reduction of technical noise. While we cannot state that it is squeezing, its trend follows the predictions of Fig. 4.3, suggesting that if we were to take pains to reduce technical PM laser noise, we could observe squeezing under these experimental conditions. It turns out that

[5]One can verify that light is shot-noise limited by observing how the measured power at a relevant frequency scales with increasing probe power. Shot-noise should rise linearly, while technical noise will typically be of quadratic or higher order in the input power.

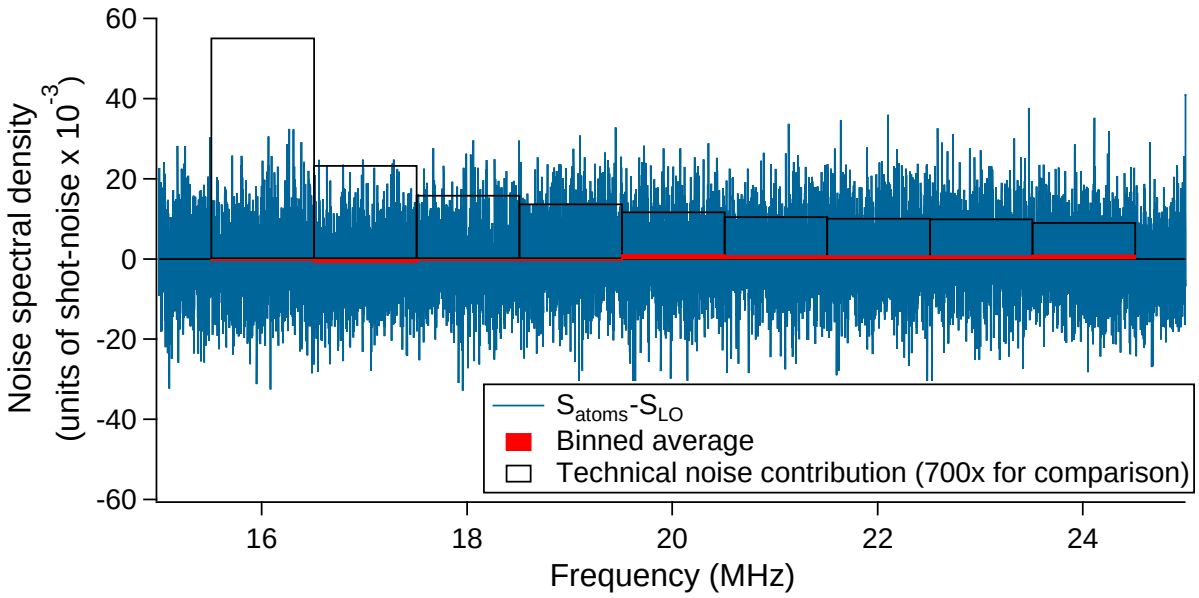

Figure 4.6: Difference between noise power for heterodyne measurements made with signal light, S_{atoms}, and noise power for heterodyne measurements made without signal light, S_{LO}, for experimental results reported in Ref. [26]. The binned average, over the 15-25 MHz range considered, gave a net difference of about 0.01% of shot-noise, with standard deviation of 0.05% for a 1 MHz bins. We found that a small portion (only 1.2±0.2%) of this difference could be described by technical noise on the probe light, well within the ±0.05% standard deviation of the measurement. We thus recorded an overall systematic correction of our measured squeezing uncertainty of $0 \pm 5 \times 10^{-4}$ relative to shot-noise.

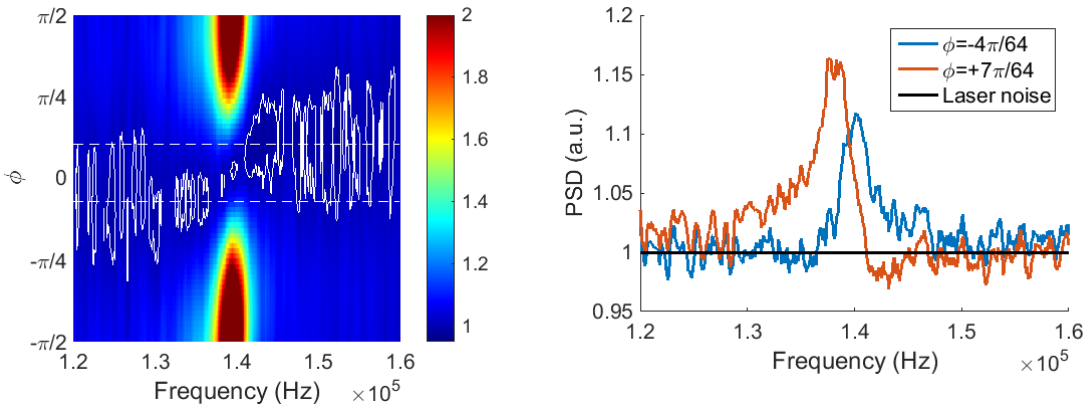

Figure 4.7: Experimental data showing technical noise reduction due to ponderomotive interaction for $\Delta_{pc} = 0$. Data are normalized to S_{empty}, giving the technical noise level. The regions of "squashing" of noise, outlined in white contours, behave like ponderomotive squeezing calculated in Fig. 4.3, but cannot be termed thus because the noise is not reduced below its vacuum value. The dashed white lines in the quadrature map on the left correspond to the quadratures plotted on the right.

such an exercise might not be so painful after all, as we observe that the laser phase noise falls further with increased frequency and appears to be shot-noise limited at frequencies a few hundred kilohertz from the heterodyne carrier. We are limited in our optomechanical frequency by available ODT laser power, but increasing laser power is often by comparison a simpler task than noise hunting.

After the original observation of ponderomotive squeezing, we installed the optical superlattice, allowing for the introduction of multiple spectrally-distinct mechanical oscillators. A natural question that arose was how one oscillator would react to the squeezed vacuum produced by another, and whether this response would be observable. The motivation for this investigation was two-fold. First, the "sensing oscillator" would observe the ponderomotively squeezed light within the cavity, where the squeezing has not yet been impaired by the losses that eventually contribute to our overall detection efficiency. Though our original measurement of ponderomotive squeezing showed a small effect (only 1.2% of shot-noise), the squeezing within the cavity could be as much as 20 dB. Second, we wondered if by placing one oscillator within an AM-quadrature squeezing trough of another we could perform a more sensitive force measurement thanks to the reduced backaction. In light of our work on multi-oscillator optomechanics in Ref. [38], we now believe that these motivations were misguided, as we have come to understand that the hybridization of mechanical modes through cavity-mediated coupling will most likely lead to a single squeezing interaction in much the same way as the single oscillator case. Figure. 4.8 shows some early attempts at such measurements. Three oscillators interact with the probe field at different detunings. The squeezing trends are similar to those predicted in Fig. 4.5, though now with three clear

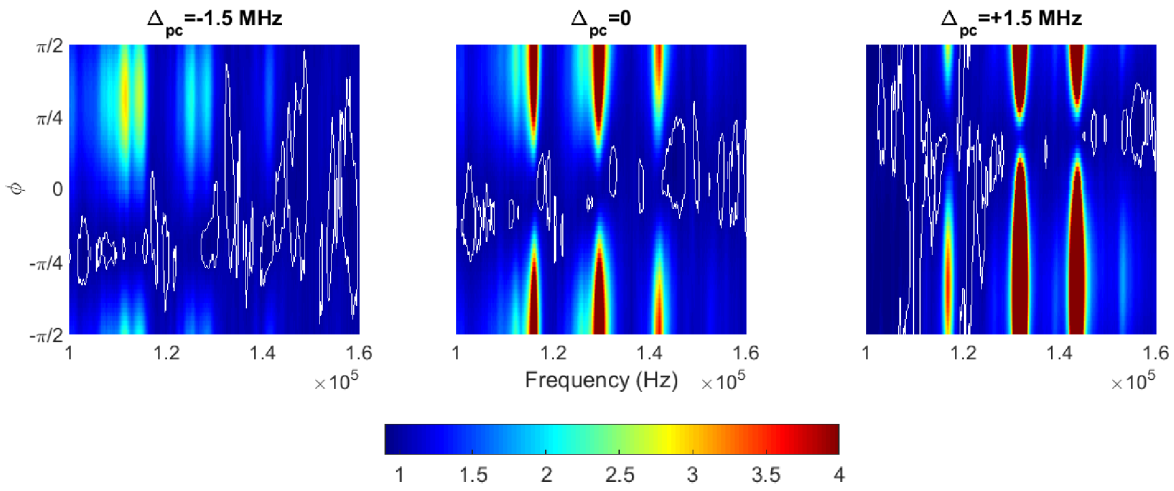

Figure 4.8: Experimental data showing technical noise reduction due to ponderomotive interaction for three oscillators (with unshifted resonances at 118, 130, and 141 kHz). The regions of "squashing" of noise, outlined in white contours, behave like ponderomotive squeezing calculated in Fig. 4.5, but cannot be termed thus because the noise is not reduced below its vacuum value. The left and center figures show secondary peaks for some oscillators due to heating in the anharmonic trap, discussed in Ch. 3.

oscillator peaks. Again, probe phase noise means that the regions of noise reduction do not necessarily dip below the vacuum level, except near the AM quadrature. Though the appearance of noise dips on either side of the highest frequency oscillator for the red-detuned case may suggest that it sits in a squeezing trough produced by the two lower-frequency oscillators, the effect of this on overall optomechanical response is difficult to say. This is because changes of backaction driven response height are difficult to discern from the effects of oscillator coupling which hybridize the oscillator modes in such a way that their coupling to the probe light differs. This hybridization and redistribution of backaction occurs independently of any squeezing of the probe light, and is explored in Spethmann et al. [38].

4.4 Squeezing force sensitivity

I would now like to return to the question of whether ponderomotive squeezing can help with force sensitivity for a single oscillator. In general, we presume that any reduction of optical noise near mechanical resonance could help our cause. However, in the case of noise reduction via ponderomotive squeezing, a couple of obstacles stand in the way. One is that the squeezing often primarily appears in the wrong quadrature, opposite the mechanical response. Another is that squeezing is necessarily suppressed at mechanical resonance, where, as shown in Fig. 4.4, the real part of $\chi(\omega)$ goes to zero. Unfortunately, mechanical resonance, we have learned, is where force sensitivity is finest. The top row of Fig. 4.9 shows mechanical

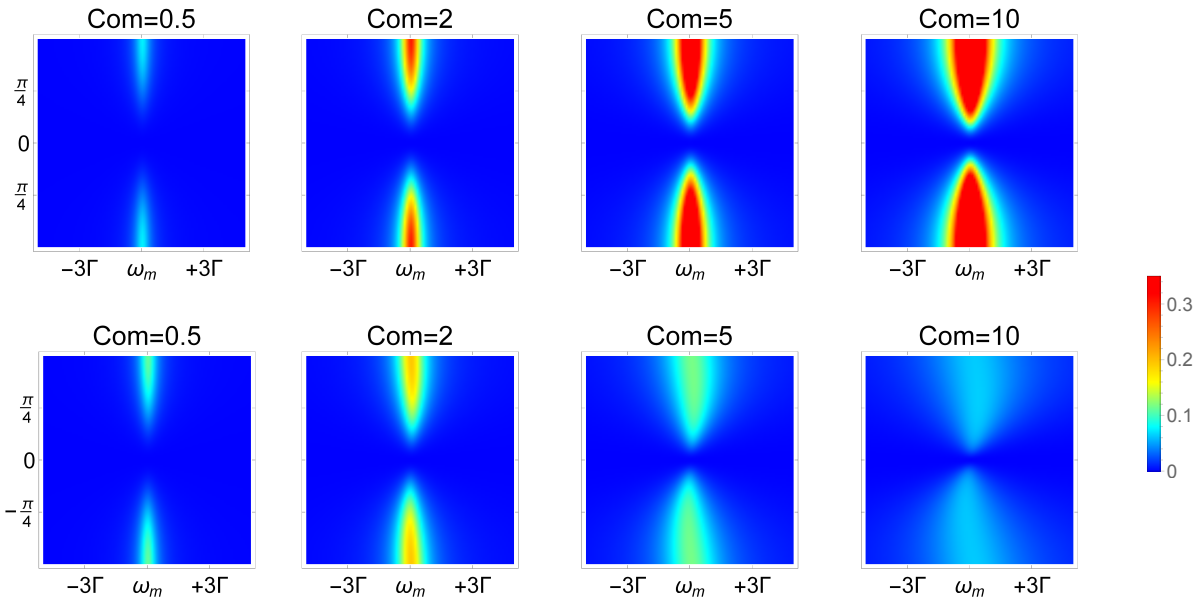

Figure 4.9: Predicted mechanical susceptibility (top) and force sensitivity (bottom) for different values of $C_{\rm om}$, with $\Delta_{pc} = 0$, shown as a function of quadrature angle ϕ (ordinate) frequency ω (abcissa), for typical experimental parameters: $\kappa = 2\pi\times$ 1.82 MHz, $\omega_m = 2\pi\times$ 110 kHz, $\Gamma = 2\pi\times$ 3 kHz, $\varepsilon = 6\%$. The force sensitivity plots (bottom) are found by taking the ratio of the susceptibilities (top) to the noise spectra of Fig. 4.3. The onset of ponderomotive squeezing for $C_{\rm om} \geq 2$ may influence the location of optimal sensitivity in the quadrature maps.

susceptibility as a function of frequency and quadrature angle for different values of $C_{\rm om}$. The ratio of the spectra in Fig. 4.3 to these susceptibilities gives the sensitivity to applied force, plotted in the bottom row of Fig. 4.9. The appearance of squeezing, which starts to take effect as backaction becomes a dominant contributor to the noise ($C_{\rm om} \gtrsim 2$ for detection efficiency ε=0.6), affects slightly the frequency and quadrature of the highest sensitivity regions. However, these sensitivities do not appear to exceed the SQL (recalling that the SQL is the sensitivity in the PM quadrature at mechanical resonance, and is observed when $C_{\rm om} \approx 2$).

Since the plots in Fig. 4.9 only give a vague sense of the sensitivities we could expect if we allow ourselves to search the (ϕ, ω) parameter space, we perform an optimization on experimental parameters to find the best settings for force sensitivity. This may lend insight into whether excursions into regions with squeezing ever help the cause. Figure 4.10 shows the parameters recovered for best sensitivity (that is, minimum S_{FF} or maximum signal-to-noise $1/S_{FF}$), for values of detuning $-\kappa \leq \Delta_{pc} \leq +\kappa$. Different detunings shift the $C_{\rm om}$ at which the best sensitivity occurs, and the sensitivity itself appears to depend on Δ_{pc}, decreasing as the detuning moves from blue to red. Also plotted are the frequency and quadrature angle at which this maximum sensitivity occurs. The changing frequency with detuning and

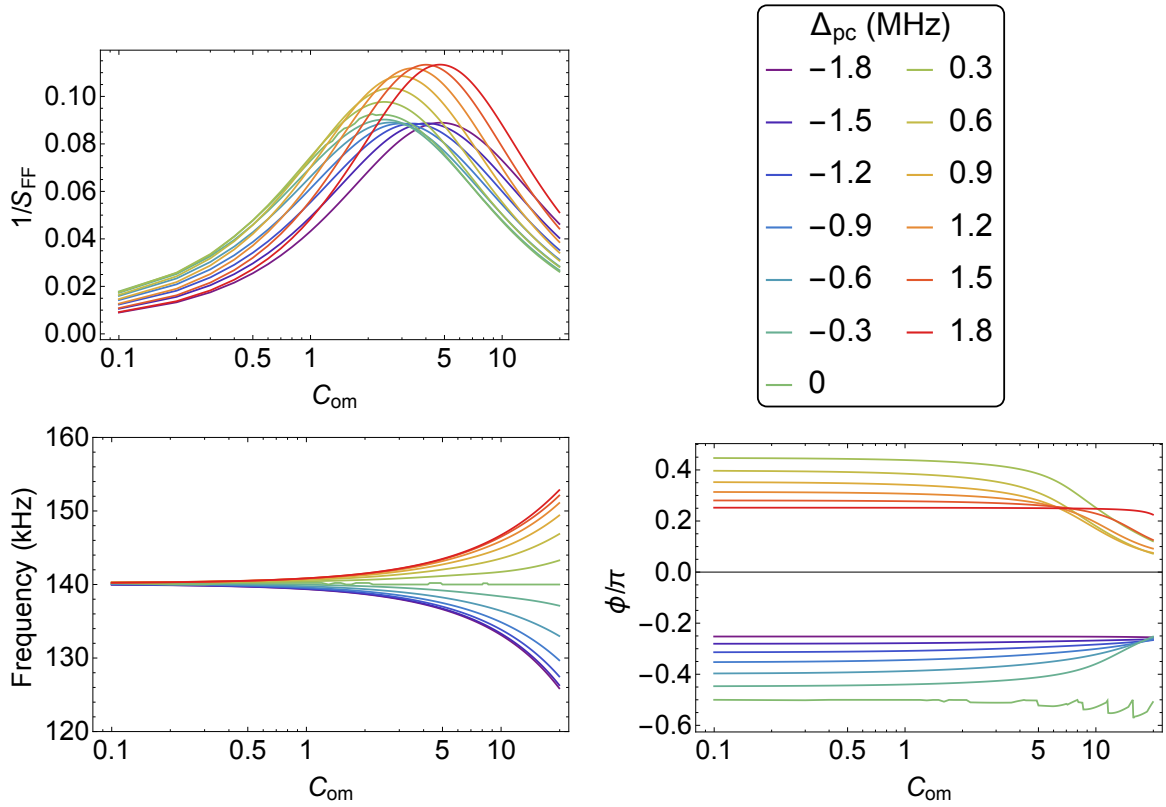

Figure 4.10: Results of optimization on ϕ and ω to recover the best force sensitivity as Δ_{pc} and C_{om} are varied. The result of detuning the probe is to shift the optimal measurement frequency, due to the optical spring shift, and the optimal measurement quadrature, possibly due to the presence of ponderomotive squeezing. At high values of C_{om}, where squeezing troughs are narrow, the optimization algorithm has some difficulty, as observed in the bottom right panel.

cooperativity can be explained by the optical spring shift. This frequency change accounts for the differences in optimal sensitivity, since S_{FF} has a prefactor of $p_{\mathrm{HO}}^2 \propto \omega_m$.

What about these results can hint at the role of squeezing in force sensitivity? The frequency of optimal sensitivity is always found to be close to (but not exactly at) the shifted mechanical resonance. We know that squeezing usually occurs away from that frequency, which may downplay its importance. However, the observed quadrature for optimal sensitivity may support the case of squeezing. At low C_{om}, where squeezing does not occur, the optimal response quadratures correspond to those where the typical maximum mechanical response to shot-noise occurs, rotated of course due to the detuning. However, as C_{om} climbs to values where we know squeezing sets in, the optimal quadratures shift in a C_{om}-dependent fashion, though the cavity rotation of quadratures has no dependence on measurement strength. This suggests that the optimization routine may be finding the deep, narrow squeezing troughs that are very close to mechanical resonance but shifted in quadrature. This evidence is inconclusive, but it does motivate further investigation, since claims for [58] and against [56] the usefulness of ponderomotive squeezing in force measurements have been made in the literature.

Finally, the question remains as to whether the ponderomotive squeezing produced by one mechanical oscillator could help to measure forces applied to another oscillator in the same cavity with precision beyond the SQL. This is similar to proposals for introducing squeezed light created outside [58] or inside [66] a cavity optomechanical system to enhance sensitivity. We recorded the optomechanical spectra of multiple oscillators in Fig. 4.8. By the same reasoning that led us to conclude that one oscillator would not be effective in detecting the ponderomotive squeezing of another, we now believe that the effect of mode hybridization will mean no improvement in force sensitivity in the multioscillator case.

Chapter 5

Complex Squeezing

The very longest swell in the ocean, I suspect,
carries the deepest memory, the information of actions
summarized (surface peaks and dibbles and local sharp

slopes of windstorms) with a summary of the summaries
and under other summaries a deeper summary...

A. R. Ammons, "Swells", 1981

5.1 Introduction

In the last chapter, we found that ponderomotive squeezing was nonexistent at mechanical resonance as a consequence of the phase of $\chi(\omega_m)$. Since a homodyne measurement is only sensitive to the real part of χ, as shown in Eq. 4.5, our experimental methods did not have simultaneous access to the strongest correlated backaction noise in the PM quadrature that occurred exactly $\pi/2$ out of phase with its generating AM fluctuations. Figure 5.1 shows again the real and imaginary components of $\chi(\omega)$, now plotted parametrically on complex axes so as to demonstrate clearly that the largest extent of the susceptibility occurs along the imaginary axis. Knowing that these correlations, though not accessible via homodyne detection, nonetheless exist and are in fact strongest at this out-of-phase point, we wondered how we might obtain access to them. We imagine that instead of measuring a quadrature that is a linear combination of AM and PM, $\hat{X}(\phi) = \hat{X}_{\mathrm{AM}}\cos(\phi) + \hat{X}_{\mathrm{PM}}\sin(\phi)$, where the coefficients $\sin(\phi)$ and $\cos(\phi)$ are real, we would like instead to measure $\mu\hat{X}_{\mathrm{AM}} + \nu\hat{X}_{\mathrm{PM}}$, where μ and ν can be complex numbers. This could allow us, for example, to subtract the imaginary part of $\hat{X}_{\mathrm{PM}}$ that carries the backaction noise from the real part of $\hat{X}_{\mathrm{AM}}$ that generated the backaction, thus removing the correlated backaction from the measurement entirely. Since μ and ν could both be complex, the quadrature being measured would now be defined by two angles ϕ and θ, as we will show in the next section.

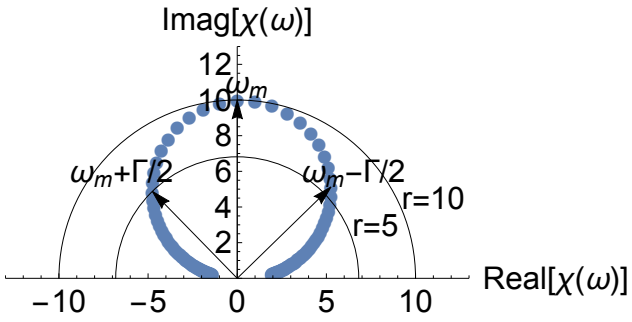

Figure 5.1: Parametric plot of the real and imaginary parts of $\chi(\omega)$ on complex axes, with points spaced by equal frequency. The greatest magnitude (largest excursion from the origin) occurs at ω_m, where the real part of the susceptibility vanishes. Half-circles show lines of constant magnitude.

Chapter 4 showed how in-phase correlations showing up at the wings of the susceptibility spectrum lead to ponderomotive amplification and squeezing of noise. In this chapter, I will describe how by selecting complex detection angles ϕ and θ properly, we propose to be able to subtract correlated noise at all frequencies in an optomechanical system in such a way as to take advantage of a new kind of squeezing, which we dub "complex squeezing" due to the nature of the correlations used. I will begin by providing intuition and some derivations for the parameters and limits of complex squeezing, hewing to the experimentalist's perspective. Then I will discuss the attempts to observe such squeezing experimentally, and what requirements might help in its future realization. Finally, I will introduce a novel detection scheme that would overcome the limits of homodyne detection and allow for improvements to force sensitivity, as described more extensively in Buchmann et al. [39].

5.2 Eigenmodes of complex squeezing

The simple description of quadrature squeezing given in Ch. 4 was one of the reduction of the noise, or uncertainty, of one quadrature (e.g. AM) of phase space below the vacuum level. When a quantum state is measured repeatedly, the experimental manifestation of this noise is the variance observed among the measurements. As soon as squeezing occurs, the phase space distribution no longer has the circular symmetry of the coherent state, as shown in the left panel of Fig. 5.2. The compression and elongation that characterize squeezing and anti-squeezing mean that there is now a non-zero covariance between quadratures in some basis. In Fig. 5.2, for example, correlations between X and Y (and Z in the three-dimensional case) are apparent due to the angle of the asymmetric distribution. The black lines show the eigenvectors of the distribution, which fall along the semi-major and semi-minor axis. They evidently follow the directions containing the least and the most noise: the squeezed and anti-squeezed quadratures.

Just as the squeezing in Fig. 5.2 does not occur in the (X, Y) basis, recall that quadrature squeezing is not restricted to just AM or PM variances, but can occur at some intermediate

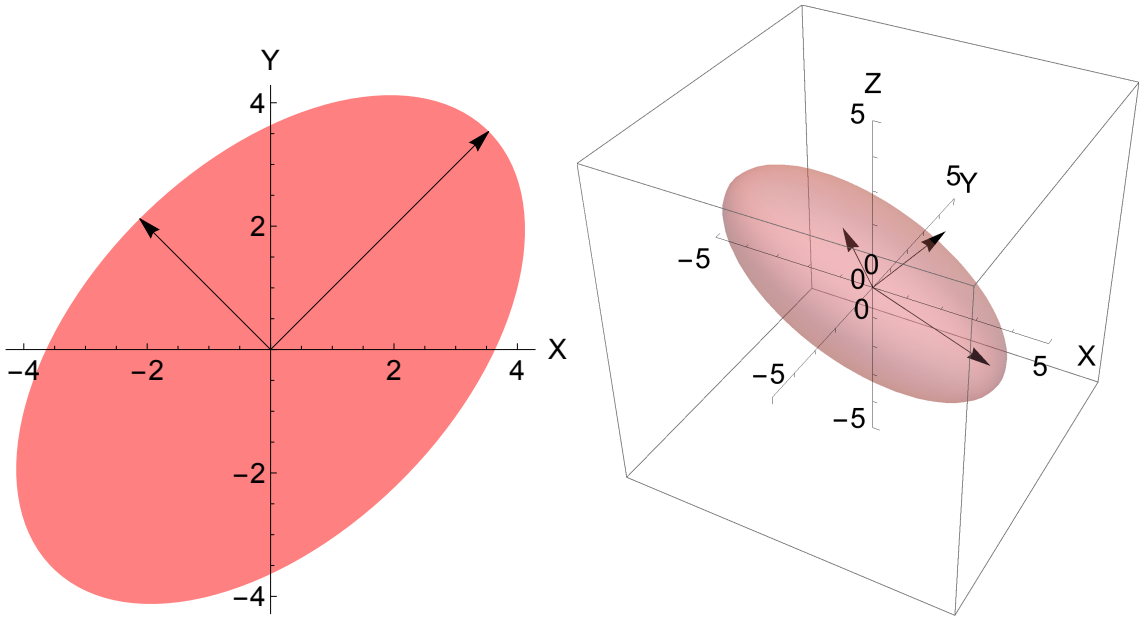

Figure 5.2: Principal component analysis yields the eigenvectors of the 2×2 (left) and 3×3 (right) covariance matrix. The black arrows point along the eigenvectors, which contain the least and greatest variances in the distribution. The lengths of the arrows give the eigenvalues.

quadrature angle ϕ. Such a rotation is evident in a phase plot like Fig. 5.2, or equivalently by examining the covariance matrix for noise in the AM and PM quadratures[1],

$$C\left(X_{\mathrm{AM}}, X_{\mathrm{PM}}\right) = \begin{pmatrix} \mathrm{Var}\left[X_{\mathrm{AM}}\right] & \mathrm{Cov}\left[X_{\mathrm{AM}}, X_{\mathrm{PM}}\right] \\ \mathrm{Cov}\left[X_{\mathrm{PM}}, X_{\mathrm{AM}}\right] & \mathrm{Var}\left[X_{\mathrm{PM}}\right] \end{pmatrix}. \tag{5.1}$$

For an uncorrelated coherent state, the off-diagonal covariance terms are zero, and this matrix is diagonal. In the case of squeezing at some intermediate angle $0 < \phi < \pi/2$, the matrix will no longer be diagonal, but will rather have eigenvectors at the squeezed and anti-squeezed quadrature angles. Characterization of the squeezing is therefore possible using principal component analysis to investigate the eigenmodes of the covariance matrix. Furthermore, if the state is gaussian (as is the case for most of the optical and mechanical states we create and measure in our experimental efforts), the covariance matrix actually contains all of the information about the state. Finally, were the phase-space three-dimensional, the same analysis could be extended to a 3×3 covariance matrix, resulting in 3 eigenmodes like those shown in the right panel of Fig. 5.2. A four-dimensional case, as will become important in the analysis of complex squeezing, is difficult to illustrate, but the same considerations also hold true.

In this section I will discuss quadrature squeezing in terms of the covariance matrix for quantum noise. I will then define the four Fourier transformed detection operators that can

[1] I will define the covariance matrix more carefully in the next section. In the meantime, here $\mathrm{Var}\left[X\right]$ means the variance of a value X, and $\mathrm{Cov}\left[X, Y\right]$ means the covariance of value X with value Y.

be combined so as to be sensitive to complex squeezing, studying their 4×4 covariance matrix for the resulting squeezed and anti-squeezed eigenmodes.

5.2.1 Generalized covariance matrices

I will take a somewhat more rigorous quantum optics approach in this chapter. To that end, here I will carefully detail the connection between the covariance matrix and quadrature squeezing.

Walls & Milburn [67] define the covariance matrix for two operators as

$$C\left(X_1, X_2\right)_{p,q} = \frac{1}{2}\left\langle\{X_p, X_q\}\right\rangle - \left\langle X_p\right\rangle\left\langle X_q\right\rangle \ (p, q = 1, 2), \tag{5.2}$$

where $\{,\}$ is the anticommutator. The anticommutator is required in describing the covariance matrix of quantum operators because in general (and in the cases we study here) X_1 and X_2 do not commute. Thus, while these operators may be Hermitian, their product may not be. A covariance matrix, even if it describes complex-valued variables, is real, symmetric, and positive definite, and thus Hermitian [68]. Therefore, we need to use the symmetrized product.

To align the definition of squeezing with the covariance matrix, I will follow arguments from Simon et al. [68] for the "characterization of variance matrices by uncertainty principles". Later, I will apply this characterization to understand the uncertainty principles we should expect for four newly defined Fourier-transformed operators. According to Ref. [68], classically, any real symmetric positive-definite matrix is a physically realizable variance matrix, as defined in Eq. 5.2 (though generally it can extend to $2n \times 2n$ in size, an extension we will need). In the quantum case there is an additional restriction required of a matrix in order for it to be a physically realizable variance matrix. This additional restriction, that

$$\det C \geq 1/4, \tag{5.3}$$

is the complete, precise statement of the Heisenberg uncertainty relation (which I will derive carefully later in this chapter). This restriction takes into account potential off-diagonal terms in the covariance matrix. Equation 5.3 does not negate the less careful (though often used) definition of the Heisenberg uncertainty relation, $\mathrm{Var}\left[X_1\right]\mathrm{Var}\left[X_2\right] \geq 1/4$. However, this narrowly defined inequality says nothing about the product of the variances along eigenvectors in a rotated quadrature, where there could be squeezing present. Simon et al. [68] define a squeezed state as one for which some transformed quadrature – obtained by applying a transformation that is part of the real symplectic group[2] $Sp(2n, \mathbb{R})$ to a vector of the harmonic oscillator quadratures – has variance of less than $1/2$. Furthermore they prove that a state with covariance matrix C is squeezed according to this definition if and only if the least eigenvalue of the matrix has a value of less than $1/2$.

[2] $Sp(2n, \mathbb{R})$ contains all real canonical linear transformations in $2n$ dimensions.

As a final note on this subject, Simon et al. [68] point out that the determinant that forms the left side of Eq. 5.3 is in fact invariant under such $Sp(2n, \mathbb{R})$ transformations. Let's take a moment to understand the scope of these transformations. For a Hermitian Hamiltonian that is quadratic in the canonical variables X_1 and X_2 (and therefore equivalently in a and $a^\dagger$), unitary evolution of the Hamiltonian produces $Sp(2, \mathbb{R})$ transformations on those canonical variables. This means that the matrix S that solves the canonical evolution equation

$$e^{iH} \begin{pmatrix} a \\ a^\dagger \end{pmatrix} e^{-iH} = S \begin{pmatrix} a \\ a^\dagger \end{pmatrix} \tag{5.4}$$

is a member of the symplectic group $Sp(2, \mathbb{R})$. Two such quadratic Hamiltonian terms that are important for us are those of form

$$\hat{H}(\theta) = \frac{\theta}{4} \left(a^\dagger a + a a^\dagger \right) \tag{5.5}$$

or

$$\hat{H}(z) = \frac{1}{4} \left(z a^{\dagger 2} + z^* a^2 \right). \tag{5.6}$$

The first is related to the normal harmonic oscillator Hamiltonian, and thus its evolution is just a rotation in phase space. In this case, the symplectic matrix that transforms the quadrature vector is

$$S(\theta) = \begin{pmatrix} \cos\theta & \sin\theta \\ -\sin\theta & \cos\theta \end{pmatrix}. \tag{5.7}$$

The second Hamiltonian is the quadrature squeezing interaction and evolves as a scaling in phase space along some axis. The symplectic matrix generating this transformation on the quadratures is then

$$S(z) = S(re^{i\theta}) = 2 \begin{pmatrix} \cosh(r/2) + \sinh(r/2)\sin(\theta) & -\sinh(r/2)\cos(\theta) \\ -\sinh(r/2)\cos(\theta) & \cosh(r/2) - \sinh(r/2)\sin(\theta) \end{pmatrix}. \tag{5.8}$$

Here r is the squeezing parameter, which compresses the state along axis θ.

If we are interested in how covariance matrices change under the evolution of a quadratic Hamiltonian, we simply transform them by the relevant symplectic matrix, such that $C' = S\,C\,S^T$. Since the determinant of Eq. 5.3 is invariant under these transformations, we know that the time-evolution of the harmonic oscillator and the introduction of quadrature squeezing leave the Heisenberg uncertainty principle intact. These rigorous definitions are useful since in this chapter we propose an entirely new form of squeezing – "complex squeezing" – which as yet has not been described. We would therefore like to justify calling this effect "squeezing". Furthermore, we may like to allow for states that are not stationary to be included as potential complex squeezed candidates. As such, understanding of how the Heisenberg uncertainty principle behaves in time will be important. It is heartening, therefore, to learn that the uncertainty bound is invariant under both the quadrature squeezing and the harmonic oscillator interactions.

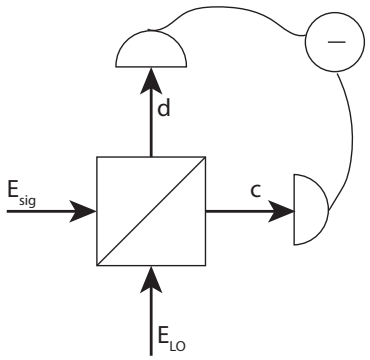

Figure 5.3: A beamsplitter combines the signal of interest $E_{\rm sig}$ with a classical local oscillator $E_{\rm LO}$. The resulting current on the output photodiodes contains information about the magnitudes and relative phase of the two electric fields. Subtracting the currents of the two photodiodes cancels common-mode noise.

5.2.2 Homodyne quantum operators

After considerable buildup, I will now describe how the four detection operators of interest come about. Though quadrature operators $\hat{X}_{\rm AM}$ and $\hat{X}_{\rm PM}$ are Hermitian, with real observable eigenvalues, homodyne detection actually gives us access to two complex quantities $\tilde{X}_{\rm AM}(\omega)$ and $\tilde{X}_{\rm PM}(\omega)$, which are complex because of the Fourier transform used to obtain them. These can equivalently be expressed as four real-valued quantities, which are directly accessible in our experimental apparatus. Our hope is that by choosing the correct combination of these four quantities, we can access some combination of $\hat{X}_{\rm PM}$ and $\hat{X}_{\rm AM}$ that allows us to subtract correlated noise in such a way so as to observe complex squeezing. We will find, however, that homodyne detection does not give us simultaneous access to the necessary components, and that we must devise another detection method to observe this squeezing.

To define the four homodyne detection operators, we consider the simple case of a quantized signal field

$$E_{\rm sig} = a(t)e^{-i\omega_c t} + a^\dagger(t)e^{i\omega_c t}, \tag{5.9}$$

with ω_c the carrier frequency for the coherent tone and $a(t)$ the amplitude of the field. We will let the time dependence of $a(t)$ remain general. Note that I have not defined $a(t)$ as the harmonic oscillator lowering operator, since the amplitude of E_{sig} may be of a more complicated form. A homodyne detection is performed by combining this signal field on a beamsplitter (depicted in Fig. 5.3) with a classical local oscillator of fixed amplitude $|\alpha|$,

$$E_{\rm LO} = |\alpha|e^{-i\omega_c t+i\theta} + |\alpha|e^{i\omega_c t-i\phi}, \tag{5.10}$$

rotating at carrier frequency ω_c and with ϕ the phase relative to the signal at time $t = 0$. The field that exits one port of the beamsplitter is given by

$$c(t) = a(t)e^{-i\omega_c t} + |\alpha|e^{-i\omega_c t+i\phi}, \tag{5.11}$$

(where I have let ϕ absorb the extra $\pi/2$ phase that comes with reflection) and the intensity of the beat note measured by a subsequent photodetector is

$$\begin{aligned} I_c(t) &= c^\dagger(t)c(t) \\ &= a^\dagger(t)a(t) + |\alpha|^2 + |\alpha|a^\dagger(t)e^{i\phi} + |\alpha|a(t)e^{-i\phi}. \end{aligned} \tag{5.12}$$

If we perform balanced detection (subtracting I_d from I_c in Fig. 5.3), the first two terms of this equation drop out, while the last two are doubled. Therefore, we will focus on the latter terms for the duration of this section.

$$I(t) \propto |\alpha|a^\dagger(t)e^{i\phi} + |\alpha|a(t)e^{-i\phi} \tag{5.13}$$

We are interested in the terms that result from taking the Fourier Transform of $I(t)$:

$$I(\omega) \propto \int_0^T dt \left[a^\dagger(t)e^{i\omega t + i\phi} + a(t)e^{i\omega t - i\phi}\right]. \tag{5.14}$$

We are concerned with conjugate quadratures AM ($\phi = 0$) and FM ($\phi = \pi/2$). We expand the integrands for each case:

$$\begin{aligned} I_{\mathrm{AM}}(\omega) &\propto \int_0^T dt \left\{a^\dagger(t)\left[\cos(\omega t) + i\sin(\omega t)\right] + a(t)\left[\cos(\omega t) + i\sin(\omega t)\right]\right\} \\ &= a^\dagger(\omega) + a(\omega), \end{aligned} \tag{5.15}$$

$$\begin{aligned} I_{\mathrm{PM}}(\omega) &\propto \int_0^T dt \left\{a^\dagger(t)\left[\cos(\omega t) + i\sin(\omega t)\right] - a(t)\left[\cos(\omega t) + i\sin(\omega t)\right]\right\} \\ &= a^\dagger(\omega) - a(\omega). \end{aligned} \tag{5.16}$$

Both of these have real and imaginary components. Note that we have pulled an overall phase factor i out of $I_{\mathrm{PM}}(\omega)$. This is in keeping with the understanding that $I(\omega) = I_{\mathrm{AM}}(\omega) + iI_{\mathrm{PM}}(\omega)$.

We will treat each component of AM and of PM as its own operator, meaning we will have four total operators among which to look for correlations.

$$\begin{aligned} \tilde{X}^{\mathrm{Re}}_{\mathrm{AM}}(\omega) &= \mathrm{Real}\left[I_{\mathrm{AM}}(\omega)\right] \\ &= \int_0^T dt \left[a^\dagger(t)\cos(\omega t) + a(t)\cos(\omega t)\right] \\ &= a^\dagger(\omega) + a^\dagger(-\omega) + a(\omega) + a(-\omega) \\ &= \tilde{X}_{\mathrm{AM}}(\omega) + \tilde{X}_{\mathrm{AM}}(-\omega) \end{aligned} \tag{5.17}$$

$$\begin{aligned} \tilde{X}^{\mathrm{Im}}_{\mathrm{AM}}(\omega) &= \mathrm{Imag}\left[I_{\mathrm{AM}}(\omega)\right] \\ &= \int_0^T dt \left[a^\dagger(t)\sin(\omega t) + a(t)\sin(\omega t)\right] \\ &= -i\left(\tilde{X}_{\mathrm{AM}}(\omega) - \tilde{X}_{\mathrm{AM}}(-\omega)\right) \end{aligned} \tag{5.18}$$

$$\begin{aligned}\tilde{X}^{\mathrm{Re}}_{\mathrm{PM}}(\omega) &= \mathrm{Real}\left[I_{\mathrm{PM}}(\omega)\right] \\ &= \int_0^T dt\left[a^\dagger(t)\cos(\omega t) - a(t)\cos(\omega t)\right] \\ &= \tilde{X}_{\mathrm{PM}}(\omega) + \tilde{X}_{\mathrm{PM}}(-\omega)\end{aligned} \tag{5.19}$$

$$\begin{aligned}\tilde{X}^{\mathrm{Im}}_{\mathrm{PM}}(\omega) &= \mathrm{Imag}\left[I_{\mathrm{PM}}(\omega)\right] \\ &= \int_0^T dt\left[-a^\dagger(t)\sin(\omega t) + a(t)\sin(\omega t)\right] \\ &= i\left(\tilde{X}_{\mathrm{PM}}(\omega) - \tilde{X}_{\mathrm{PM}}(-\omega)\right)\end{aligned} \tag{5.20}$$

Thus we see that homodyne detection gives us two complex spectra, or equivalently four real-valued spectra. We suspect that correlations can arise, for example, between $\tilde{X}^{\mathrm{Re}}_{\mathrm{AM}}$ and $\tilde{X}^{\mathrm{Im}}_{\mathrm{PM}}$ at $\omega = \omega_m$ for optomechanical interactions. Therefore, we imagine that an eigenmode of the 4×4 covariance matrix with a vector positive along one of these axes and negative along another might show suppressed noise consistent with our definition of squeezing. The weights of the contributions from these four operators to the eigenmodes would be the real and imaginary parts of the complex μ and ν we imagined at the beginning of the chapter.

5.2.3 Limits on squeezing

What level of noise suppression defines squeezing among these new homodyne operators? That is, what are limits on the 4×4 covariance matrix for the new homodyne operators analogous to that given in Eq. 5.3? In the 2×2 case, this limit was exactly the Heisenberg uncertainty principle. To expand to the 4×4 case, we will first look at how that inequality is derived. Here I follow closely the derivation in Ch. 9 of Shankar [69].

Let us assume that X_1 and X_2 are Hermitian. Their variances are given by

$$\sigma^2_{X_i} = \left\langle \left(X_i - \langle X_i\rangle\right)^2 \right\rangle, i = \{1, 2\}. \tag{5.21}$$

With no loss of generality[3], we will let both $\langle X_i\rangle = 0$. Also, noting that they are Hermitian, we can say that their commutator has the form $[X_1, X_2] = i\Gamma$, where Γ is a Hermitian operator. The product of the variances is

$$\sigma^2_{X_1}\sigma^2_{X_2} = \left\langle X_1^2\right\rangle \left\langle X_2^2\right\rangle. \tag{5.22}$$

[3] If $\langle X_i\rangle \neq 0$, this is equivalent to a coherent displacement in phase space, which does not affect the noise distribution. Application of the displacement operator to a state centered at the origin in order to produce such an offset does not affect the results of the derivation.

The Cauchy-Schwarz inequality allows us to compare the expectation value of the product of X_1 and X_2 to the product of their expectation values: $\langle X_1\rangle^2\langle X_2\rangle^2 \geq |\left\langle X_1^\dagger X_2\right\rangle|^2$. Therefore, the product of variances is subject to the inequality:

$$\begin{aligned}\sigma_{X_1}^2\sigma_{X_2}^2 &= \left\langle X_1^2\right\rangle\left\langle X_2^2\right\rangle \\ &= \left|\left\langle X_1^\dagger X_2\right\rangle\right|^2 = \left|\langle X_1 X_2\rangle\right|^2\end{aligned} \tag{5.23}$$

Next we invoke the following trivial equality: $X_1X_2 = 1/2\,\{X_1,X_2\}+1/2\,[X_1,X_2]$. Applying this to the variance inequality, we find:

$$\begin{aligned}\left\langle X_1^2\right\rangle\left\langle X_2^2\right\rangle &\geq \left|\left\langle \frac{1}{2}\{X_1,X_2\}+\frac{1}{2}[X_1,X_2]\right\rangle\right|^2 \\ &= \left|\left\langle \frac{1}{2}\{X_1,X_2\}+\frac{1}{2}i\Gamma\right\rangle\right|^2 \\ &= \frac{1}{4}\left|\langle\{X_1,X_2\}\rangle\right|^2+\frac{1}{4}\langle\Gamma\rangle^2 \\ &= \frac{1}{4}\left|\langle\{X_1,X_2\}\rangle\right|^2+\frac{1}{4}\left|\langle[X_1,X_2]\rangle\right|^2\end{aligned} \tag{5.24}$$

Now let's re-examine the covariance matrix as defined in Eq. 5.2. Consider first just a 2×2 matrix, $C\left(X_p,X_q\right) = 1/2\left\langle\{X_p,X_q\}\right\rangle - \left\langle X_p\right\rangle\left\langle X_q\right\rangle, (p,q=1,2)$. Assuming average values of X_1 and X_2 disappear, the determinant of this matrix is

$$\begin{aligned}\det\left(C\right) &= \frac{1}{4}\left\langle 2X_1^2\right\rangle\left\langle 2X_2^2\right\rangle - \frac{1}{4}\left\langle\{X_2,X_1\}\right\rangle\left\langle\{X_1,X_2\}\right\rangle \\ &= \left\langle X_1^2\right\rangle\left\langle X_2^2\right\rangle - \frac{1}{4}\left\langle\{X_2,X_1\}\right\rangle\left\langle\{X_1,X_2\}\right\rangle.\end{aligned} \tag{5.25}$$

Next we use Eq. 5.24 to put a lower bound on the value of the $\left\langle X_1^2\right\rangle\left\langle X_2^2\right\rangle$ term.

$$\det\left(C\right) \geq \frac{1}{4}\left|\langle\{X_1,X_2\}\rangle\right|^2 - \frac{1}{4}\left\langle\{X_2,X_1\}\right\rangle\left\langle\{X_1,X_2\}\right\rangle + \frac{1}{4}\left|\langle[X_1,X_2]\rangle\right|^2. \tag{5.26}$$

Since $\{X_1,X_2\} = \{X_2,X_1\}$, the first two terms cancel, and we are left with the inequality:

$$\det\left(C\left(X_1,X_2\right)\right) \geq \frac{1}{4}\left|\langle[X_1,X_2]\rangle\right|^2. \tag{5.27}$$

Thus, we see that the commutation relations between operators set the lower bounds on the determinants of covariance matrices. We will therefore calculate the commutators among the four new homodyne operators in order to set bounds on determinants within the larger

covariance matrix.

$$
\begin{aligned}
&C\left(\tilde{X}^{\mathrm{Re}}_{\mathrm{AM}}, \tilde{X}^{\mathrm{Re}}_{\mathrm{PM}}, \tilde{X}^{\mathrm{Im}}_{\mathrm{AM}}, \tilde{X}^{\mathrm{Im}}_{\mathrm{PM}}\right) \\
&= \frac{1}{2}\begin{pmatrix}
\left\langle\left\{\tilde{X}^{\mathrm{Re}}_{\mathrm{AM}}, \tilde{X}^{\mathrm{Re}}_{\mathrm{AM}}\right\}\right\rangle & \left\langle\left\{\tilde{X}^{\mathrm{Re}}_{\mathrm{AM}}, \tilde{X}^{\mathrm{Re}}_{\mathrm{PM}}\right\}\right\rangle & \left\langle\left\{\tilde{X}^{\mathrm{Re}}_{\mathrm{AM}}, \tilde{X}^{\mathrm{Im}}_{\mathrm{AM}}\right\}\right\rangle & \left\langle\left\{\tilde{X}^{\mathrm{Re}}_{\mathrm{AM}}, \tilde{X}^{\mathrm{Im}}_{\mathrm{PM}}\right\}\right\rangle \\
\left\langle\left\{\tilde{X}^{\mathrm{Re}}_{\mathrm{PM}}, \tilde{X}^{\mathrm{Re}}_{\mathrm{AM}}\right\}\right\rangle & \left\langle\left\{\tilde{X}^{\mathrm{Re}}_{\mathrm{PM}}, \tilde{X}^{\mathrm{Re}}_{\mathrm{PM}}\right\}\right\rangle & \left\langle\left\{\tilde{X}^{\mathrm{Re}}_{\mathrm{PM}}, \tilde{X}^{\mathrm{Im}}_{\mathrm{AM}}\right\}\right\rangle & \left\langle\left\{\tilde{X}^{\mathrm{Re}}_{\mathrm{PM}}, \tilde{X}^{\mathrm{Im}}_{\mathrm{PM}}\right\}\right\rangle \\
\left\langle\left\{\tilde{X}^{\mathrm{Im}}_{\mathrm{AM}}, \tilde{X}^{\mathrm{Re}}_{\mathrm{AM}}\right\}\right\rangle & \left\langle\left\{\tilde{X}^{\mathrm{Im}}_{\mathrm{AM}}, \tilde{X}^{\mathrm{Re}}_{\mathrm{PM}}\right\}\right\rangle & \left\langle\left\{\tilde{X}^{\mathrm{Im}}_{\mathrm{AM}}, \tilde{X}^{\mathrm{Im}}_{\mathrm{AM}}\right\}\right\rangle & \left\langle\left\{\tilde{X}^{\mathrm{Im}}_{\mathrm{AM}}, \tilde{X}^{\mathrm{Im}}_{\mathrm{PM}}\right\}\right\rangle \\
\left\langle\left\{\tilde{X}^{\mathrm{Im}}_{\mathrm{PM}}, \tilde{X}^{\mathrm{Re}}_{\mathrm{AM}}\right\}\right\rangle & \left\langle\left\{\tilde{X}^{\mathrm{Im}}_{\mathrm{PM}}, \tilde{X}^{\mathrm{Re}}_{\mathrm{PM}}\right\}\right\rangle & \left\langle\left\{\tilde{X}^{\mathrm{Im}}_{\mathrm{PM}}, \tilde{X}^{\mathrm{Im}}_{\mathrm{AM}}\right\}\right\rangle & \left\langle\left\{\tilde{X}^{\mathrm{Im}}_{\mathrm{PM}}, \tilde{X}^{\mathrm{Im}}_{\mathrm{PM}}\right\}\right\rangle
\end{pmatrix} \\
&= \begin{pmatrix} C_1 & C_2 \\ C_3 & C_4 \end{pmatrix}
\end{aligned}
\tag{5.28}
$$

The quadrants C_1 and C_4 are just 2×2 covariance matrices for the real and imaginary operators respectively. C_2 and C_3, which combine real and imaginary operators, cannot be defined thus, and are therefore not so easily related to the commutation relations used in the derivation of the uncertainty principle. Nonetheless, it may be instructive to check the limits of the diagonal quadrant determinants.

In the case of the real operators, $\tilde{X}^{\mathrm{Re}}_{\mathrm{AM}}$ and $\tilde{X}^{\mathrm{Re}}_{\mathrm{PM}}$,

$$
\begin{aligned}
&\left[\tilde{X}^{\mathrm{Re}}_{\mathrm{AM}}(\omega), \tilde{X}^{\mathrm{Re}}_{\mathrm{PM}}(\omega)\right] \\
&= \frac{1}{T}\int_0^T \int_0^T dt'dt \Big\{ \left[a^\dagger(t')\cos(\omega t') + a(t')\cos(\omega t')\right]\left[a^\dagger(t)\cos(\omega t) - a(t)\cos(\omega t)\right] \\
&- \left[a^\dagger(t)\cos(\omega t) - a(t)\cos(\omega t)\right]\left[a^\dagger(t')\cos(\omega t') + a(t')\cos(\omega t')\right] \Big\} \\
&= \frac{1}{T}\int_0^T \int_0^T dt'dt \cos(\omega t')\cos(\omega t) \big\{ \left[a^\dagger(t'), a^\dagger(t)\right] - [a(t'), a(t)] \\
&+ \left[a(t), a^\dagger(t')\right] + \left[a(t'), a^\dagger(t)\right] \big\} \\
&= \frac{2}{T}\int_0^T dt \cos^2(\omega t)
\end{aligned}
\tag{5.29}
$$

For the last line, we have assumed that $a(t)$ is uncorrelated with $a(t')$. Similarly, we find for the imaginary terms:

$$
\left[\tilde{X}^{\mathrm{Im}}_{\mathrm{AM}}(\omega), \tilde{X}^{\mathrm{Im}}_{\mathrm{PM}}(\omega)\right] = -\frac{2}{T}\int_0^T dt \sin^2(\omega t) \tag{5.30}
$$

If we go through these calculations for every combination of the four operators, we find only

four non-zero commutators result.

$$\begin{aligned}
\left[\tilde{X}^{\mathrm{Re}}_{\mathrm{AM}}, \tilde{X}^{\mathrm{Re}}_{\mathrm{PM}}\right] &= \frac{2}{T}\int_0^T dt \cos^2(\omega t) &&= 1 + \frac{\cos(\omega T)\sin(\omega T)}{\omega T} \\
\left[\tilde{X}^{\mathrm{Im}}_{\mathrm{AM}}, \tilde{X}^{\mathrm{Im}}_{\mathrm{PM}}\right] &= -\frac{2}{T}\int_0^T dt \sin^2(\omega t) &&= -1 + \frac{\cos(\omega T)\sin(\omega T)}{\omega T} \\
\left[\tilde{X}^{\mathrm{Re}}_{\mathrm{AM}}, \tilde{X}^{\mathrm{Im}}_{\mathrm{PM}}\right] &= -\frac{2}{T}\int_0^T dt \cos(\omega t)\sin(\omega t) &&= -\frac{\sin^2(\omega T)}{\omega T} \\
\left[\tilde{X}^{\mathrm{Im}}_{\mathrm{AM}}, \tilde{X}^{\mathrm{Re}}_{\mathrm{PM}}\right] &= \frac{2}{T}\int_0^t dt \cos(\omega t)\sin(\omega t) &&= \frac{\sin^2(\omega T)}{\omega T}.
\end{aligned} \tag{5.31}$$

As T gets large, the first and second commutators tend toward 1, while the third and fourth approach 0. These allow us to put limits on the determinants of the diagonal quadrants of the covariance matrix.

$$\begin{aligned}
\det C_1 &\geq \frac{1}{4}\left|\left\langle\left[\tilde{X}^{\mathrm{Re}}_{\mathrm{AM}}, \tilde{X}^{\mathrm{Re}}_{\mathrm{PM}}\right]\right\rangle\right|^2 = \frac{1}{4} \\
\det C_4 &\geq \frac{1}{4}\left|\left\langle\left[\tilde{X}^{\mathrm{Im}}_{\mathrm{AM}}, \tilde{X}^{\mathrm{Im}}_{\mathrm{PM}}\right]\right\rangle\right|^2 = \frac{1}{4}
\end{aligned} \tag{5.32}$$

This suggests that the pair of real operators and the pair of imaginary operators each constitute a sort of harmonic oscillator with its own uncertainty limits.

The off-diagonal quadrants are not so straight-forward, unfortunately. They do not have the form of self-contained covariance matrices, and thus, we cannot apply our inequality to set a limit on their determinants. However, suppose we were considering the covariance of the operators that we might have access to: $C\left(\tilde{X}^{\mathrm{Re}}_{\mathrm{AM}}, \tilde{X}^{\mathrm{Im}}_{\mathrm{PM}}\right)$. The determinant of this matrix would be equal to the product of its eigenvalues, so a lower bound on this would tell us something about uncertainties in this basis. We know then that

$$\det C\left(\tilde{X}^{\mathrm{Re}}_{\mathrm{AM}}, \tilde{X}^{\mathrm{Im}}_{\mathrm{PM}}\right) \geq \frac{1}{4}\left|\left\langle\left[\tilde{X}^{\mathrm{Re}}_{\mathrm{AM}}, \tilde{X}^{\mathrm{Im}}_{\mathrm{PM}}\right]\right\rangle\right|^2 = 0. \tag{5.33}$$

That is, there is no lower limit on the product of the eigenvalues of the matrix. The same is true for $C\left(\tilde{X}^{\mathrm{Im}}_{\mathrm{AM}}, \tilde{X}^{\mathrm{Re}}_{\mathrm{PM}}\right)$.

However, this is not entirely a satisfactory result. We still do not know the limits imposed on products of eigenvalues for the entire covariance matrix $C\left(\tilde{X}^{\mathrm{Re}}_{\mathrm{AM}}, \tilde{X}^{\mathrm{Re}}_{\mathrm{PM}}, \tilde{X}^{\mathrm{Im}}_{\mathrm{AM}}, \tilde{X}^{\mathrm{Im}}_{\mathrm{PM}}\right)$. We hypothesize that if complex squeezing occurs in some complex quadrature $\mathrm{Real}[\mu]\tilde{X}^{\mathrm{Re}}_{\mathrm{AM}} + \mathrm{Imag}[\mu]_i\tilde{X}^{\mathrm{Im}}_{\mathrm{AM}} + \mathrm{Real}[\nu]\tilde{X}^{\mathrm{Re}}_{\mathrm{PM}} + \mathrm{Imag}[\nu]\tilde{X}^{\mathrm{Im}}_{\mathrm{PM}}$, then anti-squeezing will appear in the conjugate complex quadrature, since complex squeezing is really just an extension of real quadrature squeezing. We might guess, using this comparison, that a limit to the product of all four eigenvalues would be $1/16$, the product of the limits for the two diagonal quadratures. This would be in keeping with the interpretation of our four operators as composing two individual harmonic oscillators that can be coupled by optomechanical interaction. If this is the case, then any quadrature with noise that drops below a vacuum value of $1/4$ could be said to be squeezed.

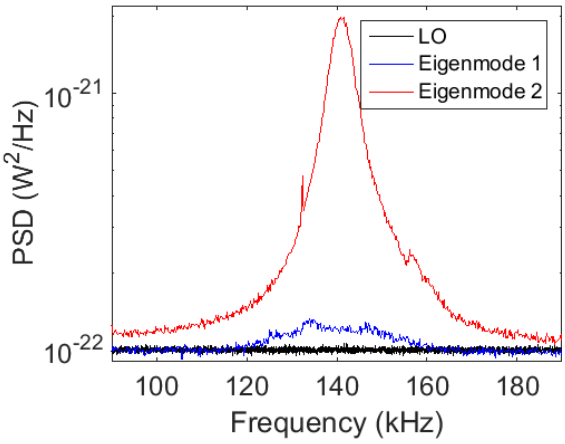

Figure 5.4: Eigenmodes of the covariance matrix for experimental data recorded in Brooks et al. [26] that showed real ponderomotive squeezing at frequencies away from ω_m. Neither eigenmode dips below the vacuum level at mechanical resonance, a symptom of too much PM laser noise at the input and an improper detuning for observing the ideal correlation angle between AM and PM output fluctuations.

5.3 Experimental observations

With a guess as to the vacuum value below which we can define an complex squeezed state, we now turn to the effort to observe one experimentally. In general, a homodyne detector cannot measure a quadrature that combines the operators in such a way so as to observe complex squeezing. This can be understood by considering again Eq. 4.2 for the homodyne spectrum. It can be rewritten in terms of components of the covariance matrix $\left[C\left(\tilde{X}^{\mathrm{Re}}_{\mathrm{AM}}, \tilde{X}^{\mathrm{Re}}_{\mathrm{PM}}, \tilde{X}^{\mathrm{Im}}_{\mathrm{AM}}, \tilde{X}^{\mathrm{Im}}_{\mathrm{PM}}\right)\right]_{ij}$:

$$\begin{aligned} S(\phi,\omega) = \cos^2(\phi)\left\{[C(\omega)]_{11} + [C(\omega)]_{33}\right\} + \sin^2(\phi)\left\{[C(\omega)]_{22} + [C(\omega)]_{44}\right\} \\ + \cos(\phi)\sin(\phi)\left\{[C(\omega)]_{12} + [C(\omega)]_{21} + [C(\omega)]_{34} + [C(\omega)]_{43}\right\}. \end{aligned} \tag{5.34}$$

The homodyne spectrum is only sensitive to components of the quadrants C_1 and C_4, and carries no information about C_2 or C_3. The diagonal quadrants only compare real components of AM with real components of PM, or likewise for imaginary, thus never capturing correlations that might exist when one is real and one is imaginary.

A heterodyne detector, on the other hand, that cycles through quadratures at a rate faster than any of the experimental time scales can give access to all four operators defined in the last section[4]. Thus, if we calculate the eigenmodes of the covariance matrices for

[4]As was the case in the force sensitivity measurement of Ch. 3, heterodyne detection introduces some additional unwanted shot-noise which may make limit squeezing and sensitivity. This is due to the fact that the receiver spends some portion of the measurement record sampling the "wrong" quadratures, mixing in noise while detecting no useful signal

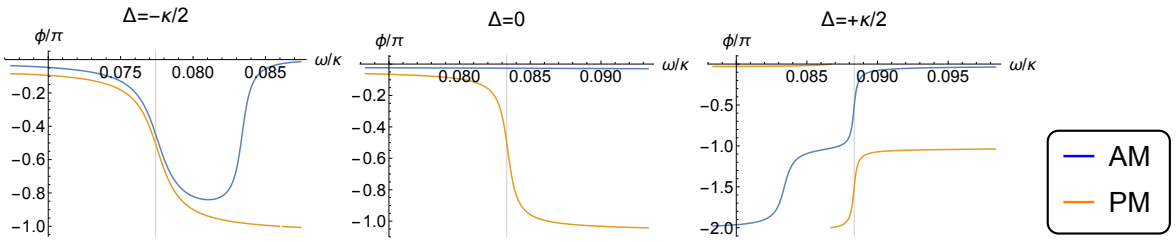

Figure 5.5: On cavity resonance (center), AM fluctuations injected into the optomechanical system drive AM output fluctuations directly and PM output fluctuations indirectly through the optomechanical interaction. The relative phases of the outgoing AM and PM with respect to the input AM are plotted. The same are plotted for light detuned to the red (left panel) and the blue (right panel) of cavity resonance, in which case the detuning of the cavity provides additional rotation of the quadratures. The grey vertical lines in each panel show the effective mechanical resonance of the oscillator, shifted by the Δ-dependent spring shift. With the light red-detuned as in the data in Fig. 5.4, we expect almost no phase difference between correlated AM and PM at mechanical resonance.

the heterodyne operators recorded for each frequency across a spectrum that includes the optomechanical response, we may expect to see eigenvalues that show squeezing. We were originally inclined to examine the data set for which we knew that experimental parameters had permitted the observation of real ponderomotive squeezing, that used in Ref. [26]. However, the eigenmodes measured during heterodyne detection, shown in Fig. 5.4, showed no such squeezing beyond the real squeezing already measured at frequencies away from ω_m.

A more careful investigation of the expected phase of the correlation suggests the obstacle. With the probe red-detuned from cavity resonance, as it was in those data and as shown in Fig. 5.5, the part of the optical PM fluctuations correlated with AM is actually in phase with the AM near the shifted mechanical resonance (identified by grey vertical lines), where the response is strongest. Though the $\pi/2$ phase difference is restored at the unshifted resonance in each case, not enough susceptibility remains at this frequency to allow for much backaction to contribute. Figure 5.5 instead suggests that a measurement made with a probe resonant with the cavity would overlay the maximum susceptibility with the imaginary correlations.

5.3.1 New search for complex squeezing

With this motivation, we turned our experiment to measure optomechanical correlations with a probe resonant with the cavity. We measure the optomechanical response of an oscillator probed with cooperativity approximately that for achieving the SQL, where the noise power of measurement backaction should equal that of shot-noise. We therefore expect that in the appropriate eigenmode, we should see some reduction of the noise power below the vacuum level due to the coherent subtraction of this backaction. The resulting eigenvalue spectra for this measurement are shown in Fig. 5.6. To understand this figure, we recall from

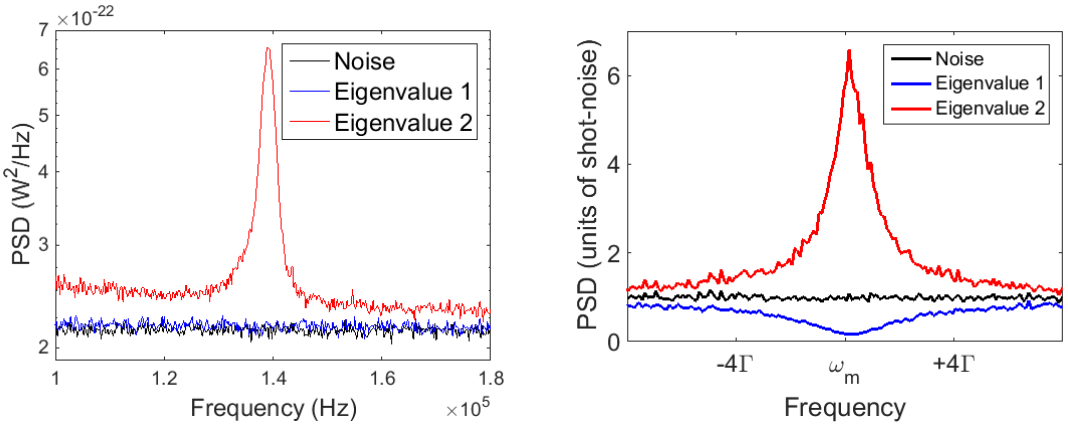

Figure 5.6: Experimental data (left) and simulation (right) for the covariance matrix eigenvalues for a mechanical oscillator measured on cavity resonance and with C_{om} near the value which attains the SQL of sensitivity. The experimental data show no visible dip below the vacuum level that would suggest complex squeezing. The simulation has similar parameters to the experiment, but assumes perfect detection efficiency and no thermal phonon occupation.

Ch. 4 that the probe light used is only shot-noise limited in the AM quadrature. The PM quadrature, in the mean time, contains enough noise to potentially swamp any squeezing. Since we envision the minimum-valued eigenmode being a complex combination of AM and PM, it will certainly contain some of this noise. We compare our measured spectra to simulations with shot-noise limited probe to envision how a complex squeezing observation would appear. The right panel of Fig. 5.6 shows an obvious dip of one eigenmode below the vacuum level.

Further investigation into the theoretical extent of complex squeezing yields the expected dependence on detection efficiency. Our simulation in Fig. 5.6 assumes perfect detection efficiency, and the decrease in squeezing visibility from this case to the more realistic case of $\varepsilon \approx 0.1$ that we regularly encounter experimentally is apparent in Fig. 5.7. With low detection efficiency, we must rely upon a large ensemble of measurements in order to average for long enough to be sensitive to complex squeezing at the level of only a few percent. As discussed in Ch. 4, however, larger ensembles of measurements make us more prone to experimental drift.

In addition to the limitations imposed by detection efficiency, the thermal occupation of the mechanical oscillator poses some risk for the observation of complex squeezing. Though experimentally our mechanical oscillator is near its ground state, we still measure a residual thermal occupation of approximately one phonon shared among the thousands of atoms that compose the oscillator. This is of particular concern since the noise from this phonon occurs exactly at the frequency of interest for complex squeezing. The predicted reduction in squeezing for additional phonon occupation is plotted in Fig. 5.8.

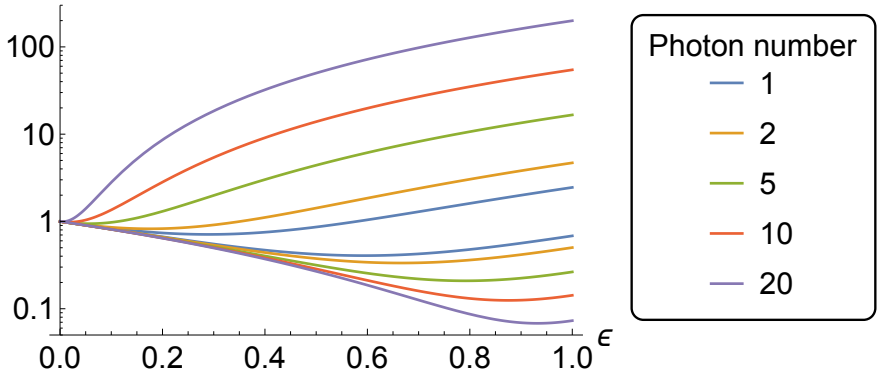

Figure 5.7: Predicted covariance eigenvalues (in units of shot-noise) for experimental parameters like those in Fig. 5.6 as a function of detection efficiency, assuming no thermal phonon occupation. Figure 5.6 presents experimental data with approximately 2 photons and 10% detection efficiency.

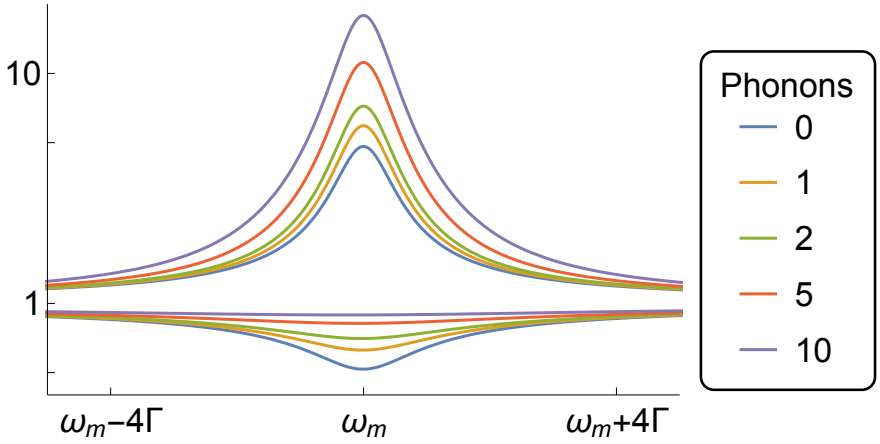

Figure 5.8: Predicted covariance eigenvalues (in units of shot-noise) for experimental parameters like those in Fig. 5.6 as a function of frequency, assuming perfect detection efficiency and 2 probe photons. Figure 5.6 presents experimental data with approximately 1 phonon.

5.3.2 Angles of complex squeezing

Despite the lack of experimental evidence for squeezing, we can examine the composition of the two eigenmodes of the data to see if the complex coefficients μ and ν match those theorized. Recalling that the orientation of the eigenmodes in the two-dimensional case could be described by a single quantity ϕ, we will find that in the four-dimensional case, two angles ϕ and θ, plus a normalization condition, suffice.

As described before, the eigenmodes of the covariance matrix can be given by $\mu\hat{X}_{\mathrm{AM}} + \nu\hat{X}_{\mathrm{PM}}$, where μ and ν can be complex numbers. There is an additional normalization restriction on μ and ν. Principal component analysis is achieved by first measuring $\tilde{X}_{\mathrm{AM}}(\omega_i)$ and $\tilde{X}_{\mathrm{PM}}(\omega_i)$, the complex Fourier responses at frequency ω_i. Equivalent to finding the eigenvalues of the 4×4 covariance matrix is calculating the value

$$\Sigma_i \left| \mu\tilde{X}_{\mathrm{AM}}(\omega_i) + \nu\tilde{X}_{\mathrm{PM}}(\omega_i) \right|^2 = P, \tag{5.35}$$

and then solving for $\frac{\partial P}{\partial \mu_i, \nu_i} = 0$ with the normalization constraint that $|\mu|^2 + |\nu|^2 = 1$. In practice, both of these techniques result in 4 eigenvalue/eigenvector pairs. These eigenvalues tell us about the strength of the correlations, while the eigenvectors tell us about the quadrature angles of the correlations.

We can plot the resulting eigenvector angles on a sphere and follow their trajectory as a function of frequency. This is similar to following the state of a two-level-system on a Bloch Sphere. In this case, we represent the state of the squeezed eigenmode as

$$\begin{aligned} |\psi\rangle &= \mu\,|0\rangle + \nu\,|1\rangle \\ &= r_\mu e^{i\phi_\mu}\,|0\rangle + r_\nu e^{i\phi_\nu}\,|1\rangle\,, \end{aligned} \tag{5.36}$$

where μ and ν can be complex coefficients. However, because the overall phase of $|\psi\rangle$ does not matter as it is not measurable, we can rotate the state to make μ real:

$$|\psi'\rangle = e^{-i\phi_\mu}\,|\psi\rangle = r_\mu\,|0\rangle + r_\nu e^{i(\phi_\nu - \phi_\mu)}\,|1\rangle\,. \tag{5.37}$$

In spherical coordinates, with $|0\rangle$ being the north pole of the sphere and $|1\rangle$ being the equator, we can rewrite this as

$$|\psi'\rangle = \cos\frac{\theta}{2}\,|0\rangle + e^{i\phi}\sin\frac{\theta}{2}\,|1\rangle\,, \tag{5.38}$$

where θ is now the polar angle and ϕ the azimuthal angle around the equator. One can easily find that $\theta = 2\cos^{-1} r_\mu$ and $\phi = -i\ln(\frac{r_\nu}{\sqrt{1-r_\mu^2}}) + \phi_\nu - \phi_\mu$. But we also know that $|\mu|^2 + |\nu|^2 = r_\mu^2 + r_\nu^2 = 1$, so we recover $\phi = \phi_\nu - \phi_\mu$.

How can we interpret these coordinates? The polar angle θ now represents the relative contribution of AM compared to PM, with $\theta = 0$ giving only AM contribution to correlations (and thus no correlations between quadratures at all) and $\theta = \pi$ giving only PM contribution.

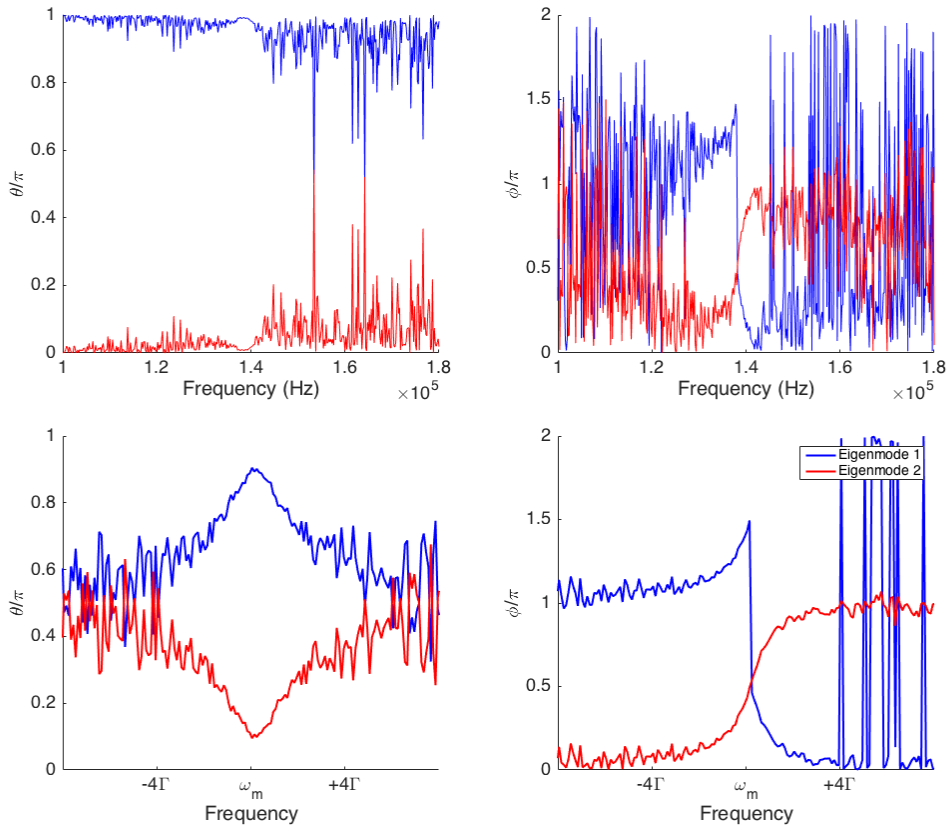

Figure 5.9: Eigenvector angles as a function of frequency for data (top) and simulations (bottom) presented in Fig. 5.6. Left panels show polar angle θ, which gives the mixing angle of $|\tilde{X}_{\mathrm{AM}}|$ and $|\tilde{X}_{\mathrm{PM}}|$. Right panels show azimuthal angle ϕ, which gives the relative phase between the arguments of $\tilde{X}_{\mathrm{AM}}$ and $\tilde{X}_{\mathrm{PM}}$. Away from mechanical resonance, both angles become ill defined as the backaction correlation that directs the angles of the eigenmodes disappears.

The azimuthal angle ϕ is the relative phase between AM and PM of the correlations. For example, if $(\theta, \phi) = (\pi/2, 0)$, then there are maximal correlations between AM and PM occurring at the same Fourier angle for AM as for PM (e.g. real with real or imaginary with imaginary). If $(\theta, \phi) = (\pi/2, \pi/2)$, then the Fourier angles for maximal correlations are out of phase (e.g. real with imaginary or imaginary with real).

In practice, the excursions of θ from the pole and the equator are small, so it is easier to plot the individual angles as a function of frequency separately, rather than trace both on the surface of a sphere. Figure 5.9 shows the angles of the eigenvectors for the data with eigenvalues shown in Fig. 5.6. There is definitely qualitative agreement between experiment and simulation. That the experimental angles θ are very nearly 0 and π for all frequencies suggests that the principal component analysis is picking out and isolating the laser phase noise to the stronger eigenmode. Still, it is the angle ϕ that hints at the presence of out-of-phase correlations between $\hat{X}_{\mathrm{AM}}$ and $\hat{X}_{\mathrm{PM}}$ in the data. As the frequency traverses mechanical

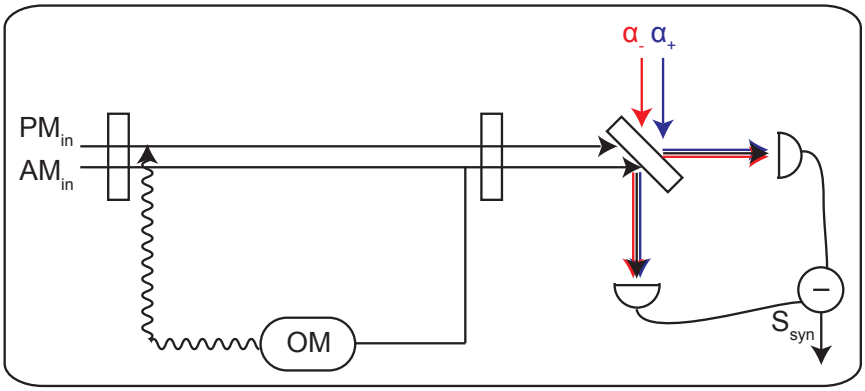

Figure 5.10: Schematic for "synodyne" detection method. The optomechanical element OM correlates AM fluctuations and PM fluctuations. A two-colored LO, with components α_- at frequency $-\omega_m$ and α_+ at frequency $+\omega_m$, mixes with the signal in such a way as to subtract the correlated noise.

resonance, the correlations go from in-phase to out-of-phase to in-phase again, precisely the expected behavior that could contribute to complex squeezing in the absence of excess laser noise.

5.3.3 Requirements for detection

I have already discussed the experimental limitations that would need to be addressed in order to detect complex squeezing. While detection efficiency and phonon occupation restrict the amount of squeezing detectable, they do not preclude its observation. More pressing is the instance of phase noise on our probe laser which pollutes the detection modes of interest. As discussed in Ch. 4, by moving the oscillator of interest to higher frequencies, we could operate in a regime of shot-noise limited laser noise in all quadratures.

Another detection issue is that a heterodyne receiver, despite its ability to cycle through quadratures and perhaps be sensitive to some complex squeezing, is not maximally sensitive to the effect. This is because it necessarily introduces additional shot-noise as it cycles through insensitive quadratures. In Buchmann et al. [39], we propose an alternate detection method that we term "synodyne" for its use of multiple tones to produce the LO. In particular, we consider the case of an LO composed of two tones detuned by $\pm\omega_m$ from the carrier frequency of the probe light (α_+ and α_- as shown in Fig. 5.10). This solution to the measurement of complex squeezing is intuitive. The two-tone LO mixes the optomechanically-produced sidebands in such a way that at the carrier frequency of the probe they interfere with strength and angle determined by the power and relative phase of the LO tones. Tuning the power and phase of these tones allows for the selection of ϕ and θ that correspond to the squeezed eigenmode. Unlike in heterodyne detection, this synodyne scheme always measures the ideal mode, introducing no additional shot-noise and perfectly

subtracting the correlated backaction noise. We show in Ref. [39] that there is in principle no limit to the observable squeezing using this method. Furthermore, we find that we can tune the synodyne parameters so as to measure a single-quadrature force with imprecision that decays without bound with increasing cooperativity.

With synodyne detection for complex squeezing, we propose a solution to the problem of measurement backaction explored throughout this dissertation. Synodyne harnesses the complex squeezing implied yet obscured in the ponderomotive squeezing measurements of Ch. 4 to subtract the correlated backaction from force measurements like those in Ch. 3. We ultimately find that through a careful accounting of noise and correlations, one can the expand the confines of quantum measurement limits.

Bibliography

[1] Bretislav Friedrich and Dudley Herschbach. Stern and Gerlach: How a bad cigar helped reorient atomic physics. *Physics Today*, 56(12):53–59, 2003.

[2] I. I. Rabi, J. R. Zacharias, S. Millman, and P. Kusch. A new method of measuring nuclear magnetic moment. *Phys. Rev.*, 53:318–318, Feb 1938.

[3] Paul Adrien Maurice Dirac. *The Principles of Quantum Mechanics*. International series of monographs on physics. Clarendon Press, 1981.

[4] John Von Neumann. *Mathematical foundations of quantum mechanics*. Princeton University Press, 1955.

[5] Howard M Wiseman and Gerard J Milburn. *Quantum measurement and control*. Cambridge University Press, 2009.

[6] Vladimir B Braginsky, Farid Ya Khalili, and Kip S Thorne. *Quantum measurement*. Cambridge University Press, 1995.

[7] John F Clauser. Experimental distinction between the quantum and classical field-theoretic predictions for the photoelectric effect. *Physical Review D*, 9(4):853, 1974.

[8] HJ Kimble, M Dagenais, and L Mandel. Photon antibunching in resonance fluorescence. *Physical Review Letters*, 39(11):691, 1977.

[9] DJ Wineland, RE Drullinger, and FL Walls. Radiation-pressure cooling of bound resonant absorbers. *Physical Review Letters*, 40(25):1639, 1978.

[10] F Diedrich, JC Bergquist, Wayne M Itano, and DJ Wineland. Laser cooling to the zero-point energy of motion. *Physical Review Letters*, 62(4):403, 1989.

[11] Serge Haroche and Jean Michel Raimond. *Exploring the quantum*. Oxford Univ. Press, 2006.

[12] Serge Haroche. Nobel lecture: Controlling photons in a box and exploring the quantum to classical boundary. *Reviews of Modern Physics*, 85(3):1083, 2013.

[13] Edwin T Jaynes and Frederick W Cummings. Comparison of quantum and semiclassical radiation theories with application to the beam maser. *Proceedings of the IEEE*, 51(1): 89–109, 1963.

[14] Frederick W Cummings. Reminiscing about thesis work with ET Jaynes at Stanford in the 1950s. *Journal of Physics B: Atomic, Molecular and Optical Physics*, 46(22): 220202, 2013.

[15] GR Guthöhrlein, M Keller, K Hayasaka, W Lange, and H Walther. A single ion as a nanoscopic probe of an optical field. *Nature*, 414(6859):49–51, 2001.

[16] AB Mundt, A Kreuter, C Becher, D Leibfried, J Eschner, F Schmidt-Kaler, and R Blatt. Coupling a single atomic quantum bit to a high finesse optical cavity. *Physical Review Letters*, 89(10):103001, 2002.

[17] Andreas Wallraff, David I Schuster, Alexandre Blais, L Frunzio, R-S Huang, J Majer, S Kumar, Steven M Girvin, and Robert J Schoelkopf. Strong coupling of a single photon to a superconducting qubit using circuit quantum electrodynamics. *Nature*, 431(7005): 162–167, 2004.

[18] Alex Abramovici, William E Althouse, Ronald WP Drever, Yekta Gürsel, Seiji Kawamura, Frederick J Raab, David Shoemaker, Lisa Sievers, Robert E Spero, Kip S Thorne, et al. LIGO: The laser interferometer gravitational-wave observatory. *Science*, 256 (5055):325–333, 1992.

[19] Tobias J Kippenberg and Kerry J Vahala. Cavity optomechanics: back-action at the mesoscale. *Science*, 321(5893):1172–1176, 2008.

[20] Markus Aspelmeyer, Tobias J Kippenberg, and Florian Marquardt. Cavity optomechanics. *Reviews of Modern Physics*, 86(4):1391, 2014.

[21] JD Thompson, BM Zwickl, AM Jayich, Florian Marquardt, SM Girvin, and JGE Harris. Strong dispersive coupling of a high-finesse cavity to a micromechanical membrane. *Nature*, 452(7183):72–75, 2008.

[22] William D Phillips. Nobel lecture: Laser cooling and trapping of neutral atoms. *Reviews of Modern Physics*, 70(3):721, 1998.

[23] David J Wineland. Nobel lecture: Superposition, entanglement, and raising Schrödinger's cat. *Reviews of Modern Physics*, 85(3):1103, 2013.

[24] Pierre-François Cohadon, Antoine Heidmann, and Michel Pinard. Cooling of a mirror by radiation pressure. *Physical Review Letters*, 83(16):3174, 1999.

[25] Jasper Chan, TP Mayer Alegre, Amir H Safavi-Naeini, Jeff T Hill, Alex Krause, Simon Gröblacher, Markus Aspelmeyer, and Oskar Painter. Laser cooling of a nanomechanical oscillator into its quantum ground state. *Nature*, 478(7367):89–92, 2011.

[26] Daniel WC Brooks, Thierry Botter, Sydney Schreppler, Thomas P Purdy, Nathan Brahms, and Dan M Stamper-Kurn. Non-classical light generated by quantum-noise-driven cavity optomechanics. *Nature*, 488(7412):476–480, 2012.

[27] Amir H Safavi-Naeini, Simon Gröblacher, Jeff T Hill, Jasper Chan, Markus Aspelmeyer, and Oskar Painter. Squeezed light from a silicon micromechanical resonator. *Nature*, 500(7461):185–189, 2013.

[28] TP Purdy, P-L Yu, RW Peterson, NS Kampel, and CA Regal. Strong optomechanical squeezing of light. *Physical Review X*, 3(3):031012, 2013.

[29] Emma Edwina Wollman, CU Lei, AJ Weinstein, J Suh, A Kronwald, F Marquardt, AA Clerk, and KC Schwab. Quantum squeezing of motion in a mechanical resonator. *Science*, 349(6251):952–955, 2015.

[30] TA Palomaki, JD Teufel, RW Simmonds, and KW Lehnert. Entangling mechanical motion with microwave fields. *Science*, 342(6159):710–713, 2013.

[31] Igor Pikovski, Michael R Vanner, Markus Aspelmeyer, MS Kim, and Časlav Brukner. Probing planck-scale physics with quantum optics. *Nature Physics*, 8(5):393–397, 2012.

[32] Oriol Romero-Isart, Anika C Pflanzer, Florian Blaser, Rainer Kaltenbaek, Nikolai Kiesel, Markus Aspelmeyer, and J Ignacio Cirac. Large quantum superpositions and interference of massive nanometer-sized objects. *Physical Review Letters*, 107(2):020405, 2011.

[33] Aaron D O'Connell, Max Hofheinz, Markus Ansmann, Radoslaw C Bialczak, Mike Lenander, Erik Lucero, Matthew Neeley, Daniel Sank, H Wang, M Weides, et al. Quantum ground state and single-phonon control of a mechanical resonator. *Nature*, 464 (7289):697–703, 2010.

[34] Tom P Purdy, DWC Brooks, T Botter, N Brahms, Z-Y Ma, and DM Stamper-Kurn. Tunable cavity optomechanics with ultracold atoms. *Physical Review Letters*, 105(13): 133602, 2010.

[35] Nathan Brahms, Thierry Botter, Sydney Schreppler, Daniel WC Brooks, and Dan M Stamper-Kurn. Optical detection of the quantization of collective atomic motion. *Physical Review Letters*, 108(13):133601, 2012.

[36] Thierry Botter, Daniel WC Brooks, Sydney Schreppler, Nathan Brahms, and Dan M Stamper-Kurn. Optical readout of the quantum collective motion of an array of atomic ensembles. *Physical Review Letters*, 110(15):153001, 2013.

[37] Sydney Schreppler, Nicolas Spethmann, Nathan Brahms, Thierry Botter, Maryrose Barrios, and Dan M Stamper-Kurn. Optically measuring force near the standard quantum limit. *Science*, 344(6191):1486–1489, 2014.

[38] Nicolas Spethmann, Jonathan Kohler, Sydney Schreppler, Lukas Buchmann, and Dan M Stamper-Kurn. Cavity-mediated coupling of mechanical oscillators limited by quantum back-action. *Nature Physics*, 12(1):27–31, 2016.

[39] LF Buchmann, S Schreppler, J Kohler, N Spethmann, and DM Stamper-Kurn. Complex squeezing and force measurement beyond the standard quantum limit. *arXiv:1602.02141*, 2016.

[40] N Brahms and DM Stamper-Kurn. Spin optodynamics analog of cavity optomechanics. *Physical Review A*, 82(4):041804, 2010.

[41] Carlton M Caves, Kip S Thorne, Ronald WP Drever, Vernon D Sandberg, and Mark Zimmermann. On the measurement of a weak classical force coupled to a quantum-mechanical oscillator. I. Issues of principle. *Reviews of Modern Physics*, 52(2):341, 1980.

[42] AA Clerk, MH Devoret, SM Girvin, Florian Marquardt, and RJ Schoelkopf. Introduction to quantum noise, measurement, and amplification. *Reviews of Modern Physics*, 82(2):1155, 2010.

[43] JB Hertzberg, T Rocheleau, T Ndukum, M Savva, AA Clerk, and KC Schwab. Back-action-evading measurements of nanomechanical motion. *Nature Physics*, 6(3):213–217, 2010.

[44] Thomas Patrick Purdy. *Cavity QED with ultracold atoms on an atom chip*. PhD thesis, University of California, Berkeley, 2009.

[45] Michael Tavis and Frederick W Cummings. Exact solution for an N–molecule–radiation–field Hamiltonian. *Physical Review*, 170(2):379, 1968.

[46] Kater Whitney Murch. *Cavity quantum optomechanics with ultracold atoms*. PhD thesis, University of California, Berkeley, 2008.

[47] Carl E Wieman and Leo Hollberg. Using diode lasers for atomic physics. *Review of Scientific Instruments*, 62(1):1–20, 1991.

[48] Thierry Claude Marc Botter. *Cavity Optomechanics in the Quantum Regime*. PhD thesis, University of California, Berkeley, 2013.

[49] David Hunger, Tilo Steinmetz, Yves Colombe, Christian Deutsch, Theodor W Hänsch, and Jakob Reichel. A fiber Fabry–Perot cavity with high finesse. *New Journal of Physics*, 12(6):065038, 2010.

[50] F Marsili, VB Verma, JA Stern, S Harrington, AE Lita, T Gerrits, I Vayshenker, B Baek, MD Shaw, RP Mirin, et al. Detecting single infrared photons with 93% system efficiency. *Nature Photonics*, 7(3):210–214, 2013.

[51] K-K Ni, R Norte, DJ Wilson, JD Hood, DE Chang, O Painter, and HJ Kimble. Enhancement of mechanical Q factors by optical trapping. *Physical Review Letters*, 108 (21):214302, 2012.

[52] G Binnig, C Quate, and C Gerber. Atomic force microscope. *Physical Review Letters*, 56(9):930, 1986.

[53] Alexander G Krause, Martin Winger, Tim D Blasius, Qiang Lin, and Oskar Painter. A high-resolution microchip optomechanical accelerometer. *Nature Photonics*, 6(11): 768–772, 2012.

[54] Emanuel Gavartin, Pierre Verlot, and Tobias J Kippenberg. A hybrid on-chip optomechanical transducer for ultrasensitive force measurements. *Nature Nanotechnology*, 7 (8):509–514, 2012.

[55] Susannah M Dickerson, Jason M Hogan, Alex Sugarbaker, David MS Johnson, and Mark A Kasevich. Multiaxis inertial sensing with long-time point source atom interferometry. *Physical Review Letters*, 111(8):083001, 2013.

[56] Thierry Botter, Daniel WC Brooks, Nathan Brahms, Sydney Schreppler, and Dan M Stamper-Kurn. Linear amplifier model for optomechanical systems. *Physical Review A*, 85(1):013812, 2012.

[57] Carlton M Caves. Quantum-mechanical noise in an interferometer. *Physical Review D*, 23(8):1693, 1981.

[58] HJ Kimble, Yuri Levin, Andrey B Matsko, Kip S Thorne, and Sergey P Vyatchanin. Conversion of conventional gravitational-wave interferometers into quantum nondemolition interferometers by modifying their input and/or output optics. *Physical Review D*, 65(2):022002, 2001.

[59] RE Slusher, LW Hollberg, Bernard Yurke, JC Mertz, and JF Valley. Observation of squeezed states generated by four-wave mixing in an optical cavity. *Physical Review Letters*, 55(22):2409, 1985.

[60] VB Braginsky and AB Manukin. Ponderomotive effects of electromagnetic radiation. *Sov. Phys. JETP*, 25:653, 1967.

[61] Carlton M Caves. Quantum-mechanical radiation-pressure fluctuations in an interferometer. *Physical Review Letters*, 45(2):75, 1980.

[62] William G Unruh. *Quantum optics, experimental gravity, and measurement theory*, volume 94. Plenum Press, 1982.

[63] Claude Fabre, Michel Pinard, Sophie Bourzeix, Antoine Heidmann, Elisabeth Giacobino, and Serge Reynaud. Quantum-noise reduction using a cavity with a movable mirror. *Physical Review A*, 49(2):1337, 1994.

[64] Stefano Mancini and Paolo Tombesi. Quantum noise reduction by radiation pressure. *Physical Review A*, 49(5):4055, 1994.

[65] Leonard Mandel and Emil Wolf. *Optical coherence and quantum optics*. Cambridge University Press, 1995.

[66] V Peano, HGL Schwefel, Ch Marquardt, and F Marquardt. Intracavity squeezing can enhance quantum-limited optomechanical position detection through deamplification. *Physical Review Letters*, 115(24):243603, 2015.

[67] DF Walls and GJ Milburn. *Quantum Optics*. Springer, 1995.

[68] R Simon, N Mukunda, and Biswadeb Dutta. Quantum-noise matrix for multimode systems: U(n) invariance, squeezing, and normal forms. *Physical Review A*, 49(3):1567, 1994.

[69] Ramamurti Shankar. *Principles of quantum mechanics*. Springer Science & Business Media, 2012.

Appendix A

Digital heterodyne demodulation

Because we do not stabilize the LO path length with respect to the signal in our heterodyne measurements, we observe the heterodyne phase to drift at rates that are slow compared to our signals of interest. We nonetheless would like to remove this phase drift so that we can average signals over longer time records. Here I will describe the process of our digital heterodyne demodulation, giving examples of the heterodyne signal (Fig. A.1) after various filtering and downsampling steps have occurred. I additionally include some code that is paraphrased from an implementation of our algorithm realized in Matlab and originally developed by Nathan Brahms.

First, we record a raw heterodyne beat note on our digital oscilloscope (GaGe digital oscilloscope). This signal is usually between 10 and 40 ms in length and is recorded at a sampling rate of 80 MHz. It contains a large frequency component at 10 MHz (our heterodyne beat frequency), as well as information about all additional probing and locking tones, the potential signals of interest, and technical and quantum noise. We receive the signal with units of Volts, but can convert it to Watts given our knowledge of detector gains, bandwidths, and quantum efficiencies. In order to remove the slow phase drift attributable to thermal fluctuations, we first digitally demodulate the raw signal into a quadrature that is in phase with $\cos(\omega_{\mathrm{Het}}t)$ at $t = 0$ and one that is out of phase, with ω_{Het} the 10 MHz heterodyne beat frequency. In doing so, we use Matlab's *decimate* function, which downsamples a signal at a chosen rate and applies a low-pass filter. Importantly, this filter is applied twice, processing the data forward and backward through the *filtfilt* function. This ideally achieves zero phase distortion, which is important for maintaining the integrity of the phase information at our frequencies of interest.

Our next step is to isolate the slow phase drift of the signal by applying another instance of *decimate* to the two quadratures. We then find the relative phase between the two quadratures as a function of time, using this phase to create rotation masks that we can then apply to the original quadratures so that they more accurately represent higher frequency fluctuations that are either in-phase or out-of-phase with the LO at t=0.

These methods depend on a low-pass-filter that can separate any signals of interest from slower phase drifts without introducing too much phase ripple in the stopband (since we do

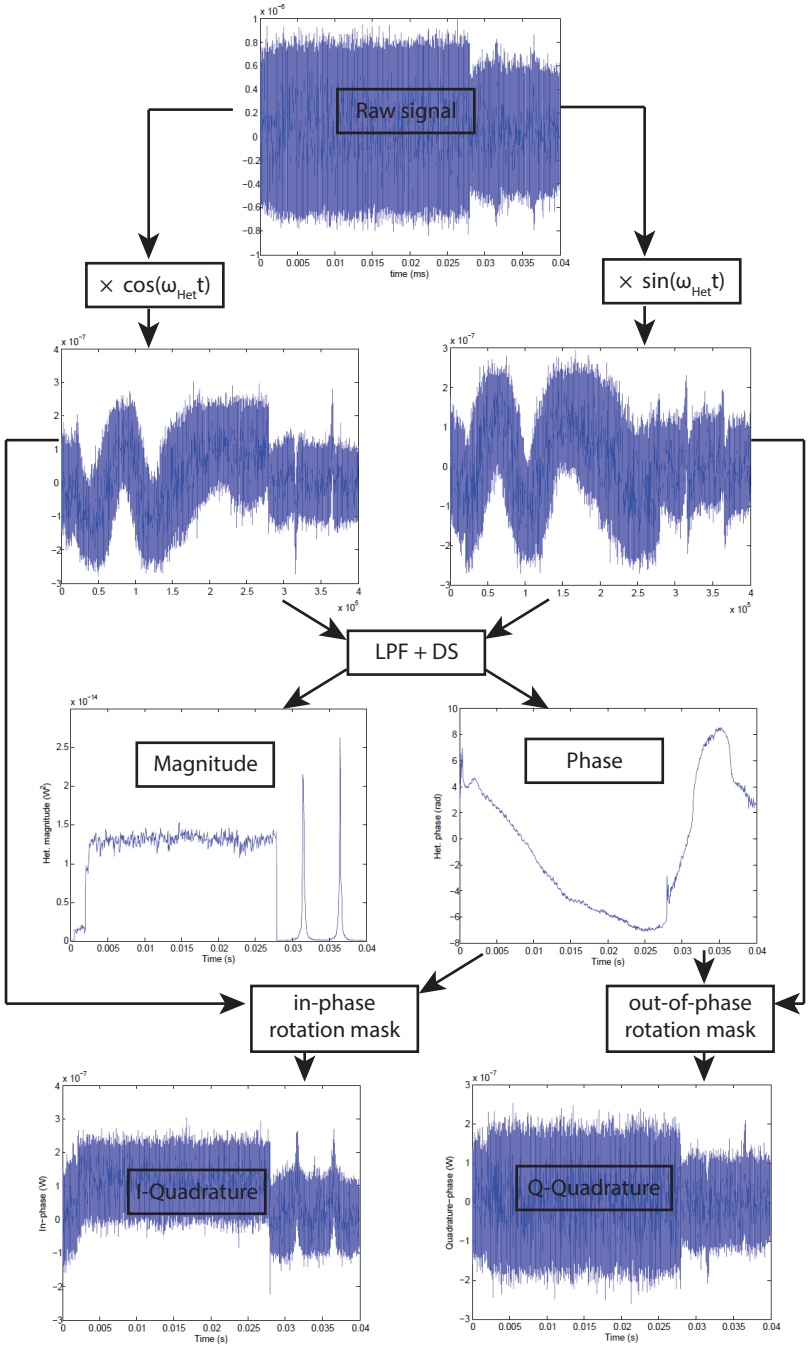

Figure A.1: The process of digital heterodyne demodulation. Raw time-series data are recorded on the digital oscilloscope. Steps are, from top to bottom: demodulate at ω_{Het}, low-pass-filter (LPF) and down-sample (DS) to find slow phase drift between quadratures, create phase masks to apply to demodulated time records to recover true quadrature information.

not want our eventual mask to alter the phases at higher frequencies, where our measurement information resides). There is some opportunity to improve upon the default filter chosen by Matlab, an 8th order Type 1 Chebyshev filter. A Butterworth filter, for example, provides a maximally flat passband at the expense of a less steep roll-off. We have found in practice that the choice between these two filters does not make a difference to the signal strengths we measure upon demodulation.

Digital heterodyne demodulation and parameter extraction

```
% Load GageScope voltage data as "raw"

    nGageBits = 16;% Number of bits in Gagescope data
    vGage = 4; % Gagescope voltage range (Peak-to-peak)

    raw = raw/2^(nGageBits)*vGage;

% Rescale raw voltage data to units of power

    impedance = 50; % Measurement impedance (ohms)
    gainDb = 30.1; % Gain of amp between detector and acquisition (dB)
    transimpedance=28.8e3;% Detector transimpedance gain (V/W)

    impAtten = 1-50/(50+impedance); % Attenuation due to impedance
    gain = 10^(gainDb/20);
    raw = raw/transimpedance/impAtten/gain; % Rescaled to units of W

% Fourier transform un-demodulated signal

    rawFFT = fftshift(fft(raw));% fftshift used to center dc

% Analyze heterodyne lock for values of nbar and delta_pc

    fCar = 10e6; %- Carrier frequency
    fMod = 2.87e6; %- Modulation frequency
    kappa = 1.82e6; %- Natural cavity linewidth (cyclic)
    rbGain = 1.14; %- Relative detection gain of red vs. blue sideband
    snRange = [2e5 4e5]; %- 2-element array indicating range over which to evaluate shot
noise
    edet = 0.10; %- Heterodyne detection efficiency
    kappaN = 2.15e6; %- Broadened cavity linewidth (cyclic)
    close = true; %- true if the lock point is within the sidebands, false otherwise

    Sb = rbGain*rawFFT.interp(fCar+fMod,'nearest'); %Power in blue sideband
```

```
    Sr = rawFFT.interp(fCar-fMod,'nearest'); %Power in red sideband
    rSB = (Sb-Sr)/(Sb+Sr);

% Calculate delta_pc

    if close
        dpc = (-fMod + sqrt(fMod^2 - rSB^2*(fMod^2 + kappa^2)))/rSB;
    else
        dpc = (-fMod - sqrt(fMod^2 - rSB^2*(fMod^2 + kappa^2)))/rSB;
    end

% Calculate nbar

    Sc = rawFFT.interp(fCar,'nearest'); % Power in carrier
    Ssn = mean(rawFFT.interp(fCar+min(snRange):rawFFT.dx:fCar+max(snRange),'nearest'))/2;
% Average noise power above carrier
    Ssn = Ssn + mean(S.interp(fCar-max(snRange):S.dx:fCar-min(snRange),'nearest'))/2;
% Average noise power below carrier
    nbar = (Sc/Ssn - 1)*rawFFT.dx/8/pi/kappaN/edet; % Carrier power in units of noise,
then scaled to units of photons

% Perform heterodyne demodulation
    filterBw = 10e3; % BW for quadrature identification, needs to be
    %small compared to signal frequencies of interest but large compared to slow thermal
drifts
    carrierFreq = 10e6; % Heterodyne beat carrier frequency
    doRotation = true; % If true, performs rotation of quadratures

%This is a three-step process. First, the heterodyne signal is demodulated
%at the carrier frequency, yielding the in-phase (I) and quadrature-phase (Q)
%signal components.

    dt1 = rawFFT.dx;
    0 = rawFFT.x0;

    carrierOmega = 2*pi*carrierFreq;
    r1 = round(1/dt1/carrierFreq);
    nRaw = floor(length(rawFFT)/r1);
    quadDt = r*dt1;

% Make the prototypical cos and sin arrays
```

```
t = linspace(t0,t0+(r1-1)*dt1,r1)';
iMask = cos(carrierOmega*t);
qMask = sin(carrierOmega*t);

iMask = repmat(iMask,nRaw,1);
qMask = repmat(qMask,nRaw,1);
iMask = rawFFT(:).*iMask;
qMask = rawFFT(:).*qMask;

% Here we use MatlabâĂŹs decimate(x,r) function, which downsamples and %downsamples x at factor of r and applies a lowpass Chebyshev Type 1 %IIR order 8 filter

iRaw = decimate(iMask,r1); % Filter and downsample
qRaw = decimate(qMask,r1); % Requires Signal Processing Toolbox

%Next, we determine the low-frequency instantaneous carrier amplitude and phase.

r2 = round(1/quadDt/filterBw/2); % Number of points over which to average
avgDt = r2*quadDt;
iAvg = decimate(iRaw,r2); % Again filter and downsample
qAvg = decimate(qRaw,r2);
mag = iAvg.^2+qAvg.^2;
phase = unwrap(atan2(qAvg,iAvg));

%Finally, the quadratures are rotated such that I reflects the true amplitude %modulation and Q reflects the true phase modulation.

ti = 0:quadDt:(length(iRaw)-1)*quadDt; % Time lookup array
phasei = winterp1(0,avgDt,phase,ti,'linear'); % Expand masks to size of %original quadratures iRaw and qRaw      iRot = iRaw.*cos(phasei) + qRaw.*sin(phasei); % Perform rotations
qRot = -iRaw.*sin(phasei) + qRaw.*cos(phasei);
```